Modelling of molecules on silicon surfaces and thin-film photovoltaic absorbers

Thesis submitted in accordance with the requirements of the University of Liverpool for the degree of Doctor of Philosophy

Piotr T. Czekała

September 30, 2013

Modeling of molecules on silicon surfaces and thin-film photovoltaic absorbers

PIOTR T. CZEKAŁA

Preface

This thesis covers the work performed by me during my time as a PhD student in the University of Liverpool in the research group of Prof. Werner Hofer. My work as a PhD student involved the theoretical modelling. I have not participated in the any experimental studies. When discussing work other then my own, I clearly state it and provide the source of presented information.

Piotr T. Czekała Liverpool September 30, 2013

Abstract

In this thesis a range of phenomena related to molecular adsorption on silicon surfaces is investigated. The majority of the studies are performed in response to experimental results, where, using newly developed methods within the framework of density functional theory, we aim to elucidate some of the underlying physics as well as test the performance of the chosen methodology. The studies cover a range of subjects such as molecularly mediated pinning of surface geometry, single molecular adsorptions, molecule migration via exited states and finally an analysis of coverage dependent adsorption phenomena, where interactions between molecules are mediated by the surface or enacted via dipole interactions. The main molecules of our simulations were water, ethylene, acetylene, and benzene, as well as halogenated hydrocarbons. We studied processes at two different surfaces, the Si(111)–7×7 surface, and the Si(100)–c(4×2) surface.

Finally we simulated and characterized one type of grain boundary observed experimentally for a set of photovoltaic absorbers ($CuInSe_2$) and kesterite and stannite($Cu_2ZnSnSe_4$ or Cu_2ZnSnS_4) in order to resolve the open question of how these grain boundaries influence efficiencies of the photovoltaic device.

Contents

Chapter 1

Introduction

1.1 Historical overview

One of the great moments in the development of science was certainly the invention of the computer, which not only revolutionized the way we work, but also the way science is conducted. In the last decade parallelization of computer processing has been the next grand step allowing access to computational power of previously inconceivable magnitude. Parallelization in high performance computing overcomes the limits of single processors and gives access to methods allowing us to solve problems of quite stunning complexity.

This progress in computational technologies coupled with advances in software engineering opens new routes in the development of most scientific disciplines, reforming the scientific method itself.

The success of the scientific method can be attributed to self-correction, through which science aims at the best fitting model. Based on accumulated empirical knowledge, through repeated observation of nature, the conclusions are drawn. These conclusions eventually contribute to formation of more accurate scientific theory. Up until the time computers became widely available experiments were the only means of scientific investigation and theory used mostly as a tool for interpretation. Due to the nature of experiments, which often are subject to fine tuning of the apparatus and experimental procedure, considerable time is usually required. The computer simulation allows one to greatly extend the theoretical side and to accelerate the feedback part of the process. It also provides the mechanism, by which the accuracy and the level of detail is greatly improved. Furthermore, if successful replication of the real phenomena is achieved, the simulation can be used as an independent research tool. In this way the usual order of scientific procedures is often reversed: trial simulations can gauge the consequences and potential

processes linked to a particular setting, and can thus be used to guide experiments. This is happening today in many fields of physics and chemistry, in chemistry most notably in catalysis, organic and inorganic chemistry, and surface chemistry.

Of course the range of possible environments and systems accessible to computer simulations is limited. Even so, there are plenty of problems that are approachable and to which the questions have not yet been provided. Based on a chosen theory a computational algorithm is built which allows the reconstruction of the experimental set-up or more likely just a selected part of it.

This thesis is based on the results obtained from computational *ab-initio* quantum mechanical methods, specifically on the very successful density functional theory, which is introduced in a dedicated chapter. The theoretical and computational aspects are introduced in the first part of the thesis.

The second part is concerned with specific systems of interest and the obtained results. For the most part of the thesis the systems discussed can be categorized as a part of surface science where the range of different phenomena are analysed, with the exception of the last chapter which talks about bulk structures.

1.2 Overview

The presentation encompasses the following systems: in **Chapter 7** the silicon surfaces will be introduced to provide the background of the later presented results. In **Chapter 8** a further analysis of the Si(100) surface will be provided in the context of surface pinning phenomena by dissociated water molecules. **Chapter 9** describes adsorption of single molecules to determine the basic properties of the investigated systems. The single molecule study is very important for understanding the basic characteristics of the investigated system. It allows one to simplify the problem to just the molecule–surface interaction without having to consider the intramolecular interactions thus greatly reducing its complexity. This type of work is necessary before including any extra variables present in the higher coverage regime when molecular interactions may become significant. Only after having a well understood foundation, is it reasonable to focus on the interactions of molecules. In the next chapter such high coverage systems are investigated, firstly with the analysis of benzene adsorption **Chapter 10**, investigating the surface mediated interactions and, secondly, with the second part of **Chapter 8** investigating high coverage water adsorption. In the

final chapter, **Chapter 11**, the subject of photovoltaic thin films absorbers is introduced, and the analysis of one particular grain boundary type is undertaken for a group of thin film photovoltaic absorbers, which are the subject of intense research in photovoltaics today.

Part I

Theoretical background

Chapter 2

Introduction

2.1 Solid state theory

Solid state physics and chemistry are governed by the laws of quantum mechanics (QM). Ideally, it would therefore be preferential to model them by QM alone. However, obtaining a full QM description of many-body systems is not always possible due to the inherent computational complexity. This is the reason why many of the large systems are still described using classical models based mainly electrostatic interactions. Currently, new and more sophisticated methodologies and computational tools are being developed, which allow more problems to be tackled by genuine QM methods.

There are two main philosophies in approaching quantum mechanical problems. The first one is called *ab-initio* (latin: from the beginning) and it is a purely theoretical approach. The input to *ab-initio* calculations is limited only to the fundamental constants and atomic numbers of nuclei. The accuracy of the results obtained using this method depends on the model's capacity to correctly represent the wave function, which is indirectly limited by the computational power available.

The alternatives to this purely theoretical approach are semi-empirical methods, which use some empirical data to either increase the accuracy of the obtained results, or to simply limit the computational cost. However, since the results obtained using these methods are experimentally deduced, they are often system sensitive. In my studies I mainly used *ab-initio* method. However, semi-empirical methods have been employed to correct for the dispersion interaction. In this chapter I will introduce the origins and foundations of the theories used in electronic structure calculation leading to Density Functional Theory (DFT), which is the core of all the calculations in the thesis. I will also introduce some technical details involved in performing DFT calculations together with extensions to the general theory,

and more specialised topics such as, scanning tunnelling microscopy, nudged elastic band, and delta self consistent field methods.

2.2 Many-body wavefunctions

In order to fully appreciate the complexity of a many-body system, it is natural to first outline a many-body formulation of the Schrödinger equation (SE). Let us consider a simple form of the SE, which is a time independent representation of a spin-less and non-relativistic many body system, with M atoms and N electrons. Such an equation reads:

$$\widehat{H}\Psi(\mathbf{r},\mathbf{R}) = E\Psi(\mathbf{r},\mathbf{R}), \tag{2.1}$$

where the wavefunction Ψ depends on coordinates $\mathbf{r}$ of N electrons and $\mathbf{R}$ of M nuclei,

$$\mathbf{r} = (\mathbf{r}_1, \mathbf{r}_2, .., \mathbf{r}_N), \mathbf{R} = (\mathbf{R}_2, \mathbf{R}_2, .., \mathbf{R}_M). \tag{2.2}$$

The total kinetic energy in such a system is defined as a sum of the kinetic energies of all electrons and all nuclei,

$$E_{kin} = \sum_{k=1}^{M} \frac{P_k^2}{2M_n} + \sum_{i=1}^{N} \frac{p_i^2}{2m_e}. \tag{2.3}$$

The potential energy is attributed to the electrostatic interactions between all the charges, which yields three possible interactions: ion–ion, electron–electron, and electron–ion:

$$\begin{aligned} E_{pot} =& \frac{1}{2} \sum_{k_1 \neq k_2 = 1}^{M} \frac{1}{4\pi\epsilon_0} \frac{Z_{k_1} Z_{k_2} e^2}{|\mathbf{R}_{k_1} - \mathbf{R}_{k_2}|} + \frac{1}{2} \sum_{i_1 \neq i_2 = 1}^{N} \frac{1}{4\pi\epsilon_0} \frac{e^2}{|\mathbf{r}_{i_1} - \mathbf{r}_{i_2}|} \\ & - \sum_{k=1}^{M} \sum_{i=1}^{N} \frac{1}{4\pi\epsilon_0} \frac{Z_k e^2}{|\mathbf{R}_k - \mathbf{r}_i|}. \end{aligned} \tag{2.4}$$

In contrast to two other contributions the nuclei-electron potential energy contribution is negative due the attractive nature of this interaction. There may also be additional terms to the Hamiltonian due to the influence of external electric or magnetic fields. These, however, are not considered here. The Hamiltonian for the total energy can be expressed as the sum of all component Hamiltonians namely two kinetic components and three potential energy components.

$$\widehat{H} = \widehat{H}_{k,n} + \widehat{H}_{k,e} + \widehat{H}_{p,n-n} + \widehat{H}_{p,n-e} + \widehat{H}_{p,e-e} \tag{2.5}$$

$$\widehat{H} = -\sum_{k=1}^{M} \frac{\hbar^2}{M_k} \nabla^2_{\mathbf{R}_k} - \sum_{i=1}^{N} \frac{\hbar^2}{2m_e} \nabla^2_{\mathbf{r}_i} + \frac{1}{2} \sum_{k_1 \neq k_2 = 1}^{M} \frac{1}{4\pi\epsilon_0} \frac{Z_{k_1} Z_{k_2} e^2}{|\mathbf{R}_{i_1} - \mathbf{R}_{i_2}|}$$
$$+ \frac{1}{2} \sum_{i_1 \neq i_2 = 1}^{N} \frac{1}{4\pi\epsilon_0} \frac{e^2}{|\mathbf{r}_{i_1} - \mathbf{r}_{i_2}|} + \sum_{k=1}^{M} \sum_{i=1}^{N} \frac{1}{4\pi\epsilon_0} \frac{Z_k e^2}{|\mathbf{R}_k - \mathbf{r}_i|} \tag{2.6}$$

Considering the evaluation of the above equations for N electrons and M atoms it becomes apparent that for only a few atoms one is already faced with very large amount of variables. Solutions for realistic systems thus will be impossible. In order to overcome this issue a variety of approximations need to be used.

2.2.1 Born-Oppenheimer Approximation

The Born-Oppenheimer (BO) approximation is one of the most fundamental approximations of computational chemistry. It is based on the recognition of the large difference in mass between electrons and ions and the times-scales that are involved in their dynamics. The large mass difference is causing nearly instantaneous reaction in electrons while keeping the positions of ions fixed by comparison. Thus, in many cases in condensed matter problems, the nuclei can be treated adiabatically i.e. the dynamics of electronic wave-functions can be seen as if it takes place in a static ionic potential energy landscape.

This implies the possibility of dividing the ionic and electronic degrees of freedom, which allows their independent treatment,

$$\Psi(\mathbf{R}, \mathbf{r}) = \psi_n(\mathbf{R}) \psi_e(\mathbf{r}). \tag{2.7}$$

The ionic kinetic energy term can be neglected, or if necessary treated as a small perturbation. This significantly simplifies the system. The first step in applying the adiabatic approximation is to exclude the ionic kinetic energy contribution from the Hamiltonian. The electronic wave function depends parametrically on the specific position of the nuclei. Consequently, a SE applying to electrons alone can be formulated:

$$H_e \psi_e = E_e \psi_e \tag{2.8}$$

and the electronic Hamiltonian is

$$\widehat{H}_e = -\sum_{i=1}^{N} \frac{\hbar^2}{2m_e} \nabla^2_{\mathbf{r}_i} + \frac{1}{2} \sum_{i_1 \neq i_2 = 1}^{N} \frac{1}{4\pi\epsilon_0} \frac{e^2}{|\mathbf{r}_{i_1} - \mathbf{r}_{i_2}|} + \sum_{k=1}^{M} \sum_{i=1}^{N} \frac{1}{4\pi\epsilon_0} \frac{Z_k e^2}{|\mathbf{R}_k - \mathbf{r}_i|} \tag{2.9}$$

After introduction of the BO approximation one can find the ground state configuration in a variational minimization of energy,

$$min \left\{ \frac{\left\langle \psi_e | \widehat{H}_e | \psi_e \right\rangle}{\langle \psi_e | \psi_e \rangle} \right\} = E, \tag{2.10}$$

while the optimal ionic coordinates can be found via the negative derivative of the total energy of the systems with respect to the ionic position $\mathbf{R}_I$ which provide the force on the nuclei.

$$F = -\frac{dE}{d\mathbf{R}_I} \tag{2.11}$$

Although the BO approximation significantly simplifies many-body problem, all the electrons are still treated as separate and interacting entities leaving one with a significant computational challenge. There is no conceivable way to extend the many-body wavefunction methodology to any realistic condensed matter problem including at least 100–1000 electrons. The BO approximation alone is not sufficient, other approximations need to be present or the many-body wave function needs to be avoided altogether.

2.2.2 Wavefunctions and density functionals

In general, in modern studies of electronic structure two different routes can be recognized. On the one hand, there are wavefunction-based methods following the work of Hartree, Fock and Slater. On the other hand there are density-based methods derived from work of Thomas, Fermi, and Dirac, and later formulated in a Density Functional Theory (DFT) by Kohn and Sham. The wavefunction approach, known under a name of Hartree–Fock (HF), is a linear combination of wavefunctions, represented by a set of basis functions. The electron wave functions are anti-symmetric in nature, thus change their sign upon exchange. In order to satisfy the Pauli exclusion principle, the antisymmetric property of the wavefunction is encapsulated by utilization of a Slater determinant,

$$\Psi(\mathbf{r}_1, \mathbf{r}_2, \ldots, \mathbf{r}_N) = \frac{1}{\sqrt{N!}} \begin{vmatrix} \chi_1(\mathbf{r}_1) & \chi_2(\mathbf{r}_1) & \cdots & \chi_N(\mathbf{r}_1) \\ \chi_1(\mathbf{r}_2) & \chi_2(\mathbf{r}_2) & \cdots & \chi_N(\mathbf{r}_2) \\ \vdots & \vdots & \ddots & \vdots \\ \chi_1(\mathbf{r}_N) & \chi_2(\mathbf{r}_N) & \cdots & \chi_N(\mathbf{r}_N) \end{vmatrix}. \tag{2.12}$$

where χ_N are orthonormal spin orbitals, each a product of a spacial orbital and the spin up or spin down function. In DFT, the electrons are no longer expressedf as complex wavefunctions but as a real electron density. This offers substantial computational advantage over wavefunction based methods. Similarly to HF, DFT has achieved a great recognition and has proven to be valid in a wide range of condensed matter systems, calculating binding energies of molecules and the band structure of solids or even molecular systems in biology. DFT offers a complementary perspective on a quantum system. It focuses on quantities in 3–dimensional space, principally on the ground-state electron density, and provides a simpler and more intuitive visualization of even larger systems. It so far has proven its reliability in many similar systems to the ones investigated here, with limited computational cost. For this reason it is the method of choice for calculations performed in this thesis .

Chapter 3

Density functional theory

The initial work on DFT was reported in two publications: the first by Walter Kohn and Pierre Hohenberg in 1964 [1] regarding the fundamental theorems. The second one by Walter Kohn and Lu Sham in 1965 [2] giving rise to the Kohn-Sham (KS) equations. The introduction of KS equations gave rise to the new field of DFT, which together with the concepts of pseudopotentials (Section 5.6), supercells (Section 5.1) and iterative minimization techniques (Section 3.4) have revolutionized the theory of condensed matter.

In this section the basic ideas behind DFT will be introduced. It is important to remember, however, that DFT is not the first theory to include electron density. But in contrast to its predecessors, such as the model proposed by Thomas and Fermi, it is for the first time meant to be exact. It proposes the density as a fundamental entity mapping it uniquely onto the wavefunction,

$$\psi_N(\mathbf{r}_1, \mathbf{r}_2, ..., \mathbf{r}_N) \leftrightarrow \rho(\mathbf{r}), \tag{3.1}$$

and it is based on the proof that the knowledge of the ground state density of electrons is sufficient to determine all observable properties of an electronic system. This means that we do not need the full wavefunction but only the electron density, and that any observable of the many-body wavefunction $\psi_{0,N}$ can be formulated as a functional of density $\rho_o(\mathbf{r})$

$$O_0 = O\left[\rho_0\right] \tag{3.2}$$

Since this is not a trivial conclusion it requires a mathematical proof of validity.

3.1 Hohenberg and Kohn Theorems

The first proofs for the above postulates were presented by Hohenberg and Kohn in the form of two simple theorems.

3.1.1 Existence theorem

One assumes $\rho(\mathbf{r})$ to be a non-degenerate ground state density of N electrons placed in the external potential $V_1(\mathbf{r})$, which is corresponding to the ground state wavefunction with its energy eigenvalue E_1:

$$\begin{aligned} E_1 &= \left\langle \psi_1 | \widehat{H}_1 | \psi_1 \right\rangle \\ &= \left\langle \psi_1 | \widehat{T} + \widehat{U} | \psi_1 \right\rangle + \left\langle \psi_1 | \widehat{V} | \psi_1 \right\rangle \\ &= \int \psi_1^* \left(\widehat{T} + \widehat{U} \right) \psi_1 d\tau + \int \psi_1^* V_1 \psi_1 d\tau \\ &= \int \psi_1^* \left(\widehat{T} + \widehat{U} \right) \psi_1 d\tau + \int V_1 n(r) \tau. \end{aligned} \tag{3.3}$$

Here, $\widehat{T}$ is the kinetic energy and $\widehat{U}$ is the electron–electron interaction energy. They operate independently of a external potential $\widehat{V}$. If one assumes another potential producing another ground state wavefunction ψ_2 is represented by the same electron density $\rho(\mathbf{r})$, then a similar equation for E_2 can be formulated:

$$E_2 = \left\langle \psi_2 | \widehat{H}_2 | \psi_2 \right\rangle = \int \psi_2^* \left(\widehat{T} + \widehat{U} \right) \psi_2 d\tau + \int V_2 n(r) d\tau \tag{3.4}$$

Since the ground state wavefunction is non-degenerate the following can be deduced:

$$\psi_1 \neq \psi_2 \tag{3.5}$$

$$E_1 < \left\langle \psi_2 | \widehat{H}_1 | \psi_2 \right\rangle = E_2 + \int \left(V_1(r) - V_2(r) \right) n(r) d\tau \tag{3.6}$$

and

$$E_2 < \left\langle \psi_1 | \widehat{H}_2 | \psi_1 \right\rangle = E_1 + \int \left(V_2(r) - V_1(r) \right) n(r) d\tau \tag{3.7}$$

from this it follows that:

$$E_1 + E_2 < E_1 + E_2. \tag{3.8}$$

Thus, by the *reductio ad absurdum*, the existence of the second potential V_2, giving rise to the same electron density is disproved. This proves the existence of a unique relation between the external potential and the electron density. This leads to the conclusion that the ground state charge density provides a complete description of the system properties via the solution of a time independent Schrödinger equation. Thus any ground state property

is a functional of the electron density. This theorem only proves, that a functional representation exists, however it does not define what it is.

3.1.2 Variational Theorem

In this theorem the variational energy minimization is discussed in terms of the positive electron density, which integrates to the total electron number N in the system.

$$N = N\left[\rho(\mathbf{r})\right] = \int d\mathbf{r}\rho(\mathbf{r}) \tag{3.9}$$

If one assumes the existence of a ground state $\rho_0(\mathbf{r})$, it is the density of electrons that determines the total ground state energy E_0. We know that $\rho(\mathbf{r})$ can be calculated from the square of the ground state N-electron wavefunction.

$$E_0 = E_0[\rho(\mathbf{r})] = \left\langle \psi_0 | \widehat{H} | \psi_0 \right\rangle \tag{3.10}$$

knowing that the energy expectation value of the ground state wavefunction and the energy functional of the density obtained from this wavefunction defines uniquely (for a non-degenerate case) the ground state energy of the system. Let us propose another wavefunction $\psi_1(\mathbf{r})$ and another corresponding density $\rho_1(\mathbf{r})$, which by the variation principle will necessary give a higher energy:

$$E_0 = E[\rho_0(\mathbf{r})] = \left\langle \psi_0(\mathbf{r}) | \widehat{H} | \psi_0(\mathbf{r}) \right\rangle < \left\langle \psi_1(\mathbf{r}) | \widehat{H} | \psi_1(\mathbf{r}) \right\rangle = E[\rho_1(\mathbf{r})] = E_1 \tag{3.11}$$

From this it follows that the total energy of the system can be found by a minimization with respect to $\rho(\mathbf{r})$, and that the minimum energy corresponds to the system with the correct electron density $\rho_0(\mathbf{r})$

3.2 N, V– representability and constrained search

Despite the fundamental nature of the above proofs of DFT theory, the HK theorems raise many questions regarding the one-to-one correspondence between the electron density and the external potentials. There have been a few generalizations showing that in fact the HK theorem is only a limited case. Fortunately, in most calculations these limits are not an issue. The one failure of HK formulation which is often discussed regards the degenerate wavefunction for which one can no longer talk about the uniqueness of the ground state expectation value.

This problem has been tackled by Levy and Lieb (LL) [3, 4]. The HK formulation is based on the assumption that the density $\rho(\mathbf{r})$ is V–representable, which means that the density is defined by some external potential.The LL theorem provided an alternative formulation in which instead of a V–representable density the minimization algorithm only required the N–representability. By such a definition they avoided the problem of how an arbitrary density, integrable to number of N electrons, could be represented by the ground state of a smooth external potential.

Employing this idea it is possible to constrain the search of the ground state wavefunction from the full space to the sub-space limited to all the wavefunctions which construct the same electron density $\rho(\mathbf{r})$. In that way the minimizations can be performed in two steps instead of one, greatly decreasing the cost of calculation.

$$E_0 = min_\rho \left\{ min_{\psi\to\rho} \left[\left\langle \psi | \widehat{T} + \widehat{U} | \psi \right\rangle + \int V(\mathbf{r})\rho(\mathbf{r}) d\mathbf{r} \right] \right\} \tag{3.12}$$

$$E_0 = min_\rho E\left[\rho\right] \tag{3.13}$$

The LL formulation is defined for any density that is derivable from the wavefunction ψ_N of N electrons, therefore it is N–representative. While LL eliminates the V–representability condition from the domain of variation, nonetheless the density of the minimum energy solution is still V–representable, agreeing with HK even for the degenerate case.

If ψ can be calculated from ρ and vice-versa then both functions contain exactly the same information. The ground state wavefunction not only reproduces the ground state density but also minimizes the energy of the system.

3.3 Self-consistent Kohn-Sham equations

Up to this point, we know that the density $\rho(\mathbf{r})$ can be used to fully represent a many-body system, thus reducing the many-body problem to a single–body problem. HK and LL have proved that a system can be exactly described only by means of $\rho(\mathbf{r})$, but it was still left unclear how this can be done. DFT can be implemented in many ways, from which the most widely used is the Kohn-Sham approach. Interestingly, this approach does not exclusively work in terms of the charge density but employs also a special type of wave functions called Kohn–Sham orbitals. As a consequence, DFT looks like a

single particle theory although many particle effects are still included via the so-called exchange-correlation potential.

In order to accommodate the electron interaction the Hamiltonian is

$$\widehat{H} = T_s + V_{eff} \tag{3.14}$$

where T_s is the kinetic energy of non-interacting electrons, while V_{eff} is an effective potential of following form,

$$V_{eff} = V_{ext} + V_H + V_{XC}. \tag{3.15}$$

where the Hartree potential is (in atomic units)

$$V_H(r) = \int \frac{\rho(\mathbf{r}')}{|r - r'|} d^3r' \tag{3.16}$$

and the exchange-correlation potential is

$$V_{xc}(\mathbf{r}) = \frac{\delta E_{xc}[\rho(r)]}{\delta \rho(\mathbf{r})} \tag{3.17}$$

V_{ext} is an external ionic potential. The exchange-correlation potential V_{xc} is a functional of the electron density, with the electron density defined as follows.

$$\rho(r) = \sum_i \mid \phi_{KS(r)} \mid^2 \tag{3.18}$$

The Kohn-Sham equations are used iteratively. They provide the framework for finding the exact density and energy of the ground state of the system.

$$(-\hbar^2\nabla^2/2m + V_{eff})\phi_{KS}(r) = E_{KS}\phi_{KS}(r) \tag{3.19}$$

The Kohn-Sham equations map many-electron systems onto a system of non-interacting electrons moving in the effective potential due to all the other electrons. As shown by Hohenberg and Kohn, DFT is an exact reformulation of the interaction for a many-electron ground state problem but the difficulty lies in the formulation of the unknown exchange-correlation energy functional.

The Kohn-Sham eigenvalues are not strictly speaking the energies of the single electron states but rather the derivatives for the total energy with respect to the occupation numbers of these states. DFT calculations are focused on iterative solution of the eigenvalue problem once an approximate expression for exchange correlation energy is given. The minimum energy of the total functional is the ground state energy and the obtained electron density

is the exact ground state single particle density. The exchange-correlation potential is given as the functional derivative of exchange correlation energy functional with respect to density.

The meaning of KS orbitals is often confused with a standard wave-function representation. It is important to highlight the fact that the KS eigenvalues are introduced as completely artificial objects. They are results of auxiliary single body equations, even though the eigenfunctions (KS orbitals) yield the correct density. The density has a strictly physical meaning while KS eigenvalues provide only semi-quantitative information of the energy spectrum. Given this nature of KS eigenvalues it is surprising that they provide a reasonable approximation to the energy levels.

DFT is a very popular method for band structure calculations in solid state physics. It has also been shown to be in good agreement with experimental studies. It has been also used to perform band structure studies in this thesis. Nonetheless, it is important to remember that the extent of its validity is not yet clearly known. DFT also is not a rigorous many-body theory but a mean field theory. The neglect of the derivative discontinuity by LDA and GGA functionals leads to an underestimation of the band gap which is most severe in metal oxides or strongly correlated systems.

3.4 Solutions to Kohn-Sham equation: Algorithms

In the process of solving the KS equations a few essential components have to be taken into account for efficient and accurate calculations.

- Introduction of effective valence-core potentials via pseudo-potentials, approximating the core electrons
- Choice of periodic boundary conditions or isolated clusters
- Choice of basis set for one-electron wave-functions: de-localized plane waves, or localized atomic orbitals
- Efficient diagonalization of Hamiltonian matrix obtained from the representation of the one electron Schrödinger equation in the basis set

In any numerical implementation a many-electron problem has to be solved iteratively. The reason is the inherent non-linearity of the fundamental Kohn–Sham equations. While in a single step of the iteration the Kohn–Sham eigenvalues and eigenvectors can be calculated on the basis of an existing density distribution, the summation of the charge density over all eigenstates creates a new potential. The final result can thus not be predicted

from one iteration only. The rough structure of an electronic self-consistent iteration cycle is the following [5].

1. From an existing distribution of ions and electron density ρ_0 construct the various components of the potential: the external potential V_{ext} (summation over ions, e. g. by Ewald summation), the Hartree potential V_H (solving the Poisson equation for the charge distribution) and the exchange–correlation potential V_{xc} (determined point by point from the density distribution). The sum of all potentials gives the effective potential in the single-electron Kohn–Sham equation:

$$V_{eff}(\mathbf{r}) = V_{ext}(\mathbf{r}) + V_H(\mathbf{r}) + V_{xc}(\mathbf{r}) \tag{3.20}$$

2. Solve the corresponding Kohn–Sham equations either by matrix inversion if the Hamiltonian is represented in a discrete basis set, or by some other method e.g. using trial solutions and a predictor-corrector scheme:

$$\left(-\frac{\hbar^2}{2m}\nabla^2 + V_{eff}\right)\Phi_{KS}(\mathbf{r}) = E_{KS}\Phi_{KS}(\mathbf{r}) \tag{3.21}$$

3. Calculate the total energy from the various contributions. The total energy in a system is described by a sum over the eigenvalues of occupied states and some corrections:

$$E_{tot,step} = \sum_i^N E_{KS,i} - E_H\left[\rho\right] + E_{xc}\left[\rho\right] - \int V_{ext}(\mathbf{r})\rho(\mathbf{r})d\mathbf{r} \tag{3.22}$$

4. See if the energy is equal to the previous one. If yes stop the iteration. Check the energy difference between the obtained energy and the energy calculated of the previous step. If it is smaller then the set threshold value stop the calculation. The ΔE are usually set small around $1meV$ for good quality calculations

5. If the difference is still larger, then sum up all density contributions from the occupied states and create a charge density:

$$\rho_{new}\left(\mathbf{r}\right) = \sum_i^N \left|\Phi_{KS,i}(\mathbf{r})\right|^2 \tag{3.23}$$

6. Admix a part of the new charge density to the old charge density ρ_0 to create a charge density ρ_1: This procedure is called mixing. It is necessary to retain numerical stability of the simulation. Several

schemes exist to admix a new charge density to the original one. In some of those schemes an array of charge densities is kept and mixed in such a way that the difference between the densities gradually goes to zero.

$$\rho_1(\mathbf{r}) = Mix\left[\rho_0(\mathbf{r}), \rho_{new}(\mathbf{r})\right] \tag{3.24}$$

7. With this density go back to step 1.

   The self–consistent electronic iteration procedure is usually embedded in a cycle aimed at achieving the ground state positions of all ions. In this case the Hellman–Feynman forces (see Appendix I for details)on the ions are calculated after the electronic ground state is achieved, and the ions moved according to the forces acting on them. Depending on the system, the electronic self–consistency cycle in today's codes takes about 10–50 iterations. Ionic relaxation depends strongly on the initial guess for the ionic positions and can take from about 10 to a few hundred cycles.

3.5 Exchange and Correlation

DFT offers a way to avoid the enormous complexity arising from electron-electron interactions in many-body systems and substitutes it with the effective one electron potential, a functional of the electron density only. Although the exact form of the functional is not known, its various approximations have allowed prediction of many properties of molecules and solids. In the search for the perfect functional a wide variety of approximations has been created. The functionals proposed so far are usually more valid for specific systems and tasks, dividing them into separate groups. Some of these functionals are not strictly *ab-initio* and include empirical parametrizations enabling them to obtain results of higher accuracy, or they decrease the cost of the calculations. While these methods are fairly successful for very similar systems they can produce highly inaccurate results for inadequate ones. A good example of this problem would be a functional such as B3LYP [6, 7], which is the most popular functional in the quantum chemistry community for calculations of small molecules, while producing inadequate results for systems containing a homogeneous electron gas. The other approach to design the exchange-correlation functionals is to reproduce as many exact constraints of the many-body system as possible. This approach aims to

produce functionals with a much more flexible range of applications, their creation is however not without difficulties [8].

Although DFT is an exact description in principle, all problems are hidden in defining the exchange-correlation energy functional $E_{XC}(n)$. The great success of DFT depends on the unexpected accuracy of simple approximations. The first approximation was based on the local density approximation (LDA) using the exchange correlation energy of a homogeneous electron gas with the density equal to the local density. The LDA has been very successful in the solid state, but does not work well for molecules where there are strong variations in their electron density. This weakness was partially removed by the construction of gradient corrected functionals such as GGA and semi-empirical approximations including explicit exchange such as B3LYP [6, 7], which was very successful in modelling molecular systems, or HSE03 [9] and HSE06 [10] for solid state systems. The development of better and yet computationally cheap functionals is still very much in progress.

3.5.1 Local density approximation

The local-density approximation is the simplest method for the description of exchange correlation energy [8]. In this approximation the exchange-correlation energy is obtained by assuming that the energy per electron at $\mathbf{r}$, $E_{xc}(\mathbf{r})$, is equal to the energy per electron of in homogeneous gas of the density equal to the density of electrons at this the same point, $\rho\mathbf{r}$

$$E_{xc}[\rho(\mathbf{r})] = \int \epsilon_{xc}\rho(\mathbf{r}))\rho(\mathbf{r})d^3\mathbf{r} \tag{3.25}$$

with

$$\varepsilon_{xc}(\mathbf{r}) = \varepsilon_{xc}^{hom}[\rho(\mathbf{r})] \tag{3.26}$$

Considering that a homogeneous electron gas is far from a real density distribution, the LDA approximation has nevertheless been highly successful in dealing with a broad range of systems. The reason why the uniform electron gas has such a prominent place in DFT is that it is the only system for which we know the form of the exchange and correlation energy functional exactly or at least to very high accuracy.

Despite the success of LDA, the homogeneous density was clearly not sufficient for many systems exhibiting strong electron density variation; a new method was needed, if one aimed to approach more chemical systems.

3.5.2 General gradient approximation

This approximation is an extension to the LDA, in which the exchange correlation energy was based on local density only. In this case the additional local information included the gradient of density $\nabla\rho(\mathbf{r})$. In this case the functional is able to account for the non–homogeneous electron density of the real system. The name general gradient approximation is reserved for the group of functionals which can be defined in the following way:

$$E_{xc}^{GGA}[\rho_\alpha, \rho_\beta] = \int f\left(\rho_\alpha, \rho_\beta, \nabla\rho_\alpha, \nabla\rho_\beta\right) d\mathbf{r}. \tag{3.27}$$

Furthermore, the exchange–correlation functional can be divided into separate exchange and correlation parts. It is important to realise that in both cases one is dealing with complex mathematical constructs which have been chosen to suit the boundary conditions and to obtain system specific performance. One should be aware that in this case the results of calculations are more important than the underling physics, and it is these results which often determine the mathematical model. There exist a group of different functionals which operate within a GGA frame-work for which each exchange or correlation energy can be separately accounted for. For the exchange interactions, empirically based functionals can be used such as PW91 by Perdew et al. [11], and CAM(A), CAM(B) by Handy and co-workers [12]. In addition there are purely theoretical functionals which instead of empirically aided parametrizations use rational functions of reduced density gradients. The most prominent of this kind are PBE by Perdew, Burke, and Ernzerhof [13], or its revised form revPBE proposed by Zhang and Wang [14], or recently its version RPBE [15]. From this variety the PBE and RPBE have been functionals of choice in this work.

3.5.3 Spin extension

So far the theorems introduced here were formulated for spinless densities; however, there also exists an extended approach to the DFT in which the electron density is a sum of the two separate densities representing spin–up and spin–down states. This is essential in a theory of atoms and molecules with a net spin different from zero and in solids with magnetic ordering.

$$n(r) = n(r,\uparrow) + n(r,\downarrow) \tag{3.28}$$

Even though from a purely theoretical point of view the exact functional will not depend on the spin densities (as long as the external potential is

spin independent), the approximations to it will benefit from the additional flexibility of having two instead of one variable. In particular for an open shell system with an unequal number of α (spin up) and β (spin down) electrons, a functional of the two spin densities consistently leads to more accurate results. But an improvement is also seen for certain systems in which the number of electrons is even, such as H_2 molecules at large separation, for which the unrestricted functionals perform significantly better because they allow symmetry breaking.

Just as for the simple spin compensated situation where the $\rho_\alpha(\mathbf{r}) = \rho_\beta(\mathbf{r}) = \frac{1}{2}\rho(\mathbf{r})$ there are related expressions for the exchange and correlation energies per particle of the uniform electron gas characterised by $\rho_\alpha(\mathbf{r}) \neq \rho_\beta(\mathbf{r})$, the so called spin polarized case.

Chapter 4

Dispersion interaction

As discussed above the choice of the exchange-correlation functional is very important for the simulation outcome [16]. While for large homogeneous systems, such as simple metals and semiconductors a local density approximation is appropriate, for inhomogeneous systems like transition metals, ionic crystals, compound metals, surfaces, interfaces and some chemical systems semi-local approximations such as a generalized gradient approximation (GGA) work much better. These two standard methods are cheap and easily applicable for periodic systems. However, since they are not able to describe dispersion interaction properly, they cannot be used for modelling soft matter systems, van der Waals complexes and biomolecules. In this case another extension of the method, including also non-local interactions is necessary. These non-local interactions can be also a decisive contribution in the determination of the structure of highest stability, in particular in metastable chemisorbed systems, such as the one investigated here. It has been shown that although many *ab–initio* methods are quite successful in predicting bonding energies, they perform rather poorly when estimating the dispersion interactions.

The dispersion interaction plays a very important role in many self assembly processes, ranging from simple organic molecule adsorption to protein folding, and its understanding seems to be an essential step on the way to evolve some intuition on how and when the correction should be incorporated in the calculations as not to miss any important phenomena. In general, dispersion interactions are described as interactions between two dipole moments within the electron distribution of atoms or molecules. The simplest model of dispersions is the interaction of two Drude oscillators where the instantaneous interaction between them creates an attractive interaction between them. The dispersion interaction can take the form of the series

expansion $E_{disp} = -\frac{C_6}{R^6} - \frac{C_8}{R^8} - \frac{C_{10}}{R^{10}} - ...$ where higher order terms can be neglected. The Leonard-Jones potential is often used among chemists to describe the interaction between atoms or charge-neutral molecules. It is commonly expressed in the following fashion:

$$V_{LJ} = 4\epsilon \left[\left(\frac{\sigma}{r}\right)^{12} - \left(\frac{\sigma}{r}\right)^{6} \right] \tag{4.1}$$

where ϵ is the depth of potential well σ is the distance close to the particle at which the potential is zero. The R^6 term approximates the potential from the dispersion forces while R^{12} corresponds to the repulsive Pauli exclusion force arising from the electron cloud overlap.

It has been shown in recent studies, utilizing extensions to density-functional approaches for vdW interactions, that this method is suitable to describe adsorption energies, bulk moduli and elastic constants of layered materials like graphite, boron nitride and MoS_2 [17]. It has also been concluded that in most cases the use of post-GGA methods is sufficient to obtain accurate results. However, self-consistent methods can be used in systems strongly influenced by dispersion interactions where the VdW would affect Hellman–Feynman forces during ionic relaxation calculations [18].

4.1 Non-self consistent method

The non self consistent method employed in this work is based on the approach developed by Langreth and Lundqvist where the energy values obtained from standard DFT calculations are updated by the vdW corrected correlation energies calculated separately for local and non-local interactions:

$$E^{TOT} = E^{SCF} - E_c^{PBE} + E_c^{LDA} + E_c^{nl} \tag{4.2}$$

Here, E^{SCF} is the total energy obtained from the DFT/GGA simulation, and E_c^{nl} is the non-local correlation energy calculated within the vdW code. The local part obtained using the local density approximation E_c^{LDA} substitutes earlier calculated E_c^{PBE}. E_c^{nl} is expressed as the two-centred integral:

$$E_c^{nl} = \frac{1}{2} \int \rho(\mathbf{r}) \phi(\mathbf{r}, \mathbf{r}') \rho(\mathbf{r}') d^3\mathbf{r} d^3\mathbf{r}' \tag{4.3}$$

This feature was implemented in VASP by Klimes [19]

4.2 Self consistent method DFT-D

The self-consistent method used in a work present in the following chapters was based on semi-empirical Grimme corrections [20], where dispersion corrections take the form of C^6R^{-6}. Within this method density functional theory is restricted to calculate the short range correlation energies, while medium to long range correlation energies are described by damped empirical potentials given by

$$E_{disp} = -s_6 \sum_{i=1}^{N_{at}-1} \sum_{j=1+1}^{N_{at}} C_6^{ij}/\mathbf{R}_{ij}^6 * f_{dmp}(\mathbf{R}_{ij}) \tag{4.4}$$

Here, N_{at} is the number of atoms in the system, C^6 is the dispersion coefficient for pair of atoms, s_6 is a scaling factor depending on the functional used, and R_{ij} is the distance between interacting atoms. The f represents a damping function of the following form:

$$f_{dmp}(\mathbf{R}_{ij}) = 1/(1 + e^{-d(\mathbf{R}_{ij}/\mathbf{R}_{ij}-1)}) \tag{4.5}$$

The total energy is then given by:

$$E^{TOT} = E_{DFT} + E_{disp} \tag{4.6}$$

Chapter 5

Technical aspects

5.1 Periodicity: Bloch theorem

Periodicity plays a very important role in computational analysis. The identification of the symmetry allows one to minimize the computational cost by avoiding multiple calculations of the same problem.

Many of the systems in condensed matter physics as well as chemistry are periodic (e.g. crystals, wires, tubes, polymers). The symmetry of these systems can be used, and their size reduced to the smallest repeatable unit. Usually this is done by reduction to the unit-cell or surface super-cell size but sometimes its multiples are necessary to more accurately model the phenomena of interest. This type of case may include: isolated molecules, molecules on the surface, defects, doping where one often does not want to model such unrealistic systems with 20 % doping or defect concentration. In these cases a larger unit cell may be required to reduce the interactions between defects, molecules, etc., from the neighbouring periodic images. Although this technique is far from ideal it is certainly a good approximation for a large enough cell. In the calculations of isolated molecules or surfaces high quality results are reached by introducing a large vacuum in between the periodic images, thus decreasing the molecule–molecule or surface–surface image interaction to a negligible value.

In the single-electron description in a periodic potential $V(\mathbf{r}) = V(\mathbf{r}+\mathbf{R})$, the Hamiltonian is invariant under the lattice translations. Which means that it commutes with the translational operator.

$$\left[\widehat{H}, \widehat{R}_T\right], \widehat{R}_T = n_1\mathbf{a}_1 + n_2\mathbf{a}_2 + n_1\mathbf{a}_2 \tag{5.1}$$

$$n_1, n_2, n_3 = 1, 2, 3, ... \tag{5.2}$$

According to Bloch's theorem [5] the wavefunction can then be written as a product of a plane wave and the lattice periodic function,

$$\psi_{\mathbf{k}} = \exp(i\mathbf{kr})u_{\mathbf{k}}(\mathbf{r}) \tag{5.3}$$

where $u_{\mathbf{k}}(\mathbf{r})$ has the same periodicity as the potential, which in the reciprocal space leads to:

$$\psi_{\mathbf{k}} = \sum_{\mathbf{G}} C_{\mathbf{k}+\mathbf{G}} \exp(i\mathbf{r}(\mathbf{k}+\mathbf{G})) \tag{5.4}$$

where C is a Fourier coefficient and G is reciprocal space lattice vector. The important conclusion from Bloch's representation is that although the wave function phase is not transitionally invariant the charge density $\rho(r) = \psi(r)\psi(r)^*$ is. Therefore, the use of Bloch theorem allows for the periodic representation of systems with ($\mathbf{r}$+$\mathbf{R}$) translational symmetry such as the electron density in a periodic lattice potential.

5.2 Density of states

The density of states is the number of states per unit energy per unit volume. Under the periodic boundary condition the volume of each wavevector point in three dimentional space is

$$\delta\mathbf{k} = (\frac{2\pi}{L})^3 \tag{5.5}$$

In the reciprocal space the number of states in the shell from k to $k+dk$ is

$$dN = 2(\frac{L}{2\pi})^3 int_k^{k+dk} d\mathbf{k} \tag{5.6}$$

Then for the dispersion relation$E(k) = \hbar^2k^2/2m$, one can obtain the following density of states

$$g(E) = \frac{1}{L^3}\frac{dN}{dE} = \frac{1}{2\pi^2}(\frac{2m}{\hbar^2})^{3/2}E^{1/2}. \tag{5.7}$$

5.3 Basis set

5.3.1 Plane wave versus local functions

The basis can be formed from a set of plane waves or some localized functions. Both of the methods have advantages and disadvantages, depending on the system and the research interest. Within the plane wave methods it is easy to change between real and momentum space, through utilization of the Fast

Fourier Transforms (FFT). The kinetic and potential energy are then represented diagonally. Plane waves offer very simple convergence control and their adjustment through a cut-off energy. The Hellmann-Feynman forces [5] can also be easily calculated with respect to ionic coordinates and superposition errors from the local basis set are avoided. For convergence the nodal character of the valence orbitals needs to be eliminated and ion-electron interactions described by pseudo-potentials. While some regard plane wave methods as an unnecessary approximation, some are sceptical about localized basis sets due to incompleteness and superposition errors. Local basis sets have certain advantages compared to plane wave basis set, and they allow analytical integration of $1/\mathbf{r}$ singularities of Coulomb potentials thus allowing fast calculation of exact exchange.

5.3.2 Plane wave basis set

Through the introduction of the Bloch theorem the single electron wavefunction can be expanded in terms of a discrete basis set. In order to describe the system perfectly, the basis set should be infinite. In practice this is approximated. Plane waves are especially appropriate for systems with long range periodicity. In such conditions they provide intuitive understanding as well as algorithms for practical calculations.

Because many of the condensed matter systems offer long range periodicity it is natural to express them using periodic functions such as 3-dimensional plane waves. Using the fact that any periodic function can be expanded into a complete set of Fourier components an eigenfunction can be written as follows:

$$\psi_i(\mathbf{r}) = \sum_q c_{i,\mathbf{q}} \times \frac{1}{\sqrt{\Omega}} exp\left(i\mathbf{q}\cdot\mathbf{r}\right) \equiv \sum_q c_{i,\mathbf{q}} \times |\mathbf{q}\rangle, \tag{5.8}$$

where $c_{i,q}$ are the expansion coefficients of the wavefunction in the basis of orthonormal plane waves $|q\rangle$, which satisfy the orthonormality condition:

$$\delta_{q,q'} = \frac{1}{\Omega}\int_\Omega exp\left(-i\mathbf{q'}\cdot\mathbf{r}\right) exp\left(i\mathbf{q}\cdot\mathbf{r}\right) \equiv \langle \mathbf{q'}|\mathbf{q}\rangle. \tag{5.9}$$

By inserting the eigenfunction into the KS equation (Equation (3.19)) and multiplying by $\langle\mathbf{q}'|$ we obtain the KS equation in Fourier space,

$$\sum_{\mathbf{q}} \langle \mathbf{q}'|\widehat{H}|\mathbf{q}\rangle c_{i,\mathbf{q}} = \varepsilon_i \sum_q \langle \mathbf{q}'|\mathbf{q}\rangle c_{i,\mathbf{q}} = \varepsilon_i c_{i,\mathbf{q}'}. \tag{5.10}$$

from that, the plane wave representation of kinetic energy is expressed as

$$\langle \mathbf{q}' | - \frac{\hbar^2}{2m_e} \nabla^2 | \mathbf{q} \rangle = \frac{\hbar^2}{2m_e} |q|^2 \delta_{\mathbf{q},\mathbf{q}'}, \tag{5.11}$$

Due to the periodicity of the crystal and its effective potential V_{eff} the only allowed Fourier components are those with the wavevectors in the reciprocal space of the crystal. V_{eff} is expressed as follows.

$$V_{eff}(\mathbf{r}) = \sum_m V_{eff}(\mathbf{G}_m) exp(i\mathbf{G}_m \cdot \mathbf{r}), \tag{5.12}$$

where G_m is a reciprocal lattice vector and

$$V_{eff}(\mathbf{G}) = \frac{1}{\Omega_{cell}} \int_{\Omega_{cell}} V_{eff}(\mathbf{r}) exp(-i\mathbf{G} \cdot \mathbf{r}) d\mathbf{r} \tag{5.13}$$

with Ω_{cell} representing the volume of a reciprocal unit cell. The matrix element of the effective potential is

$$\langle \mathbf{q}' | V_{eff} | \mathbf{q} \rangle = \sum_m V_{eff}(\mathbf{G}_m) \delta_{\mathbf{q}'-\mathbf{q},\mathbf{G}_m} \tag{5.14}$$

from which it becomes apparent that it can only be zero if the difference between q and q' is a reciprocal lattice vector $\mathbf{G}_m$. Redefining a $\mathbf{q}$ to:

$$\mathbf{q} = \mathbf{k} + \mathbf{G}_m, \mathbf{q}' = \mathbf{k} + \mathbf{G}_{m'}, \tag{5.15}$$

the matrix equation can be written,

$$\sum_{m'} H_{m,m'}(\mathbf{k}) c_{i,m'}(\mathbf{r}) = \varepsilon_i(\mathbf{k}) c_{i,m}(\mathbf{k}). \tag{5.16}$$

In this way the solutions have been transformed to a set of independent equations for each k-point within the Brillouin zone, where

$$\begin{aligned} H_{m,m'}(\mathbf{k}) &= \langle \mathbf{k} + \mathbf{G}_m | \widehat{H} | \mathbf{k} + \mathbf{G}_{m'} \rangle \\ &= \frac{\hbar^2}{2m_e} |\mathbf{k} + \mathbf{G}_m|^2 \delta_{m,m'} + V_{eff}(\mathbf{G}_m - \mathbf{G}_{m'}), \end{aligned} \tag{5.17}$$

is a matrix element of the Hamiltonian. The equations (5.16) and (5.17) are a system of linear equations, which can be solved via diagonalization and yield a set of eigenvalues $\varepsilon_i(\mathbf{k})$, one for each defined k point. On the basis of these equations the band structure can be calculated where the index i represents the band number of each calculated k-point value.

When one uses plane wave sets it becomes apparent than although the accuracy of the solutions depends on the number of PW basis function, the components for small kinetic energies are more important that large ones,

with their weight factor approaching zero for increasing energies. For that reason the plane wave basis set can be truncated. It is thus a viable option to introduce an energy cut-off value. Then the number of plane waves in the basis set is limited,

$$\frac{|\mathbf{k}+\mathbf{G}|^2}{2} < E_{cutoff}. \tag{5.18}$$

This process allows not only for a discrete but also a finite representation of the wavefunction. The use of E_{cutoff} within the DFT code allows easy control over regulation of the accuracy optimizing of the convergence.

5.4 k-point sampling

The convergence and accuracy of the calculation is also dependent on the choice of k-points. If the sampling is not sufficient to achieve convergence, the grid can be set denser, until the error due to the k point sampling becomes insignificant and the calculation result converges to a certain value. In general the number of k-points required for convergence is inversely proportional to the size of the unit cell. In DFT calculations the k-points can be set manually or according to one of the schemes for the k-point grid generation, with the most common one introduced by Monkhorst and Pack [21].

5.5 Electron bands and Brillouin zones

For perfect periodicity within the lattice one is able to obtain the reciprocal lattice via Fourier transform. The states in the system are now characterized by the wavevector with a specific eigenenergy or eigenfrequency. Due to the periodic boundary conditions certain energies are forbidden. The obtained dispersion relation can be divided into bands characterizing the properties of electrons. The dispersion relation is described within the Brillouin zone characterizing the periodic nature of a given reciprocal space. The solution of the matrix eigenvalue problem gives rise to a discrete set of eigenvalues $\varepsilon_i(\mathbf{k})$ which vary with $\mathbf{k}$ forming a unique electronic band structure.

The presence of various symmetries for the one-electron Hamiltonian reduces the number of inequivalent k points in the first Brillouin zone. For that reason it is only necessary to consider the k-points in the irreducible Brillouin zone (IBZ), while the states and energies for other k-points can be obtained through symmetry operations. Typically one visualizes bands along the symmetry lines in IBZ. Practically this of course can't be done in

a continuous manner and to obtain accurate band characterization one has to accurately enough sample the k-space along the directions of interest.

5.6 Pseudo-potentials

The idea of pseudo-potentials (PP) is to simply allow cheaper computational analysis of many-atom systems without sacrificing any of the details of chemical or physical systems. It is known that atoms in a chemical bond engage primarily due to the interaction of their valence electrons, and that the interaction of the core electrons is very small. This allows a greater flexibility when describing the core electrons. The main concept of PP is to add the tightly bound core electrons to the strong potential for the nuclei and in effect reproduce the effective ionic potential acting on the valence electrons only. The pseudo-potentials can be generated beforehand and then applied in the DFT calculation, thus reducing the cost. PP have been used both in plane wave and localized basis methods for quite some time, and although their use is very common, the process of the production of pseudo-potentials is not a straightforward one. The pseudo-potentials quality is matched against all-electron calculations. The major difficulty in the use of pseudo-potentials is due to the non-linearity of exchange interactions between valence and core electrons. In systems with high valence-core electron overlaps extensive corrections are necessary. One of the methods of dealing with this problem is to utilize projector augmented waves.

5.7 Projector augmented waves

The projector-augmented wave method, fist published by Blochl [22], is an attempt of creating a method combining the efficiency of pseudo-potential (PP) methods and the accuracy of full-potential linearised augmented-plane-wave (FLAPW) methods. Unlike PP, PAW accounts for the nodal features of the valence orbitals and ensures orthogonality between the valence and core wavefunctions. In PAW all valence electron wavefunctions ψ_i^{AE} are constructed from pseudo wave functions through the linear transformation.

$$|\psi_n^{AE}\rangle = |\psi_n^{PS}\rangle + \sum_i \left(|\varphi_i^{AE}\rangle - |\varphi_i^{PS}\rangle\right) \langle p_i^{PS}|\psi_i^{PS}\rangle \tag{5.19}$$

where pseudo wavefunction ψ_i^{PS} (of band index n) is a variational quantity expanded in the plane waves. ψ_i^{PS} is identical to the all electron wavefunction ψ_n^{AE} outside of the sphere of a PAW-potential (which has a radius

of about half of the atomic-separation), while inside of the sphere, it is only a bad approximation to the wavefunction. The all electron partial waves φ_n^{PS} are solutions to the spherical scalar-relativistic Schrödinger equation for non-spin polarized atoms while the pseudo (PS) partial waves φ_n^{PS} are node-less and identical to the AE partial waves outside of the sphere of the PAW-potential and match continuously inside of it. The p_i is a projector function which is constructed such that $\langle p_i^{PS}|\varphi_j^{PS}\rangle = \delta_{ij}$ and $\langle \mathbf{r}|p_i^{PS}\rangle = 0$ for r larger then the radius of the PAW-potential sphere.

Within the PAW method the charge density corresponding to the all electron eigenstate ψ_n^{AE}, $\rho(\mathbf{r}) = \langle\psi_n^{AE}|\mathbf{r}\rangle\langle\mathbf{r}|\psi_n^{AE}\rangle$ is composed of the three contributions to ψ_i^{PS}, φ_n^{PS} and φ_n^{AE};

$$\rho(\mathbf{r}) = \rho^{\psi_{PS}}(\mathbf{r}) + \rho^{\varphi_{AE}}(\mathbf{r}) - \rho^{\varphi_{PS}}(\mathbf{r}). \tag{5.20}$$

As discussed by Kresse [23] the PAW method gives results that are almost indistinguishable to the US-PP for materials in which the charge density closely resembles that of the reference system within the core region. However, for the materials with strong electro-negativity differences or systems with large magnetic moments PAW shows superiority over the ultrasoft pseudo-potential (US-PP). For the calculation in this thesis PAW potentials (as implemented in VASP) have been used due to their accuracy comparable to FLAPW, but under significantly reduced cost [23].

5.8 Delta Self-Consistent Field method : excited states

Another area in which DFT struggles is for systems not in their ground state. The problem of including the excited states has been approached in different ways, however, it often suffers from high costs or computational limitations. The most promising methods, because of their low cost, compatible to standard ground state calculations for tasks such as the excited state molecular energies calculations are Constrained DFT and the Self-consistent field method ΔSCF. For the first one an additional potential is used to achieve the desired amount of electrons in the area. In the ΔSCF scheme, however, the position of the electrons is controlled by the occupation of the Kohn-Sham (KS) states [24].

In this thesis in section 9.3, the method used is an extended Δ Self-Consistent Field method. The DSCF method closely resembles standard DFT; its advantage is that electrons are not restricted to occupy the lowest

possible orbitals. It allows one to place one or many electrons in higher lying Kohn–Sham orbitals. With this additional freedom it is possible to localize the excited state of adsorbed molecules and perform calculations from which resonance energies can be estimated. Furthermore, from the calculated forces it can be deduced if the resonance is responsible for molecular dynamics.

In actual calculations the density of a specified orbital $\phi_s(\mathbf{r})$ is added to the total density in each step of the self-consistency cycle [24].

$$\rho(r) = \sum_n f_{N-1}(T, \varepsilon_n) \mid \phi_n(r) \mid^2 + \mid \phi_s(r) \mid^2 \tag{5.21}$$

N is the total number of electrons and f_{N-1}(T,ϕ) is the Fermi-Dirac distribution of the N-1 electron system. ϕ_s is our chosen orbital occupied by an electron, which is taken from the Fermi level to keep the system neutral. To get the correct band energy $\phi_s(\mathbf{r})$ needs to be expanded in terms of KS orbitals,

$$|\phi_s >= \sum_n c_{ns}|\psi_n >, c_{ns} = \langle\psi_n|\phi_s\rangle \tag{5.22}$$

and the band energy becomes,

$$\varepsilon_s = \sum_n |c_{ns}|^2 \varepsilon_n. \tag{5.23}$$

5.9 Computational software

5.9.1 Vienna Ab initio Simulation Package

In this thesis all the calculations have been performed mainly using Vienna *ab–initio* simulation package (VASP). VASP is based on a Fortran code is a versatile quantum simulation environment based on the density functional theory. It is a complex package for performing ab-initio quantum-mechanical simulations using pseudo-potentials or the projector-augmented wave method and a plane wave basis set. In calculations performed for this thesis the interaction between ions and electrons have been described by the projected augmented wave (PAW). PAW method allows for a considerable reduction of the number of plane-waves per atom for transition metals and first row elements. The size of the basis-set can be kept very small even for transition metals and first row elements like C and O.

Forces and the full stress tensor can be calculated with VASP and used to relax atoms into their ground-state. As in any plane wave program, the execution time scales like N^3 for some parts of the code, where N is the

number of valence electrons in the system. In VASP, the pre-factors for the cubic parts are almost negligible leading to an efficient scaling with respect to system size.

As for the Brillouin-zone sampling VASP offers a range of meshes and schemes from explicit k–point definition to automatic mesh determination providing a flexible choice depending on the individual requirements. The above mentioned features are only brief outline of the whole package, much more information on VASP can be found on the VASP web site where one can access a practical guide as well us other useful resources on the VASP [30], while the overview of the main methods is provided in the article by Kresse and Furthmüller [31, 32].

Chapter 6

Scanning Tunnelling Microscopy

6.1 Background informations

In order to obtain atomic scale resolution with a scanning probe instrument (see Fig. (6.1)), a significant change in probe sample interaction needs to be observed within the scale of atomic units. The only interactions sensitive enough to such small displacement are chemical forces and tunneling currents and both are giving rise too two important methods, namely the scanning tunneling microscope (STM) and the atomic force microscope (AFM). Both of these methods are of tremendous importance and have revolutionised the field of surface science. In this work, however, we shall only be concerned with the first one. In surface science one of the most fundamental problems is an accurate determination of the surface structure. To this end, STM has been the leading method. STM offers high resolution of direct and real images making it one of the most favourable tools of surface analysis.

This is how it works. An atomically sharp tip is brought close to the surface and a voltage is applied. The potential difference between surface and tip causes the appearance of a tunnelling current, which is exponentially dependent on the tip–surface distance. This makes it possible to accurately determine the topography of the surface. The surface is scanned line by line and a full surface landscape is obtained. The scanning can be done in two modes depending on the expected topography of the system. Either the current or the height of the tip (z coordinate) is kept fixed while the other variable is mapped on the scanned **xy**–plane.

Although from these images the interpretation may often seem straightforward this is not always a case, and it is important to understand the exact

relation between the current, the tip and the surface of an investigated material. Depending on the potential difference the electrons participating in the tunnelling are chosen from certain "origin" states of the occupied states in the emitting material to their "destination" states to which they tunnel. Thus the availability of states on both sides of the junction is a necessary condition for tunneling to occur. From this, it is apparent that tunnelling current is a result of the topography of the surface; its atomic species, as well as its local electronic properties.

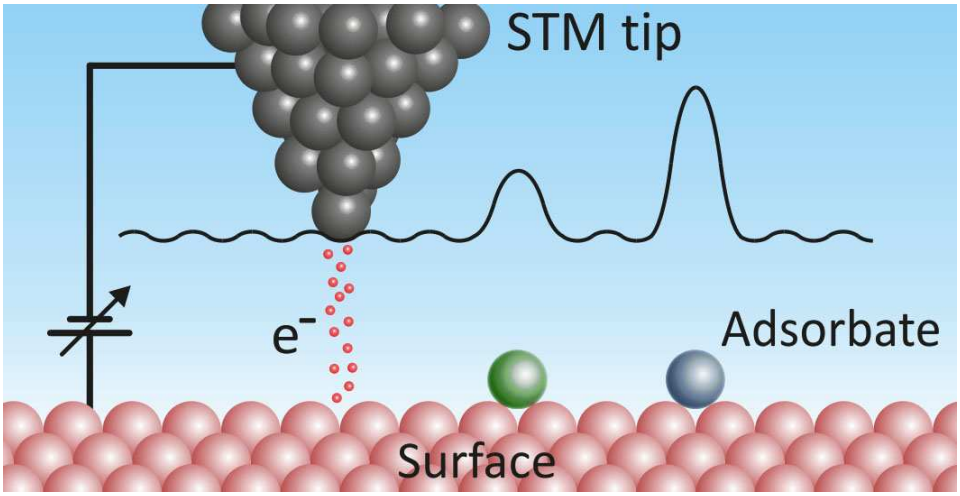

Figure 6.1: Ilustration of scanning tunnelling microscopy operation [27]

Because of the vacuum between the tip and the sample in an STM, interactions of the electrons can be considered small and the problem can be treated using perturbation models. The tunneling current to first order perturbation theory is

$$I = \frac{2\pi e}{\hbar} \sum_{\mu,\nu} f(E_\mu) \left[1 - f(E_\nu + eV)\right] \times |M_{\mu\nu}|^2 \, \delta(E_\mu - E_\nu), \tag{6.1}$$

where $f(E)$ is the Fermi function, V is the applied voltage, $M_{\mu\nu}$ is the tunneling matrix element between states ψ_μ of the probe and ψ_ν fo the surface, and E_μ is the energy state of the state ψ_μ in the absence of tunnelling.

With the current computational power the calculations of the electronic structures of the tip and the surface are feasible and the Bardeen method could by applied. Unfortunately, there is still is not enough information about the exact structure of the tip of the probe. For this reason the most commonly used technique of STM simulation is based on a very simple model proposed by Tersoff and Hamann in 1983 [28, 29]

To simplify the Bardeen method Tersoff and Hamann have restricted

the geometry of the tip to one s-like orbital. This simplification and the corresponding simplified calculation of the tunneling matrix element $M_{\mu\nu}$ yields the following expression for the tunneling current:

$$I \propto e^{2\kappa R} \sum_n |\psi_n(r_0)|^2 \, \delta(\varepsilon_n - \varepsilon_F) = e^{2\kappa R} n(r_0, \varepsilon_F) \tag{6.2}$$

where κ is the inverse decay length for the tip wave function in vacuum, R is local radius of probe's curvature. The decay length itself depends on the work function ϕ_w and the applied bias ΔV according to:

$$\kappa = \frac{\sqrt{2m_e|\phi_w - \Delta V|}}{\hbar} \tag{6.3}$$

where the ϕ_w is the work function Equation 6.2 shows that the tunneling current is proportional to the local density of states of the surface, $n(r_0, \varepsilon_F)$. Despite its simplicity this relation is very often a quite accurate description of STM images. Its drawback, however, is that it does only allow for qualitative comparisons.

6.2 BSKAN

All the STM simulations in this thesis have been performed using bSKAN by W. Hofer. bSKAN is written in modular form and is currently implemented in Fortran 90. It is an efficient tool for scanning tunnelling microscopy simulations, written on the basic of Bardeen treatment of tunneling current, and includes a Tersoff-Hamann approximation. For more informations see the bSKAN guide [34].

Part II

Analysed systems

Chapter 7

Silicon surfaces

This chapter is aimed as an introduction to the silicon surfaces discussed in this thesis. It outlines some basic phenomena observed on the clean surfaces and provides the structural informations calculated in preliminary studies.

7.1 Silicon: chemical properties

Silicon is a tetravalent chemical element with the symbol Si and atomic number 14. It is less reactive than its chemical analogue carbon, the non-metal directly above it in the periodic table, but more reactive than germanium, the element directly below in the table. Silicon is the eighth most common element in the universe by mass and second most abundant element on earth after oxygen accounting for 25.7 % of the Earth's crust by weight. However, silicon very rarely occurs as a free element in nature. It is most commonly present in a form of silicon dioxide (silica) or silicates [35].

Silicon is widely used in its available forms for building and, in the ceramic industry in the production of porcelains and quartz based lime-glass. The other silicon compounds are silicon carbides and a whole class of silicon-based polymers called silicones. Purified silicon is a base of modern technology, a corner stone of current electronics and the computing industry. As one would expect silicon also plays its part in the physics and chemistry of life, mostly as a trace element for animals but more importantly in the biology of plants. The crystalline silicon has relatively high melting and boiling temperatures of 1687 K and 3538 K, respectively.

Similarly to germanium and carbon, silicon crystallizes in a strong but brittle diamond cubic structure with a lattice parameter of 5.43 Å. Silicon is a metalloid with much lower electro-negativity than carbon (1.7 compared to 2.5 on the Allred and Rochow scale) allowing for many forms of chemical bonding. Like carbon it typically forms four bonds but it can also accept

additional electrons and form five and more bonds [35]. Its tetra-bonded chemistry provides opportunities for flexible combinations with other elements and gives rise to structurally complex chemistry, thus being the most likely candidate for an alternative biochemistry.

Its shell structure consists of $1s$, $2s$, $2p$, and $3s$ orbitals, which are completely filled, and a $3p$ orbital which contains only two electrons, adding up to four valence electrons. Silicon has a negative temperature coefficient of resistance, since the number of free charge carriers increases with temperature. The electrical resistance of single crystal silicon significantly changes under the application of mechanical stress due to the piezoresistive effect [35]. Recently it has been also discovered that silicon can exist in another anisotropic $2d$ form called silicene [36].

The electronic band structure of bulk Si has been widely studied both experimentally and theoretically [37, 38, 39, 40]. The energy of a band gap at 0°C is 1.2 eV while at room temperature it is 1.1 eV [41]. Due to the importance of silicon in modern industry the study of its properties have been of great value. Here, we are concerned with the analysis of its surface properties. The terminated bulk structure, when exposed to vacuum, usually undergoes some a reconstruction to reduce its total energy. If the reconstruction places the empty states below the Fermi surface or occupied states above it a band bending is expected and electrons flow from or to the bulk until the built-up electric field becomes strong enough to create an equilibrium. This built up field therefore corresponds directly to the band bending. Surface dangling bonds can be reduced by the formation of dimers or can be saturated by another species such as hydrogen. The bond hydrogenation causes bonding states to move to the valence band and empty states into the conduction band which flattens the band. Even though surface reconstruction minimizes the amount of dangling bonds, the shifted atomic configuration also generates surface stress which is energetically costly. For that reason not all reconstructions are easy to predict, and the most stable solutions often are due to a balance between bond saturation and surface stress.

7.2 Si(111)–(7×7) surface reconstruction

The Si(111) surface cleavage and associated reconstruction was a topic of scientific debate for many years described by a well established theoretical model called dimer adatom stacking fault (DAS). This model was first published by Takayanaki *et al.* in 1985, and instead of very simple pattern

arising from the bulk structure it proposed a new arrangement of atoms in the top three layers forming a large (7×7) unit cell, shown in Figure (7.1) [42]. The DAS model accounts for many features observed by STM, where the most visible atoms correspond to adatoms and the dark areas surrounded by hexagons of adatoms correspond to corner holes (Figure 7.2).

The trademark of this reconstruction is the existence of a 3–fold symmetry of faulted and unfaulted top layer atoms with respect to the corner hole (CH), responsible for very characteristic triangular patterns visible in STM images (Fig. 7.2). For the purpose of this work a short code in python was written to generate the reconstructed Si(111)–(7×7) surface for given bulk unit-cell lattice parameters, with a number of bulk layers and a hydrogenated bottom layer. In order to achieve a (7×7) reconstruction the first bilayer of the (111) surface cleavage has to be reorganized, this is done in four discrete steps:

1. Loss of 4 corner atoms resulting in creation of characteristic deep vacancies at the apex of the unit cell called corner holes
2. Dimerization of side atoms
3. Rearrangement of atoms in one half of a supercell creating a faulted stacking
4. Addition of 12 ad-atoms.

The obtained reconstruction is then added to a number of bulk bilayers and terminated with hydrogen atoms for saturation of dangling bonds (Fig. 7.2).

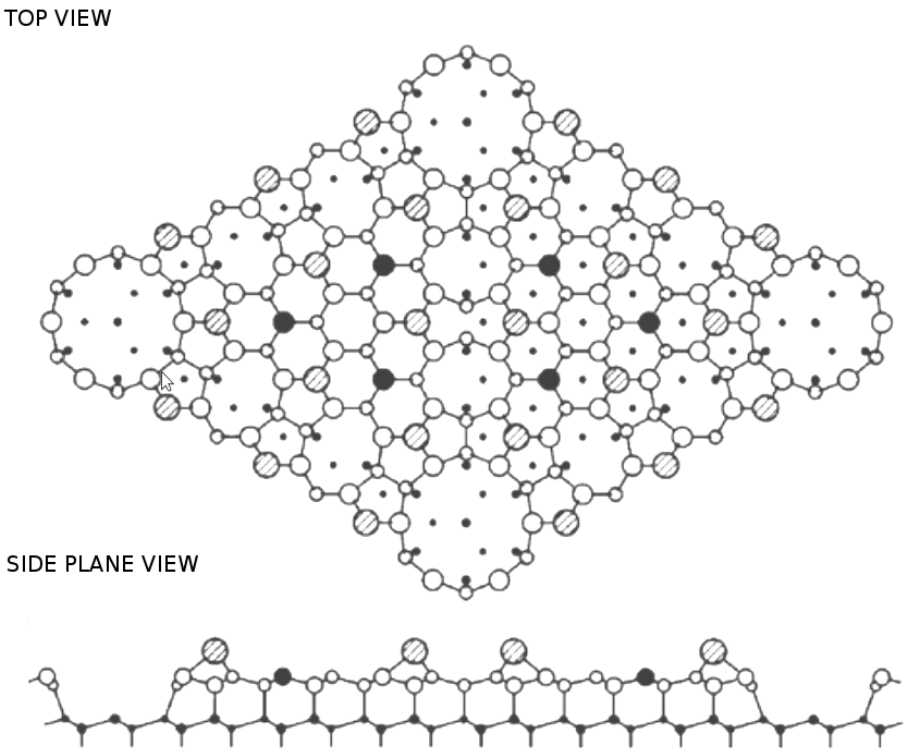

Figure 7.1: Si(111)–(7×7) surface reconstruction model proposed by Takayanaki [42]. First three layers of atoms represented as follows: dashed filling – ad-atoms, black filling – rest-atom, white filling – reconstucted bi-layer, dots – bulk bi-layer.

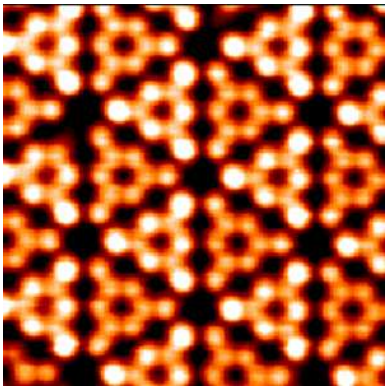

Figure 7.2: Scanning tuneling microscopy image of the Si(111)–(7×7) surface reconstruction. Two triangles representing the surface super cell where the different brightness is due to the periodic fault in top layer stacking. The six outer bright atoms in each triangle represent ad-atoms and the tree dimer ones represent rest atoms [43]

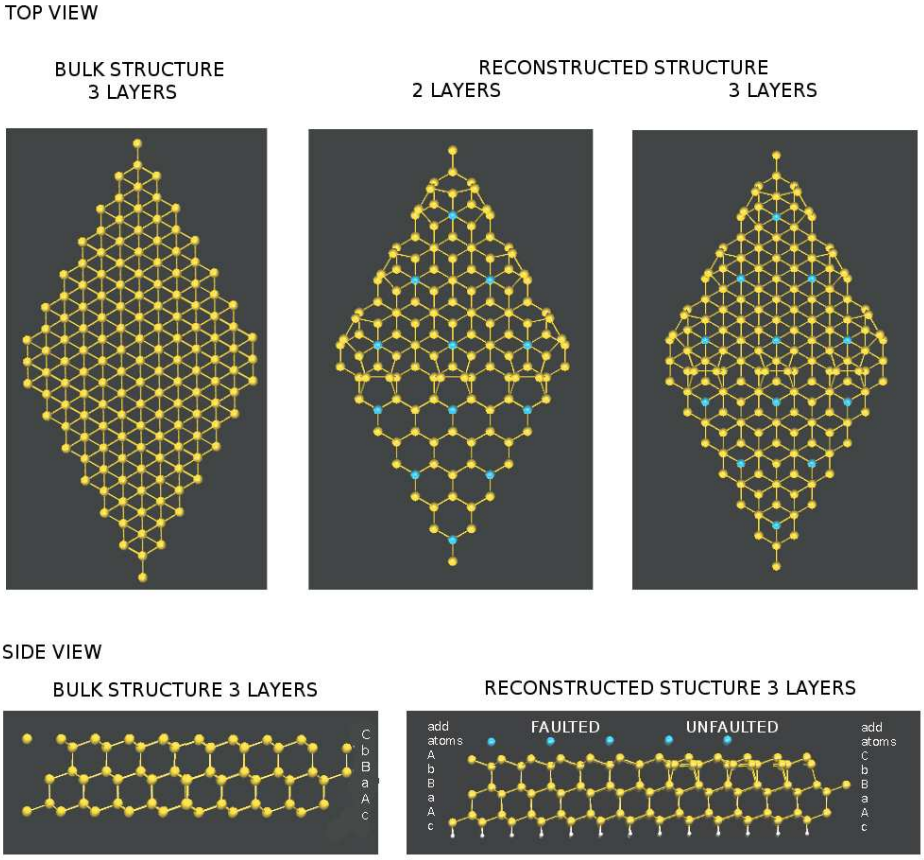

Figure 7.3: The top and side view of the (111) surface reconstruction with the side views presenting the detailed characteristic of layered arrangement and the nature of the stacking fault. The top layer of a faulted half of a supercell changes its stacking sequence from (bulk: ...AaBbCc) AaBbC to (bulk: ...AaBbCc) AaBbA.

7.3 Si(100) – c(4x2) surface reconstruction

The Si(100) surface is the most common facet of a silicon crystal. In a reconstructed surface it minimizes its energy by the formation of dimers from top layer atoms, so that the number of dangling bonds is reduced by 50%. The surface is composed of Si-Si dimer rows, while dimers in their energetic ground–state form a buckled c(4×2) structure (Fig 7.4). At room temperature, however, the surface involves asymmetric buckling vibrations of the dimers, in effect causing a flip-flop motion between opposite buckling configurations. The flip-flop motion cannot be seen directly in an STM due to the low time-resolution, although its result can be inferred from averaged surface images of flat dimers, appearing to posses (2×1) symmetry [44]. The reconstructed surface utilized in the clean surface and molecular adsorbtion

calulations was also generated using written by python script. The process is however much simpler in comparison to a Si(111)–(7×7) reconstruction, since it involves only dimerization, buckling and bulk surface hydrogenation. The obtained initial atomic arrangements were relaxed by VASP in two stages, first fixing all atoms except hydrogen passivating the bottom layer, and then keeping hydrogen together with the two bottom layers fixed, while all other layers underwent relaxation. The kpoint sampling was limited to Γ point and energy cut off was set to 350 eV.

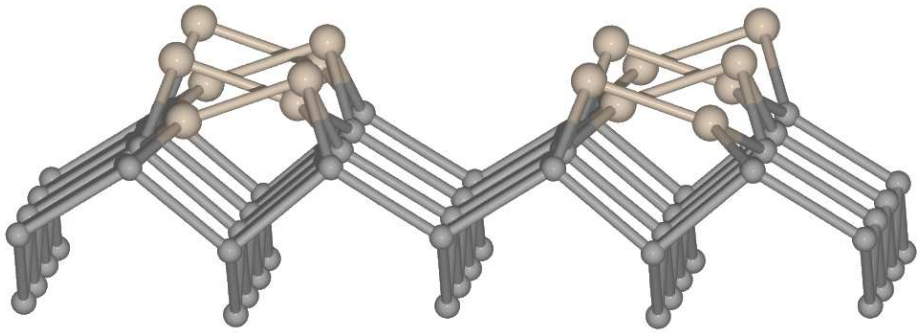

Figure 7.4: Si(100)–c(4×2) reconstruction. Beige atoms represent the top reconstructed layer of silicon atoms, forming rows of dimers buckled in opposite directions. The left row mirrors the right row forming a *c*–type reconstruction. Grey atoms represent second, third and fourth silicon layer.

The surface buckling is not only characteristic of Si(100) it has also been observed on Ge(100), therefore some of the results highlighted in the following are transferable between these system. At low temperature the buckling is static and can be easily observed in experiments. It takes the most energetically favourable symmetry forming a $c(4 \times 2)$ super-cell [45]. This observation has been also confirmed in theoretical studies of other different possible phases [46]. During the dimerization the charge is transferred from the lower to the higher Si atom within the dimer; this asymmetry in local charge is also causing an asymmetry of the atomic arrangement. As shown in the Fig. 7.6, the local density of states (LDOS) peak for the up atom (pink line in the figure) in the dimer is in the valence band, while for the down atom (blue line in the figure) it is in the conduction band. On the same plot we also included the LDOS of atoms in a flat dimer configuration (green), obtained from a flat dimer unit cell calculation, which shows a transition between the up and down results with the LDOS peak shifted closer to the Fermi level. The dimer up and down buckling also affects the second atomic layer, where the atoms change their position due to the geometry of the dimers. The atoms under the up atoms are pulled up, while atoms under

the down atom are lowered as seen in Fig. 7.5.

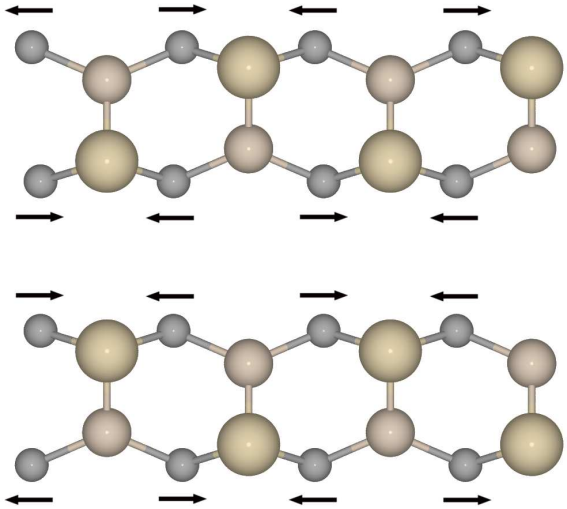

Figure 7.5: The illustration of the buckling influence on the the top layer of Si(100)–(4x2) reconstruction, the beige atoms represent the dimer atoms with brighter ones being buckled up and darker buckled down. The grey atoms represent first layer beneath the dimers, while the arrows indicate the necessery shift of these atoms to accomodate the buckling.

Employing an Ising model Fu *at el.* have estimated that at room temperature the dimers have sufficient energy to oscillate between the opposite buckling with a frequency of about $3 \times 10^6 Hz$ [46].

7.3.1 Pinning

Although the fast oscillations do not allow one to observe this characteristic $c(4\times2)$ zigzag structure in room temperature STM images, this is not always the case when dealing with defects or adsorbates. On many occasions, it has been observed that dimer oscillation can be affected and buckling can become apparent even at room temperature. Depending on the temperature and the strength of pinning, the observed effects can have local (just a few dimers) or much broader character responsible for creating domains of in– or anti– phases (see Fig. 7.7). Controlling and understanding the different Si(100) phases is of great significance due to its potential to be utilized in applications such as molecular electronics, quantum computing or quantum optics [47]. Even though the low temperature STM has repeatedly proven that Si(100)–c(4×2) is a factual ground state phase [45], the phase can be affected by a specific molecular adsorption. In the literature this process is referred to as dimer pinning when the buckling oscillation is limited in

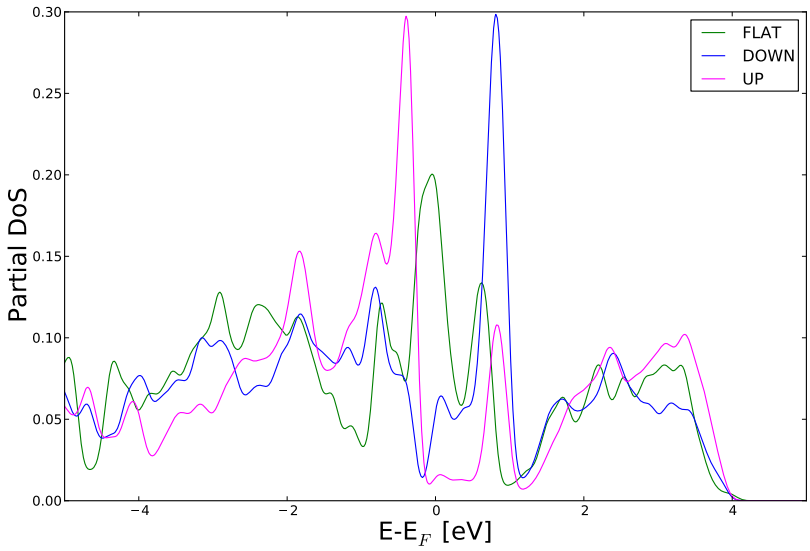

Figure 7.6: Si(100)–c(4x2) reconstruction, a comparison between a localized density of states for Si atoms buckled up or down (Gaussian broadening with a width of 0.2 eV).

a specific direction. So far, it has been shown that the restricted buckling can contribute to changed geometry/reactivity induction of surface electric dipoles and double row in– or anti– phase relation [47].

Previous work has shown that when the symmetry of the surface is broken by a defect or a step edge a regionally fixed buckling may occur [45, 48]. Hossain *at el.* present no cross–dimer row correlation, thus showing no evidence of a strong interaction between the rows. The observation regards molecular adsorption in which the two neighbouring molecules create pinning of the dimer row. The distance and the position of molecules affect the result of in phase or out of phase pinning. This effect is observed at the temperature of 300K, and the molecule used is $(CH_3)_2NCH_2CH_2N(CH_3)_2$ $(N,N,N',N'--tetramethylethylenediamine)$ (TMEDA) results in visible pinning ranging 12 dimmers away from adsorption site. The first introduced model of induced dimer pinning was based on an Ising-type model and has been mostly concerned with dimer–dimer interaction rather than molecule–dimer interactions. This has been recently expanded to molecules and will be further discussed in the following section [49, 50]. The relationship between the surface and the adsorbate has been proven to be much more complicated than initially assumed when not only the geometry but also the character of the individual bonds or polar interactions play a significant role. Smith *et al.* have shown that full knowledge of pinning could help to determine the

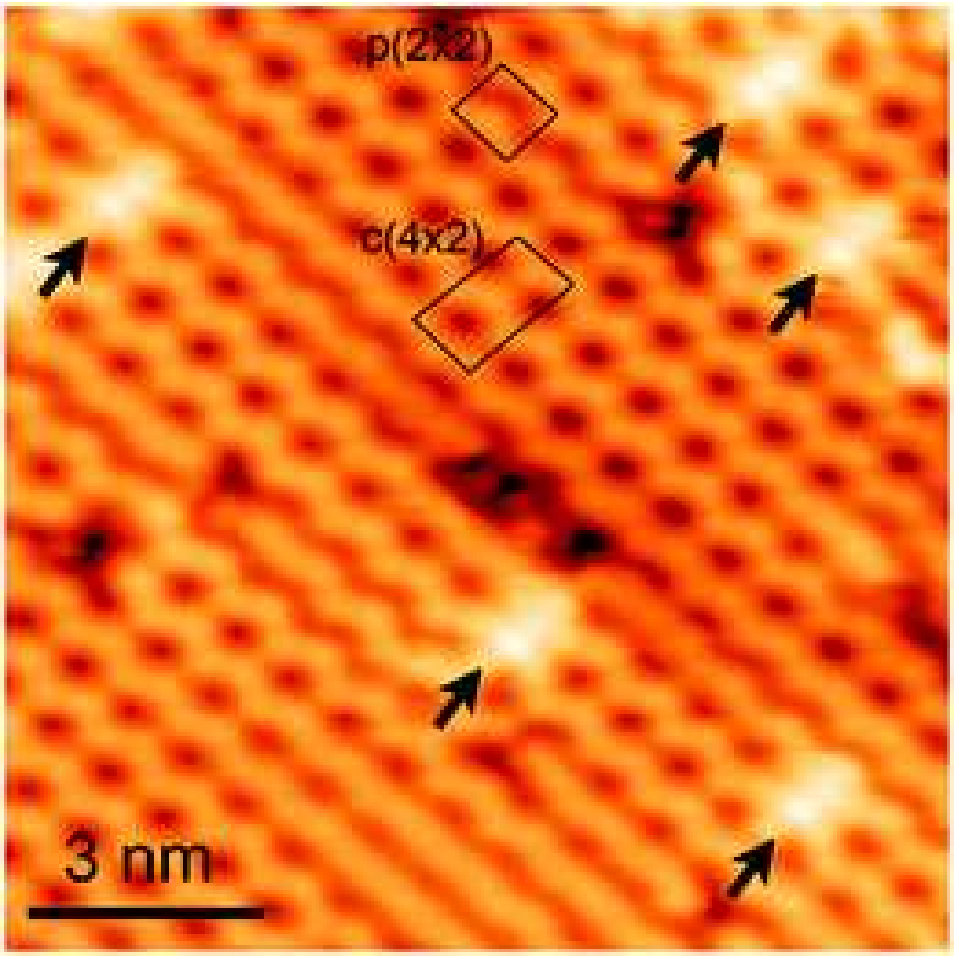

Figure 7.7: STM images taken by Hossain *et al.* showing the adsorptions of small amounts of TMEDA molecules at 65K, bias $-2V$ and tunnelling current $0.2nA$. The pinning caused by the molecule is responsible for creation of two phases: c(4x2) and p(2x2). [47]

molecular adsorption of acetylalehyde and acetone, in which a clear distinction could be derived on the basis of buckling signatures in between the (2+2) cycloaddition or enolate mediated geometries [50]. The approach based on the Isling model has been shown to be a powerful tool. This method could be used for different molecules and is expected to be applicable also on other surfaces exhibiting buckling, such as Ge(100), allowing the determination of the pinning strength and its directionality.

7.3.2 Defects

The clean Si (100) surface has several types of common imperfections such as step and point defects, all of which could influence surface properties or locally present processes. Due to the enormous importance of Si in current

industry, the issues related to the crystal purity and structural perfection are of wide interest. Despite detrimental properties of defects in some application, they have been shown to be the active site for both bulk and surface processes and can be used as catalytic centres, guides or markers in a self–assembly process. A proper understanding of existing impurities and defects is essential for applications where impurities are an integral element of the final material/device.

In the case of Si(100), point defects have been categorized into three types: A, B and C. The A and B types represent single and double dimer vacancies [51, 52]. The origin of the C type defect was initially ambiguous, there were a few different models proposed such as vacancies [53, 54], surface or subsurface foreign atoms [55, 56] and water adsorption [57]. In the past decade a general conclusion has been reached and the C defect has been identified as a reaction site for a water molecule. This will be further discussed in more detail in Section 8.1.

In order to further investigate the buckling phenomena a series of different studies were performed investigating the structural and energetic characterization of the system.

The systems of choice are dissociated water and two of its further transition states observed by both Sobotik and Warschkow *at. el.* [58, 59] which is particularly interesting due to the presence of strong pinning effects. In addition to these studies we have performed an electronic structure analysis to investigate the origin of pinning. Most of the studies have been performed on the Si(100)–c(4×2) surface although occasionally a flat dimer surface Si(100)–(2×1) was used.

Chapter 8

Surface pinning and water adsorption.

8.1 Water adsorption on Si(100)

Due to the importance of wet oxidation processes for the creation of SiO_2 layers, studies of water adsorption on Si(100) have received considerable attention. Water has been both appreciated as a reactant and catalyst, which makes it a key element in oxidation schemes [35]. Moreover it is also widely recognized as a surface contaminant due to its high residual concentration in Ultra High Vacuum (UHV) setups, which makes it desireble to know its effect on surface properties or surface processes. Historically there have been some concerns whether the adsorption of water is dissociative, which today are resolved and proven to be the case. The earlier proposed option was the *on-dimer* (OD) configuration in which the molecule dissociates on two dangling bonds of the same dimer. The STM study of this configuration suggested that adsorbed water appears identical to features previously assigned to single dimer surface defects [62, 63]. The other proposed configuration was *inter-dimer* (ID) with a molecule dissociating on the nearby dangling bonds of in-line neighbouring dimers which is also known under the name of C-defect. Subsequent DFT calculations showed that both of these configurations are stable [64].

The water adsorption is accomplished in a two step process in which at first the whole molecule is adsorbed and then it undergoes dissociation to H and OH. The process of dissociation can be described by means of transition state theory in which the total transition rate can be represented as a sum of a quantum tunneling rate and a rate due to thermal fluctuations.

The motion of the dimer can be described by the same model without

the tunnelling effect.

According to one calculation of the transition barriers, the transition to either OD or ID configurations is almost identical [65]. The minimum energy path (MEP) was investigated with the Climbing Image Nudged Elastic Band method (CI–NEB with water physisorption above down and up buckled Si atom). It has been consistently shown the DOWN Si atom is mediating in adsorption, when the oxygen attacks on the higher Si atom within the dimer it causes the dimer switch followed by adsorption [66, 67] The MEP shows that the oxygen attack is effective from any position with respect to the Si dimer, confirming the experimentally observed high rates of reaction [67].

The sticking coefficient of water is constant until saturation, suggesting a mobile mechanism for reaction. Because of its high mobility and reactivity, water can be a significant problem when in just one hour under the partial pressure of $10^{-11} mbar$ of residual water it already creates a 2 % surface coverage.

However $0.24eV$ higher energetic stability of OD vs ID does not explain the five times higher probability of ID adsorption. From the kinetic perspective the reaction barrier is 0.02 eV lower for ID which is still quite small to explain the behaviour. It has been suggested that this inequality in principle could be accounted for by H atom tunnelling similarly to the one shown for NH_3 adsorption [68]

The subject of dimer oscillation has been analysed in the recent work by Yu, providing some inside on the impact that dimer oscillation may have on the water dissociation pathways into ID and OD configurations, and it has been demonstrated that this effect may even lead to population reversal. Yu also suggested that the dimer's dynamics should be considered in analysis of other polar molecules on a Si(100) surface [69].

Although we consider Yu's point as an important consideration, we do not agree with his interpretation of the presented data in which he attributes all of the observed features to only two distinct processes. In fact, and as shown in earlier work, water dissociation is usually much more complex than that [58, 59]. It has been specifically shown that the elevations of the surface temperatures allows a series of transformations to occur which lead to surface dimer oxidation $Si–O–Si$ or even hydrogenation of this dimer $H–Si–O–Si–H$, which has been observed experimentally [70].

8.1.1 Computational details

In calculations presented here a set of different unit cells have been used to compare the different possible pinning. Four unit cell cells were generated using writen by me python script as presented in Fig. 8.1. Each unit cell composes of eight layers of Si atoms saturated from the bottom with H atoms, the unit cell is extended to nine or ten dimer rows to provide at least three dimers on each side of the adsorbate. The length of each is created in such a way as to preserve the buckling at the periodic boundary thus avoiding any unnatural effects which could occur otherwise. Due to a significant number of atoms the unit cell includes only a single dimer row. Ions were relaxed using PAW-PBE as implemented in VASP until the residual forces were less than 0.02 eV/Å. The H atom layer and two bottom layers of Si atoms fixed in their bulk positions. The k point sampling was performed with 1 x 3 x 1 mesh and the energy cut of was set to 350 eV.

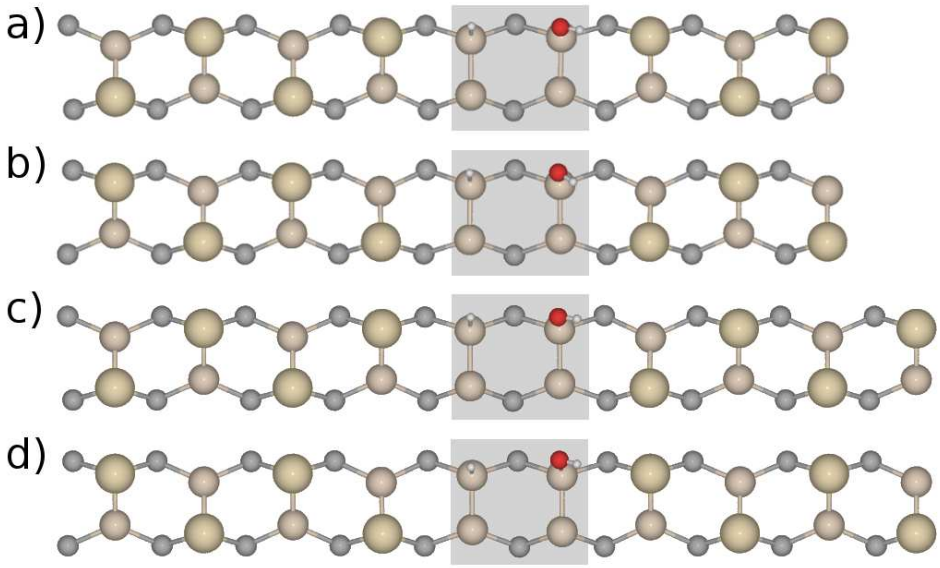

Figure 8.1: Four different buckling configurations for the OH, H inter–dimer adsorption of dissociated water molecule on Si(100)–(2×1) surface; in a) and b) the molecule breaks the buckling phase, while in c) and d) the phase is preserved. The unit cells are always created to preserve phase upon the periodic transformation. The beige atoms represent the dimer atoms with brighter ones being buckled up and darker buckled down, the black atoms represent first layer beneath the dimers.

In order to account for the different unit cells while comparing total energies, the contribution to the total energy from additional atoms was calculated. The approximated energy was obtained as a difference of total

OH and *H*	
Energy	meV
E_1 (a) in Figure 8.1	0
E_2 (b) in Figure 8.1	45
E_3 (c) in Figure 8.1	4
E_4 (d) in Figure 8.1	14

Table 8.1: Results of calculation for adsorption energies of dissociated water molecule on Si(100) - c(4×2) surface in comparison with other theoretical results.

energies from two clean surface calculations, eight and ten dimer divided by to to represent the energy difference per extra dimer, which was equal to 97.11 eV.

$$\Delta E = \frac{E_{10} - E_8}{2} \tag{8.1}$$

The unitcells with even number of dimers were chosen to account for the continuity of the buckling phase.

8.1.2 Results

From the obtained results presented in the Table 8.1 the most stable configuration predicted is E_1 (a) in Fig. 8.1), this is in agreement with experiment. Furthermore the switch of pining from a) to c) is 0.01 eV more likely than a) to d) which means that the pinning on the *H* side is expected to be stronger than on the *OH* side, this is also observed in experiments (see Fig. 8.2). Our results confirm that the phase of buckling most preferably gets broken and that the pinning strength on both sides is asymmetric.

We have investigated the impact of the adsorbate on the change of local density of states (LDOS) in the vicinity of the adsorbate. By comparing the atom projected DOS we have found that the changes are very minor and are restricted to the dimer directly involved in adsorption and the atoms below that dimer. The neighbouring dimer atoms DOS are unaffected, this conclusion applies to all the adsorptions that follow in this thesis unless stated otherwise. The exceptions to this are not resulting from molecule–surface charge transfer but from the dipole interactions between the molecule and a Si dangling bond, such as the one discussed below.

As presented for the *H* side buckling in Fig. 8.3 there is no observable change in the density of states for C–defect adsorption (Fig. 8.1). From the comparison of peaks for UP (occupied states) and DOWN (unoccupied states) atoms it is evident that the overlap of the colour lines (neighbouring

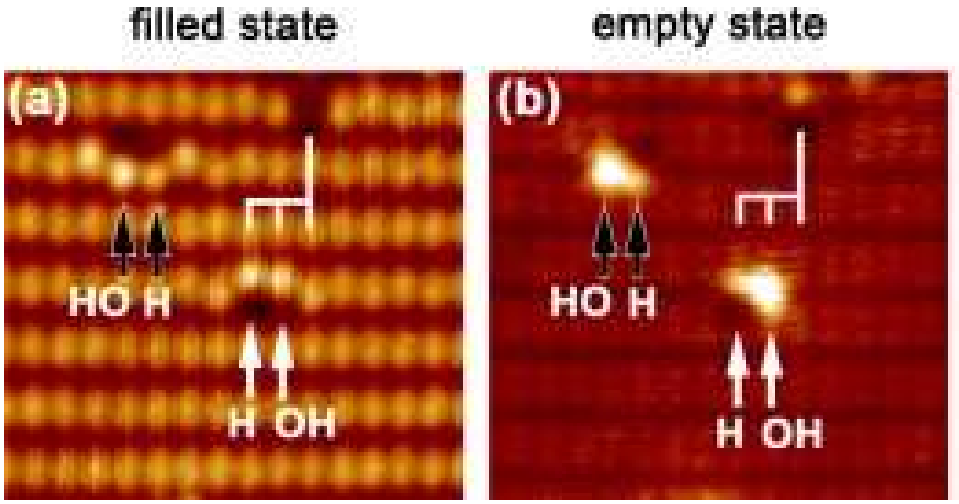

Figure 8.2: STM images taken by Warschkow *et al.* showing filled and empty states for $-2V$ and $2V$ respectively at current $0.3nA$ of water C–defect on Si(100) surface. [58]

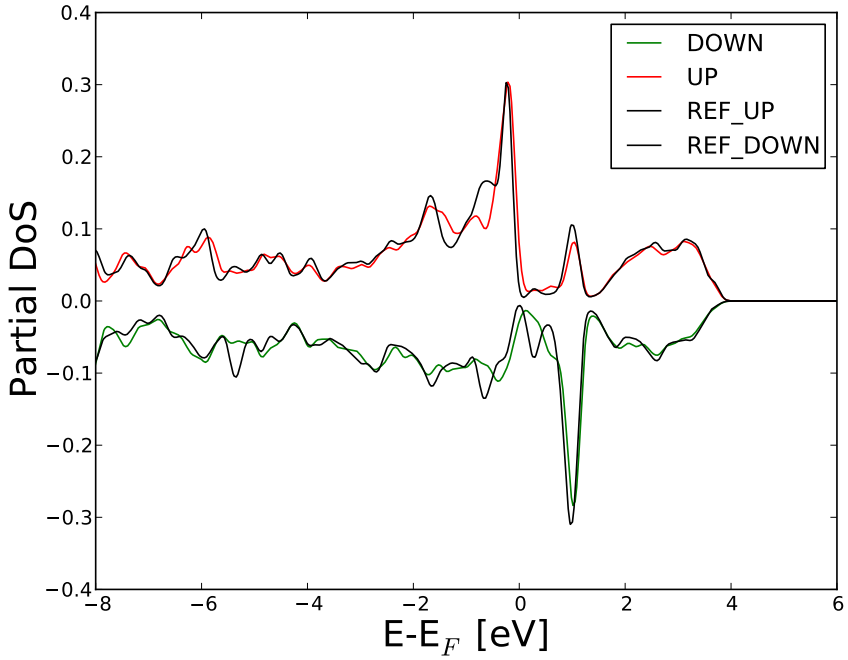

Figure 8.3: LDOS of UP and DOWN dimer Si atoms on Si(100) surface with C-defect on it. The considered atoms are neighbouring to a dimer with H adsorbate (see a) in Fig. 8.1) while REF_UP and REF_DOWN are a reference up and down atoms far away from the adsorbate. The up buckled atoms are on the positive axis while down are on the negative one.

dimer) and black plots (far away reference dimer) are almost identical. For the OH–side Fig. 8.4 however, a slight shift in the density is observed which

can be attributed to the dipole moment of the OH group. The OH dipole moment is known to be about 1.5 D. Then the potential in the vicinity of the dipole will be

$$V(\mathbf{R}) \approx \frac{1}{4\pi\varepsilon_0}\frac{q\mathbf{d}\cdot\hat{\mathbf{R}}}{R^2} \tag{8.2}$$

where R is a distance from the centre of the dipole moment, one can estimate that the potential at 4.0 Å will be 0.25 V if the direction of the dipole was exactly in the direction of measurement. In reality the electron cloud is disperse and the direction varies therefore this value represents only the higher limit. The shift measured in between the UP peak and the REF_UP peak is about 0.21 V which is in good agreement with the approximated value. Furthermore the adsorbed O–H group pointing toward the dangling bond has been observed to induce buckling up, while the OH group pointing in the opposite direction induces buckling down [66].

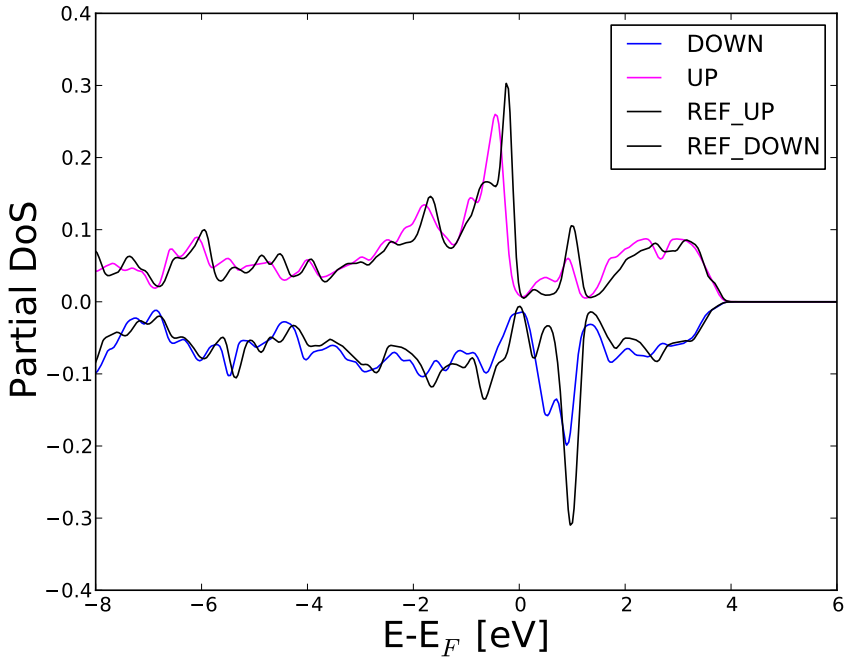

Figure 8.4: LDOS of UP and DOWN dimer Si atoms on Si(100) surface with C–defect on it. The considered atoms are neighbouring to a dimer with OH adsorbate (see a) in Fig. 8.1) while REF_UP and REF_DOWN are a reference up and down atoms far away from the adsorbate. The up buckled atoms are on the positive axis while down are on the negative one.

8.2 High coverage water on Si(100)

8.2.1 Introduction

As recently shown by Gallet and co-workers high coverage water adsorption offers a wide range of patterning. In the STM image presented by them (Fig. 8.5) a set of signatures can be distinguished for a different dimer dangling bond saturation. The possible combinations can be attributed to two H atoms per dimer, two OH groups, or one H and one OH attached to the dimer. Occasionally, individual dangling bonds are preserved [164].

In our observation as well in earlier studies it has been shown that OH groups have a tendency to orient themselves orthogonally to the dimer bond direction [165]. In this section we aim at investigating this behaviour in high coverage cases where many OH groups are able to interact with each other, with H atoms, and with isolated dangling bonds. We have performed structure relaxations and from the relaxed geometry simulated the STM images.

8.2.2 Computational details

We have recreated the features proposed in the experimental results in Fig. 8.5 and created a unit cell containing each of the above mentioned signatures. The cell used is composed of seven layers of Si atoms hydrogenated from the bottom, with two dimer rows, a total of eight Si dimers. The STM images were performed using Tersoff–Hamman approximation as implemented in bSKAN.

8.2.3 Results

During the ionic relaxation, a clear movement of the OH moieties is observed. Although this process is very slow and requires over a thousand ionic iterations. The general observation for the high coverage scenario is that OH groups preferentially align along the dimer rows if adjacent to another OH group. As seen in the structural illustration Fig. 8.6 the dipoles also interact on the dimer.

Analysing the experimental images of single dissociated water (Fig. 8.2) it is evident that it is possible to identify both the OH and H adsorption sites of the C–defect, due to the characteristic drop shape feature, and the asymmetric dimer pinning. The problem is that the STM feature does not arise from the adsorbate but from an empty dangling bond on the adsorbed dimer. When investigating full adsorption, a majority of dangling bonds are

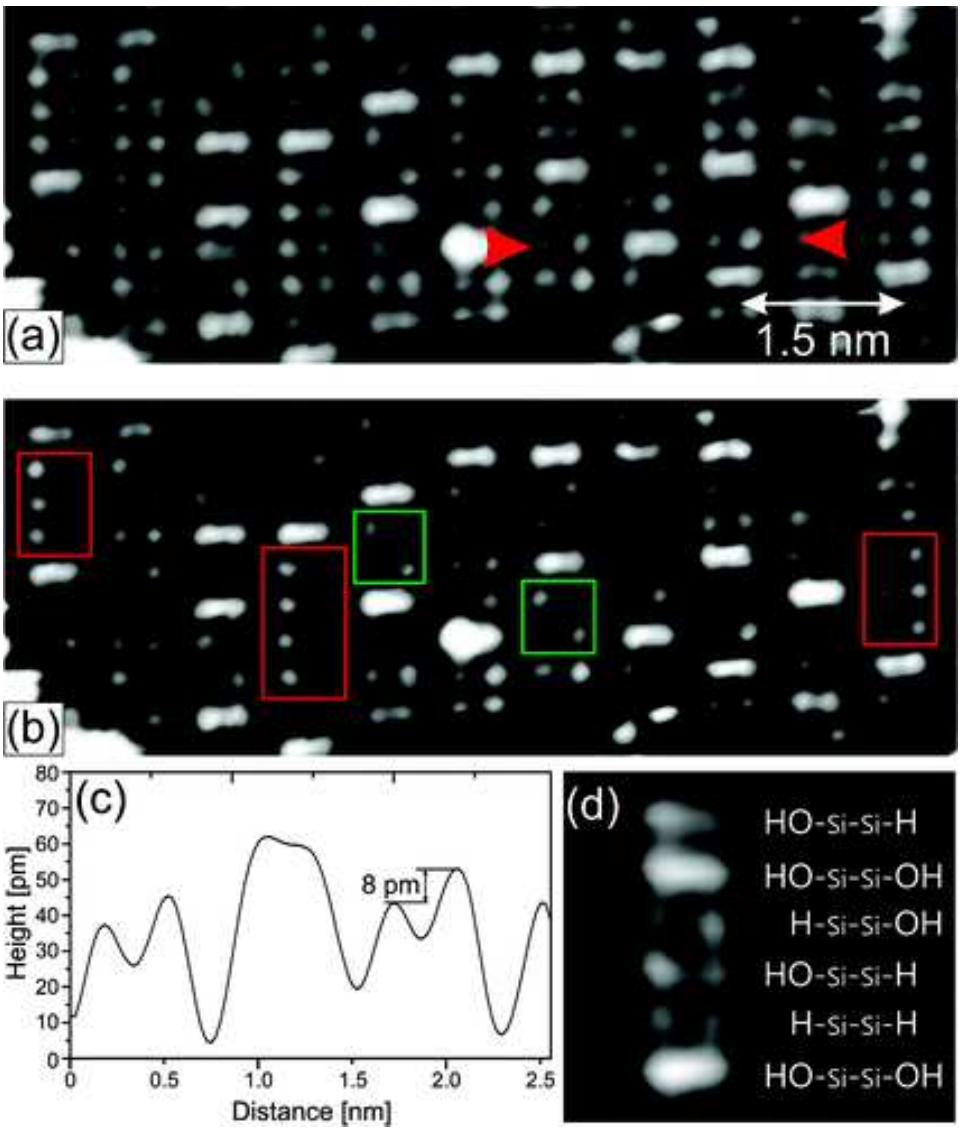

Figure 8.5: STM images of high coverage of water on Si(100)–2×1 by Gallet *et al.* (a) Image (8.5 nm × 4.0 nm) of water–saturated n doped surface scanned at bias voltage$V = -2.3V$ and $I = 0.57nA$, showing occupied states. (b) Same as (a) but with enhanced contrast to show the alignment (red rectangles) and zigzag (green rectangles) patterns made of *H–Si–Si–OH* units. (c) Line profile through the location marked by the red arrows in (a), encompassing from left to right, *H–Si–Si–OH*, *HO–Si–Si–H*, and *H–Si–Si–OH* units. (d) *H* and *OH* distribution along a dimer row, showing the coexistence of *H–Si–Si–OH*, *H–Si–Si–H* and *HO–Si–Si–OH* units [164]

saturated, therefore neither the drop feature nor the pinning are visible.

So far no account of the *OH* direction has been discussed in the experimental investigation and the existing high coverage STM images. In this thesis as well as in earlier works it has been observed that the *O–H* bond

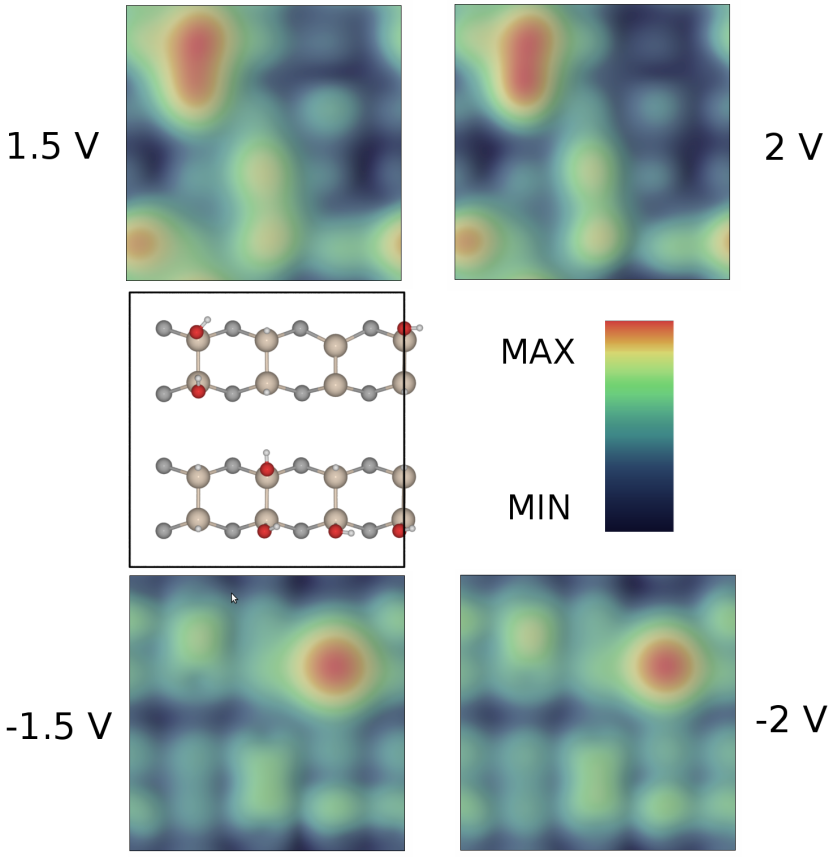

Figure 8.6: The relaxed unitcell of high coverage water adsorption on Si(100)-(2×1) surface with simulated STM images for the bias voltage of V = −1.5, −2, 1.5 and 2.0 for LDOS = 1 $\times 10^7$states/(eVm^3).

is rotated along the surface [166]. Here, we want to further investigate the effect. As visible in Fig. 8.5 the feature variation is quite significant where the brightness of the OH and H features varies considerably. From the presented STM images no OH direction can be clearly determined. This lack of definition regarding OH orientation may be caused by the thermal fluctuation and clarification of this subject using a low temperature STM would be required. When investigating the simulated STM images Fig. 8.6 a similar observation can be made. In both positive and negative bias images the feature representing H atoms is considerably lower while the OH group's signature is varied. For negative biases the height of the features are similar for all OH singularly occupied dimers while the two doubly occupied dimer offer distinct shape, one is symmetrical while the other is not. The variation between the OH signature is even more prominent at positive voltages where not just a shape but the height varies considerably.

Chapter 9

Single organic molecules on silicon surfaces

9.1 Molecules on surfaces

Before investigating surface chemistry let us first outline the basis of what is responsible for the molecular reactivity in the first place. How can we predict if the ambient molecule will, or will not attach to the surface. The sticking probability of Si atoms arriving at the clean Si surface at thermal speed is practically 1, but this does not have to be the case for other atoms or molecules and can also dramatically change upon surface reconstruction.

In general, the ability of the surface to accept an adsorbate is controlled by the local electronic structure, the geometry of the surface and theirs vibrations of which the first two are a subject of a following chapter. In the first approximation, the key factors are: the electronegativity difference between the reaction species and the availability of electrons for the charge transfer caused by this difference. For example the highly electronegative oxygen will prefer a Si atom with occupied dangling orbital close to the Fermi energy E_f, so that the O atom can acquire an electron from Si with maximum energy gain.

The character of the reaction between the surface and the adsorbate is likely to change in the course of the adsorption. There is a dependence of the adsorption rate on the exposure time due to the varying coverage, it is well known that some adsorbate species may stick better when agglomerations in the form of islands are already present on the surface. The same applies for different adsorption rates resulting from adsorption on special sites such as defects, dislocations or ridges which are often the first to be occupied. In the case of island formation the adsorption rate is dependent on the amount

of island already present on the surface [35].

In general, the adsorption of molecular species proceeds though several stages. The free molecule may become physisorbed, chemisorbed, or dissociatively chemisorbed on the surface. These states can most of the time be separated by energy barriers which further permits the determination of their transition rates, sticking probabilities and reaction pathways.

Physisorption is the weakest form of adsorption. It is characterized by lack of true chemical bond instead the molecule bonds to a substrate thought the Van der Waals or Coulomb forces. Because the molecule makes no chemical bond with the surface it can often migrate efficiently over the surface. The analysis of molecular physisorption is an important field of surface science which is a driving force behind self assembled networks on metallic surfaces or molecular imprinting techniques when the physisorbed molecules template the later chemisorbed atomic pattern. Even at large distances a mutual attraction between the atom and the surface exists that arises from the interactions of polarizable solid with the dipole from the quantum mechanical fluctuation of the atomic charge distribution and vice versa.

In contrast to physisorption, a chemisorbed molecule does make a chemical bond. The molecule however retains its identity without breaking into separate pieces. For some molecules this adsorption state is not a final one and under the right conditions they further undergo dissociation into moieties such as H_2O described in sec 8.1 .

9.2 *1,2*–dibromoethane on Si(111)

In this work we aimed to provide some clarification and an explanation of the unusual behaviour observed experimentally in which the chemisorbed, physisorbed or mixed adsorptions were observed in the one per corner hole (OPCH) pattern, even so there has been another five empty adsorbtion sited (there is six adatoms per corner hole). The molecule involved was physisorbed *1,2*–dibromoethene which gave rise to the bromination of corner-hole (CH) Si atoms. The observed phenomena suggested some mechanisms responsible for the characteristic one per corner hole adsorption. The knowledge of the underlying atomic processes could be of great value for a better control in self–assembly and nano manufacturing process. Although adsorbate repulsion has been observed, so far it has been restricted to metallic surfaces only. On metallic surfaces the molecular repulsion can be referred to different processes. The presence of the weak repulsion with forces of around 5 meV at 10 Å distance can be attributed to the standing electron waves,

while stronger interactions can be attributed to electrostatic interaction between molecules that have acquired charge from the surface [71, 72, 73]. The other reason may be dipolar interactions of about 20 meV at 15 Å, in this case the strength of this interaction is doubled due to the image–dipole interaction [74]. In our situation we deal with a semiconductor surface and the distance between the opposite ad-atoms at the corner hole is 13.4 Å. In recent works it has been shown that the charge injection into the surface using the STM tip can result in hopping of chlorine atoms [75], or a non-local removal of chlorobenzene molecule [76]. Non local activation of a metastable adsorbtion of hydrogen on Si(100)–(2×1):H surface was also observed [77].

9.2.1 Experimental findings

As presented by McNab *et al.* in STM images [78], the physisorbed molecule preferentially attaches itself to one of the adatoms located by the corner hole Fig. 9.1. In general no more then a single molecule attaches to the same corner hole, but exceptional double adsorptions have been also observed. It is difficult to explain this behaviour from the perspective of the electrostatic repulsion of molecules adsorbed at the same corner hole. The repulsion would be expected to be quite weak due to the large diameter of a corner-hole, thus the observed phenomena would be more likely related to a surface mediated effect.

It is expected that the single adsorption creates a significant change in the corner hole environment making secondary adsorption highly unlikely. In coverage studies a threshold for the surface saturation has been observed at about 80 % for both the bromination and preceding it *1, 2*–dibromoethene physisorption further supporting the presence of significant repulsion. Additionally, the statistical analysis of the bromination provided evidence for the mobile precursor. Due to the mobility of the molecule it is expected that the minimum energy configuration is reached.

The experimental data show there was no site selectivity between adsorptions on ad-atoms of the faulted or unfaulted part of the Si surface. When physisorbed, *1, 2*–dibromoethene molecules undergo a thermally induced chemical reaction and brominate the nearby ad-atoms Fig. 9.2. In no case has any residual part of molecule been observed after the bromination of the surface. According to experimental results obtained by McNab and coworkers the bromination of a CH adatom is highly favoured over the middle adatoms. The ratio of reacted Br atoms occupying the corner-hole adatoms to those occuping the middle adatoms is around 13, making it relatively un-

likely. For this to happen a strong thermodynamic or kinetic preference is required. Here again as in molecular adsorption, no selectivity is observed between the faulted and unfaulted sites.

In experiment of a partially brominated surface exposed to the *1, 2*–dibromoethene, the OPCH pattern was still preserved. In the mixed dBrE and Br there was occasional double occupancy but 93.8 % was still singular.

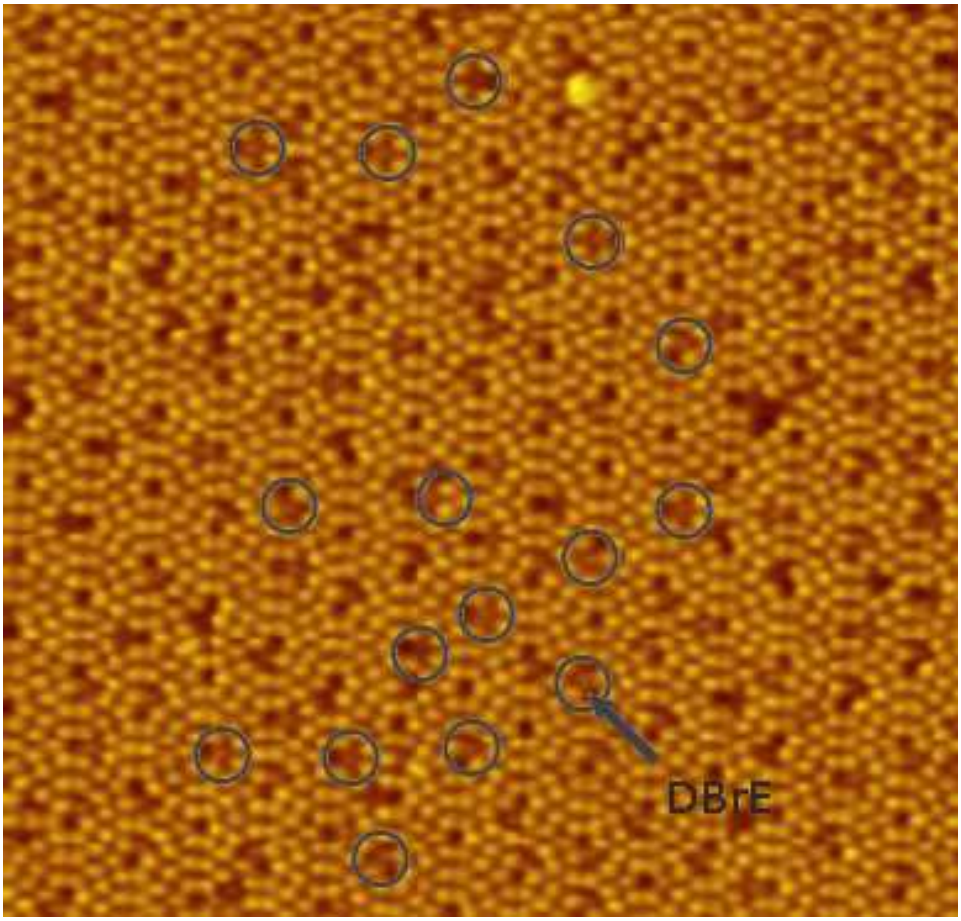

Figure 9.1: Scanning tuneling image of physisorbed dibromoethane molecules on Si(111)–(7×7). The image was taken at 110 K with a bias voltage of+2.5 V and a current of 0.2 nA [79].

9.2.2 Computational details

The calculations were performed using the Vienna Ab initio Simulation Package (VASP) [80, 32] with Generalized Gradient Approximation (GGA) and Perdue Burke Ernzerhof– Projector Augmented Wave (PBE–PAW) potentials. The energy cut off was set to 300 eV, the inter ionic forces were minimized until the reached value was smaller than 0.02 eV/Å with the k point sampling restricted to the gamma point due to large unitcell size.

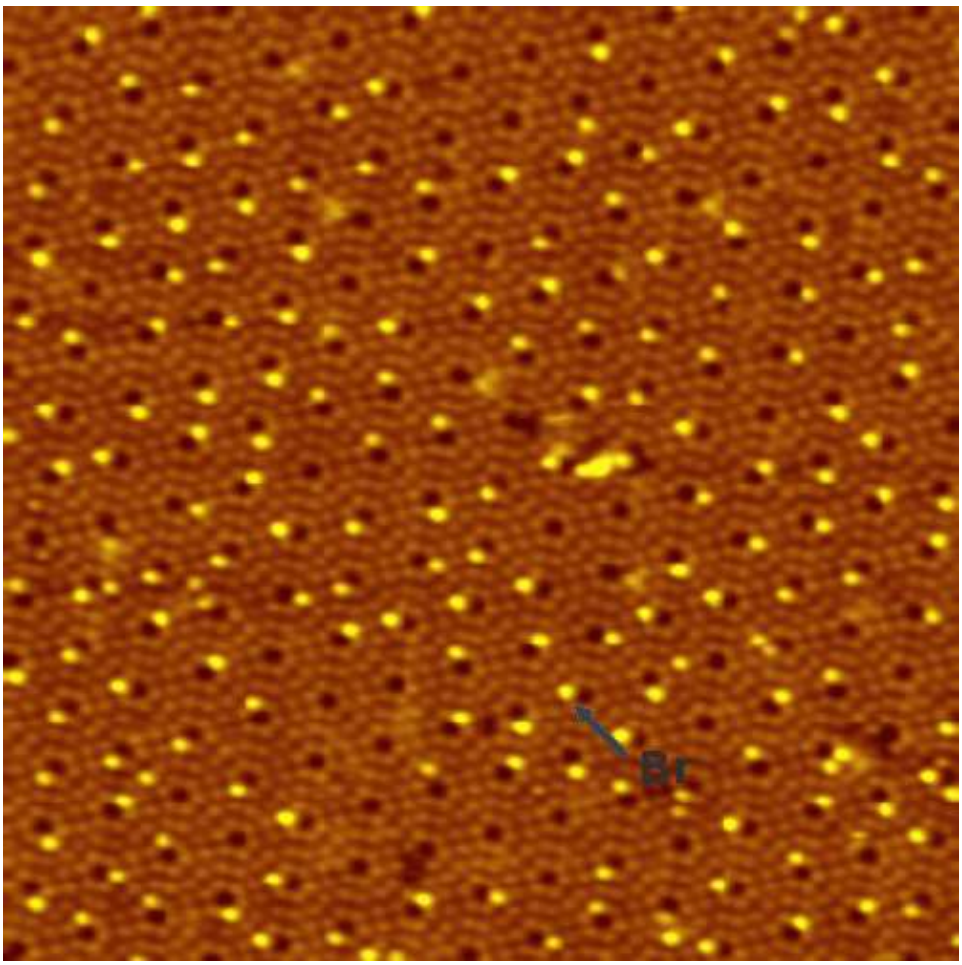

Figure 9.2: Scanning tuneling image of chemisorbed Br atoms on Si(111)–(7×7) reconstructed surface. The image was taken in 298 K with bias voltage +2.5 V and current 0.2 nA [79].

The generated unit cell Fig. 7.2 was prepared by at first fixing all the Si atoms and relaxing the H atoms then fixing the bottom two layers together with H atoms while the top layers were relaxed. The unit cell contains 49 H atoms and 298 Si atoms and has a size of $A_1 = (13.539, 23.449, 0.000)$, $A_2 = (-13.539, 23.449, 0.000)$ and $A_3 = (0.000, 0.000, 32.000)$ Å.

1,2– dibromoethane exists in two forms, as rotational isomers of *gauche* and *trans* type (Fig. 9.3) . In the gas phase their relative populations is in proportion of 1 to 9 respectively [81]. I present the structural analysis for both isomers in the Table 9.2.2.

Due to very low energy differences, both isomers are expected to be present on the surface with their population ratio possibly influenced by the interactions with the surface. The calculated gas-phase energy difference is 98 meV making the *trans* isomer more stable due to the lesser strain. In the

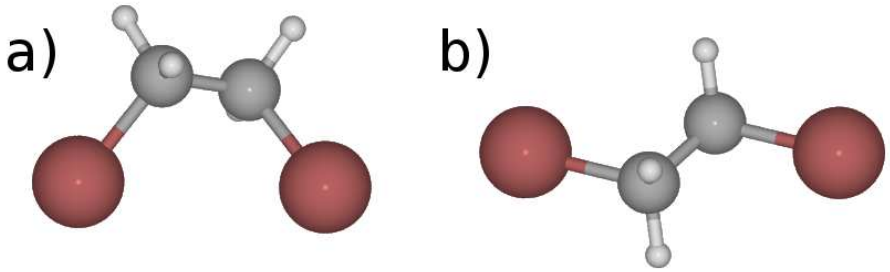

Figure 9.3: Two rotational isomers a) *gauche–1,2*–dibromoethane b) *trans–1,2*–dibromoethane.

	trans	*gauge*
angles	(°)	(°)
Br–C–C	108.8	113.2
H–C–H	110.3	109.8
bond length	Å	Å
B–C	1.97	1.97
C–C	1.51	1.51
C–H	1.1	1.11

Table 9.1: The structural characterization of two rotational isomers a) *gauche–1,2*–dibromoethane b) *trans–1,2*–dibromoethane.

adsorption configurations the relative stability is expected to change due to the interaction with the surface and the repulsive vs attractive interaction for hydrogen and bromine atoms.

The most prominent feature of the isosurface of the potential landscape are adatoms, while the lower features represent rest atoms. The corner hole atoms create an indent in which the height difference between the adatom and the corner hole atom is around 4 Å.

9.2.3 Simulated configurations

In my analysis I have considered a series of physisorption configurations which are presented in Fig 9.4 – 9.9. From the experimental images it is visible that the profile of the occupied corner holes is symmetrical in relation to one of six radial axes (axis connecting CH central atom and CH adatom) thus the adsorbates need to be positioned in an appropriate way to match the image symmetry. Under close inspection all the observed features are characterized by a dark spot in the place of a CH–adatom, one can also

	d_1 Å	d_2 Å	E_a meV
trans– CH adatom and rest-atom, (Fig. 9.4)	3.89	4.00	66
gauche– CH adatom and rest-atom, (Fig. 9.5)	3.14	3.34	70
gauche– CH adatom CH interior, (Fig. 9.6)	3.37	3.75	-28
gauche– CH interior, (Fig. 9.7)	3.29	3.61	94
trans– two mid adatoms, (Fig. 9.8)	3.37	3.54	122
trans– CH interior wide, (Fig. 9.9)	3.37	3.54	58

Table 9.2: The structural analysis of *1,2*–dibromoethane adsorbates on Si(111)–(7×7) together with the relative adsorption energies E_a. The distances d_1 and d_2 represent the separation of the each Br atom from a closest Si surface atom.

	d Å	E_a eV
Br faulted CH, (A at (Fig. 9.10)	2.27	2.67
Br faulted middle, (B at Fig. 9.10)	2.27	2.67
Br unfaulted CH, (C at Fig. 9.10)	2.28	2.62

Table 9.3: The structural analysis for Br adsorption on Si(111)–(7×7): Br–Si bond length d and relative adsorption energies E_a.

distinguish a slight variation in that some adsorption presents a very darker feature and slightly apart from the neighbouring CH–adatoms, while others have an additional dim spot still present at the place of CH–adatom. It is unclear whether this is due to the experimental imprecision or is in fact a representation of different configurations.

In order to elucidate possible configurations a series of different geometries were tested. The molecular adsorption energies were calculated in reference to the energy of the *trans* molecule 10 Å above the surface (middle of the unitcell's vacuum region), these are shown in Table 9.2. The same methodology also applies for the calculation of adsorption energy of the Br atom (Table 9.2.3). Most of the adsorbed molecules were positioned in such a way as to correlate with the experimental STM image, ie, the molecules are placed so as to reduce the density of states available to the STM tip above the adatom and produce the symmetrical image with respect to the radial axis. Other configurations were also tested as benchmark studies.

Four of these configurations were considered, some *trans* while others were *gauche*. The results of our studies are presented in the Table. 9.2.

The first series of geometries are positioned on the radial axis, with the first two configurations a *trans* and a *gauche* molecule positioned above corner-hole add atoms and directed outward Fig. 9.4 and Fig. 9.5. The adsorption energies are similar for both *trans* and *gauche* configurations at 66 and 70 meV respectively. It is known that the physisorbed molecule has a limited impact on the electronic structure of the surface. Therefore it is reasonable to consider a scenario, in which geometrical restrictions alone prevent secondary CH adsorption. For that reason we investigated two geometries positioned to the inside of the corner-hole Fig. 9.6, Fig. 9.7. In this case the CH adatoms interior turned out not to be stable while the adsorption energy of the molecule within the corner hole is 90 meV. Additionally two other conceptually possible configurations were tested, from which one was adsorbed between mid-adatoms Fig. 9.8 and one was adsorbed in the corner hole, perpendicular to the symmetry axis Fig. 9.9 Here, surprisingly, the first turned out to be the most stable configuration with 122 meV, while the other was less stable at 58 meV. On the basis of the obtained results, one can conclude that there is a large variation of possible physiorbed geometries, with very similar energetics. The most stable geometry, however, contradicts experimental observations, in which CH adsorption is more stable then mid adatoms adsorption.

The obtained results therefore are unable to unambiguously confirm the preferable configuration in the experiments. In conclusion, standard DFT methodology in which van der Waals forces are not included turns out not to be accurate enough in examination of *1, 2*–dibromethene physisorption on Si(111)–(7×7) surface. For all physisorptions the distance of the Br atom to the nearest surface atoms is between 3.3 and 4.0 Å as presented in the Table 9.2.

Additionally bromine chemisorption was also tested (Table. 9.2.3) and it shows that energetics are independent of the location of the adatom, whether it is a mid or CH adatom. The comparison between faulted and unfaulted half shows a difference of 0.05 eV, showing there is no significant selectivity between faulted or unfaulted halfs.

9.2.4 Conclusions

In summary the results presented here show that no single unambiguous geometry could be found from the perspective of standard DFT calculations. The stable configurations obtained are in agreement with the experimental profiles in two cases: the CH adatom and rest atoms configurations, for both

trans and *gauche* molecule. It seems also possible that the central CH atom is involved in the adsorption, which supports a geometrical hindrance scenario due to hole saturation. As for bromine adsorption, no preference between the mid and CH atom is observed supporting the thesis that the selective bromination is an effect of CH selective *1, 2*–dibromoethene physisorption. Due to the computational expense of these calculations and a presumed need for thicker unit cells the investigation was terminated at this point. Subsequently, increased computing power coming to bear on a much larger cell was able to pin down the energetics to subtle changes in the subsurface arrangement which fully accounted for the effect. This work was published only recently by M. Ebrahimi et al. [82].

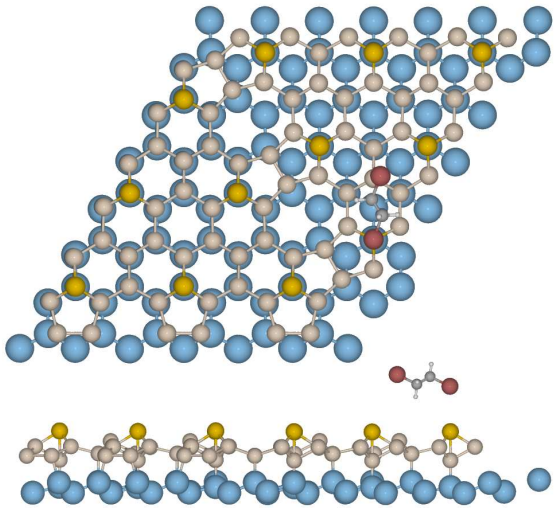

Figure 9.4: Top and side view of simulated physisorbed *trans–1,2–* dibromoethane above corner-hole adatom and neighbouring central corner-hole atom. .

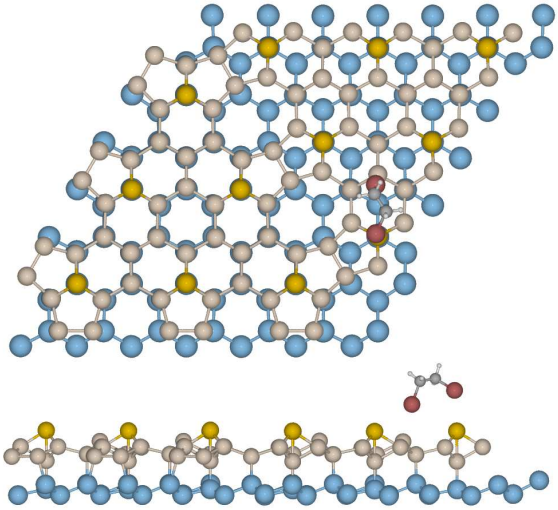

Figure 9.5: Top and side view of simulated physisorbed *gauche–1,2–*dibromoethane between corner-hole ad–atom and rest atom.

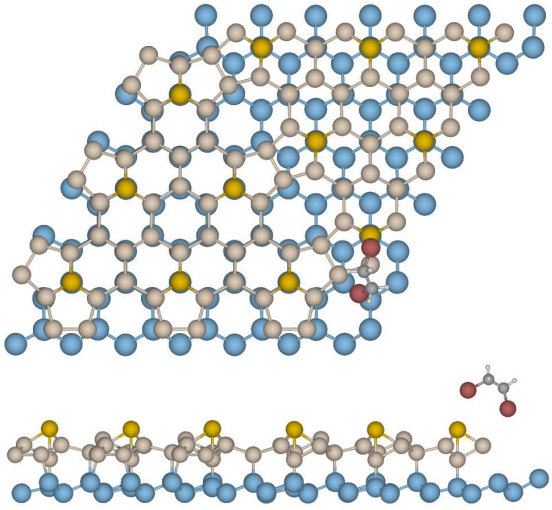

Figure 9.6: Top and side view of simulated physisorbed *gauche–1,2–*dibromoethane between corner-hole adatom and neighbouring interior corner-hole atom

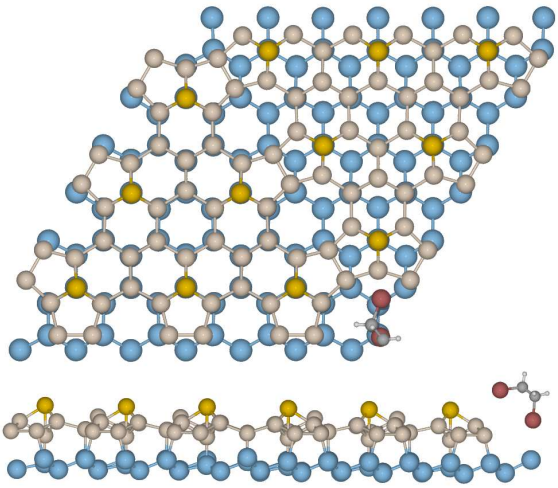

Figure 9.7: Top and side view of simulated physisorbed *gauche–1,2–*dibromoethane between corner-hole adatom and neighbouring central corner-hole atom.

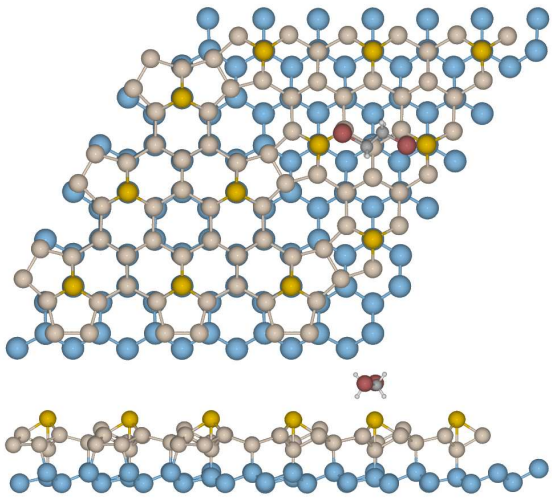

Figure 9.8: Top and side view of simulated physisorbed *trans–1,2–*dibromoethane between two mid-adatoms.

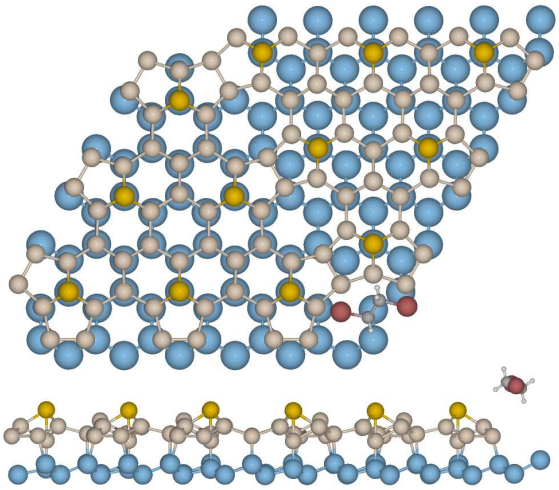

Figure 9.9: Top and side view of simulated physisorbed *trans–1,2–* dibromoethane between corner-hole atoms.

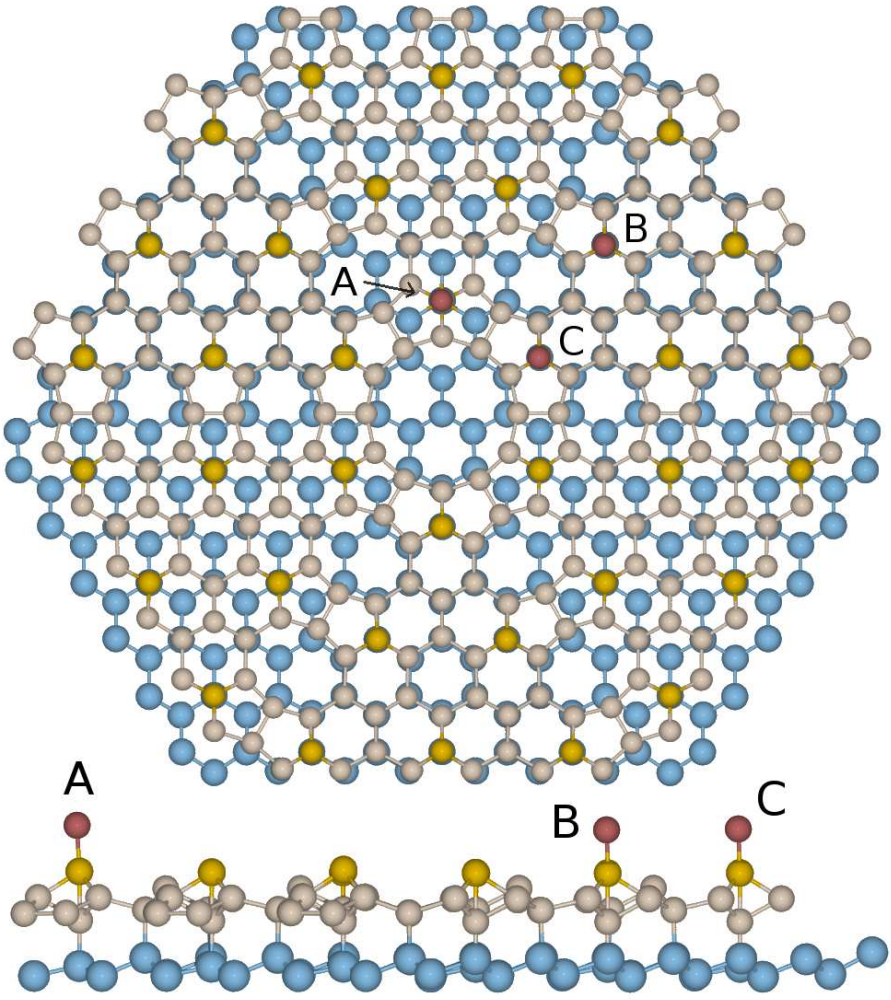

Figure 9.10: Top and side view of the three simulated bromine adsorptions: a) faulted corner-hole, b) unfaulted corner-hole c) unfaulted mid-adatom.

9.3 Ethylene on Si(100)

This section is concerned with thermal and electron stimulated migration of ethylene molecules. Adsorbate migration is a fundamental step in many surface phenomena, including self-assembly, material growth, phase separation and heterogeneous catalysis. Migration has been interpreted previously in the work of other laboratories as diffusion via sequential random hopping [83]. Real-space and even real-time observations of surface diffusion have been achieved using scanning tunnelling microscopy (STM) [84, 86, 87, 88] and ultra–fast laser spectroscopy [88, 89, 90]. In all these cases of diffusion, the direction of motion is random, and it is also short-range (5 Å), even on smooth metal surfaces [84, 86, 87, 88, 89, 90, 91, 92, 93].

In other studies recoil away from surfaces has been studied under the name of DIET (desorption induced by electronic transitions) [94]. These studies have provided valuable insights into the dynamics of surface diffusion due to thermal, electronic, or optical processes. Recoil towards surfaces is implied by the frequent observation in recent studies of electron-induced surface reactions [95]. Here, however, a directed long-range recoil in the plane of the surface is analysed, which is a genuinely novel phenomenon. The novelty resides not only in the long-range in-plane recoil, but also in the observation of reactions at a substantial distance from the originating events. This contrasts with frequent observations, in previous work, of ¨localized¨ chemical reactions [96, 97, 98]. The difference arises from the fact that in the present instance the exothermic process at first yields a mobile physisorbed species, which only later reacts, whereas in the case of a localized reaction a chemical bond forms immediately adjacent to the reagent molecule.

9.3.1 Experimental observations

Chemisorption of ethylene on Si(100) has been the subject of extensive experimental studies [98, 100, 101, 102, 103], while theoretical simulations supporting the evidence have been obtained [104, 105]. It has been shown that ethylene attaches to the surface by opening its π–bond and forming two C–Si σ–bonds. There are two observed configurations, one where the molecule is adsorbed between two dimers, the more common one, where it adsorbs directly on top of a single dimer, which is about 90 % of the total ethylene population adsorbed at room temperature which also agrees with this studies. This section's focus is to investigate the cause of long-distance molecular migrations induced by the tunneling current, for voltages below a threshold of -3 V. According to experimental STM data by K. R. Harikumar,

John C. Polanyi and Amir Zabet-Khosousi the molecule, at first adsorbed directly above the Si dimer, while stimulated migrates for distances as far as 200 Å. According to experimental results this is a one electron process, and the migration of the molecule has a directional preference, as shown in Figures 9.11 and 9.12.

The experimental data have also shown a significant temperature dependence, as presented in Fig. 9.12. The elevation of the temperature altered the outcome of electron-stimulated events. The desorption probability rises from 5 to 10 and 15 % from 25°C to 100° C, to 150° C, respectively. More importantly, the radial and angular distributions change significantly. Radially the exponential distance dependency decays while the angular distribution becomes sharper. At 25° C the angular distribution exhibits broad peaks at 0° and 63°. At 100° C the peaks moved toward larger angles and at 150° C the migration was dominant in the 90° direction, which is along the C–C bond of the initially adsorbed configuration.

Some of the experimental observations provided by Polanyi *et al.* were concerned with molecular migrations as a result of di–halogenation of the Si surface, the considered halogens were F, Cl, Br. This process took place at a temperature of 25° C. Upon dosing with di-haloethene two new surface features were observed. There have been no features that could be attributed to the intact adsorption of the di-halogen-ethylene (DXE) molecules. Furthermore, it has been recognized that the separation between the chemisorbed halogens and the migrated molecules similarly to the electrically stimulated ethylene molecule is up to 80 Å distant from the nearest halogen pairs.

The work done here is focused on the analysis of the excited states localized in the bond between the molecule and the surface, for the energies above the threshold of -3 V. The investigated scenario for the observed phenomenon was the possibility of a resonance of the tunnelling electron with the anti bonding state causing the Si–C bonds to break, while also inducing a torque on the molecule, causing its rotational excitation and thus far migration. The observed long range migration often even surmounts surface defects, other chemisorbed species or elevated terraces.

The observation that recoiling ethylene migrates over distances as great as 200 Å surmounting steps and exhibits directional preference suggests that the molecule moves ballistically rather than diffusively. Diffusive motion involves sequential short range hopping in random directions, scattering the absorbates from its initial recoil direction. Additionally, on the Si(100) surface one would expect the preferred direction to be along the dimer row due to the lower diffusion barrier. This however does not correlate well with

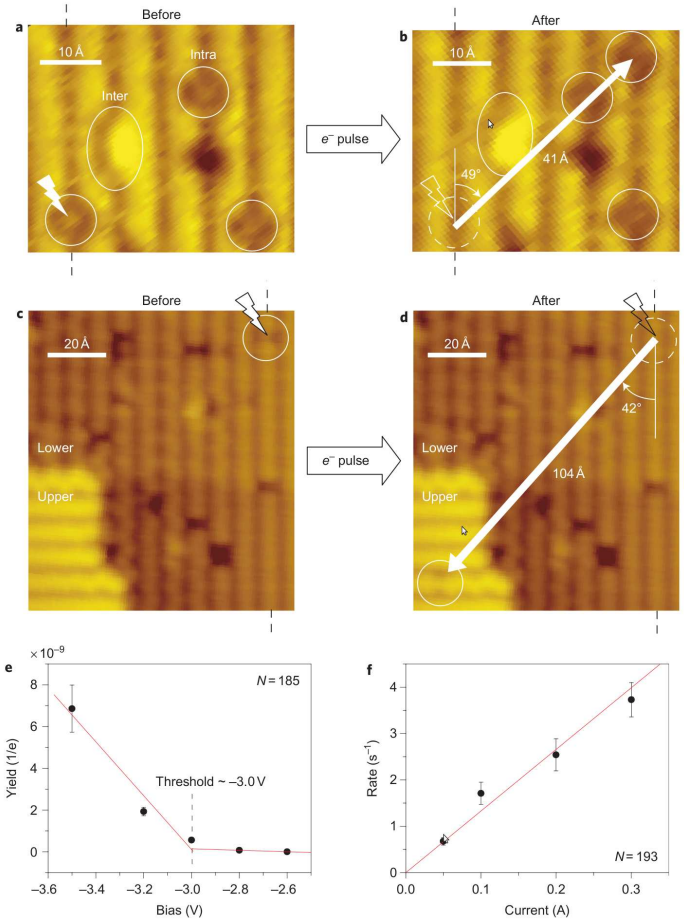

Figure 9.11: Bias dependent STM images of chemisorbed ethylene. Electron-induced ethylene migration [106]. a) STM image (+2.0 V, 0.2 nA, 25° C) showing three intra-dimer (circles) and one inter-dimer (oval) chemisorbed ethylene on Si(100). b) STM image of the same area after an electron pulse (−3.0 V, 0.2 nA, 0.5 s). The local pulse location is marked by a lightning bolt. A white arrow shows migration of the pulsed ethylene by 41 Å over a few surface features. Dashed lines above and below the images indicate the middle of a dimer rows. c), d) STM images of (−1.7 V, 0.1 nA, 25°C) of identical areas c) before and d) after an electron pulse (−3.5 V, 0.1 nA, 2 s) on the chemisorbed ethylene. White arrows shows ethylene migration by 104 Å onto an upper terrace. e) Yield of electron induced migration as a function of surface bias. A threshold of −3.0 V obtained assuming a linear threshold law. f) Rate of election induced migration obtained at a bias of −3.2 V as a function of current. A linear relation is observed indicative of a single electron process. Solid lines represent the best linear fits to the data.

observed data. To account for the observation a different mechanism has been proposed in which the molecule rotates upon recoil, which drives it in to cartwheel motion perpendicular to the direction of the surface.

Initially a part of the kinetic energy would be stored in rotational motion reducing the probability of desorption. The distance of a migration would depend on the rate of transfer of this rotational energy to the surface. This in-elasticity is expected to decrease over distance until the molecule is no longer able to escape the attractive potential of the surface atoms.

In order to support this scenario we have analysed the mechanism by which an initial rotation could be induced. The proposed scenario for rolling of ethylene molecules would have to be caused during the process of asymmetric bond breaking, which would create a torque on the molecule and initiate a rolling motion.

9.3.2 Theoretical methods

Theoretical simulations of the ground state of ethylene, the ground state of DFE physisorbed on the surface, and the final state of a reacted DFE molecule were performed using VASP [30, 32, 23]. A 4 × 4 supercell of Si(100) was simulated using a slab of eight layers with the bottom layer passivated by hydrogen. The adsorbate molecules and three surface layers were relaxed until forces on individual atoms were below 0.02 eV / Å. The cutoff energy was set to 350 eV.

The simulations used generalized gradient approximation (GGA) exchange correlation potentials and projector augmented waves to obtain the electronic ground state [107], and typically integrated the surface Brillouin zone of the system with only the gamma point. Based on obtained geometries, the origin of the torque was explored and the excited states of the ethylene molecule were simulated by the Delta Self-Consistent-Field (DSCF) method as implemented in GPAW. The ethylene calculations in GPAW where executed by Haiping Lin while NEB calculations of DFE were executed by Werner Hofer. The NEB simulations were undertaken with the VASP code using the same setings as specified earlier [25].

9.3.3 Results

The transiently occupied orbital was identified from the pool of unoccupied orbitals in the energy range from HOMO to HOMO+3.5 eV; it is shown in Figure (9.13).

Figure (9.14b) shows the results of calculations for a negatively-charged

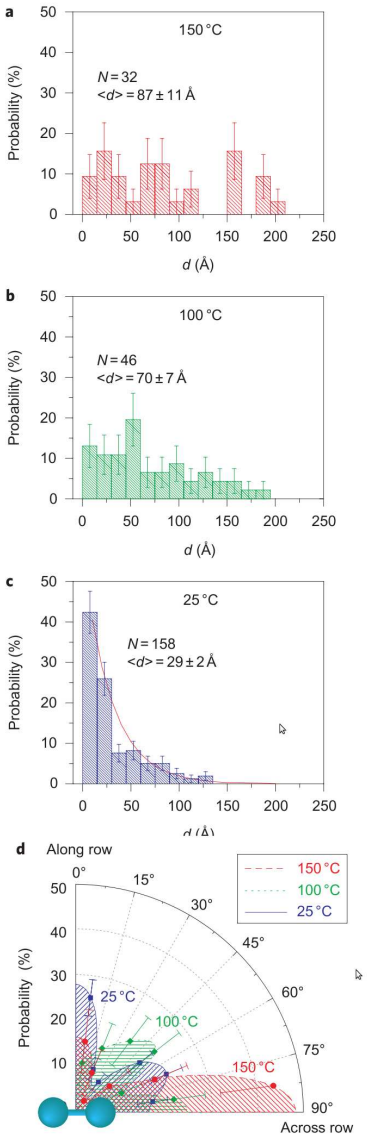

Figure 9.12: Radial and angular distribution of electron-induced migration at various temperatures [106]. a), b), c) Radial distribution (bin size 15 Å at a) 150° C b) 100° C and c) 25° C. Solid line is an exponential fit to the data. d) Angular distribution at 150° C (solid line) , 100° C (dashed line), 50° C (dotted line).

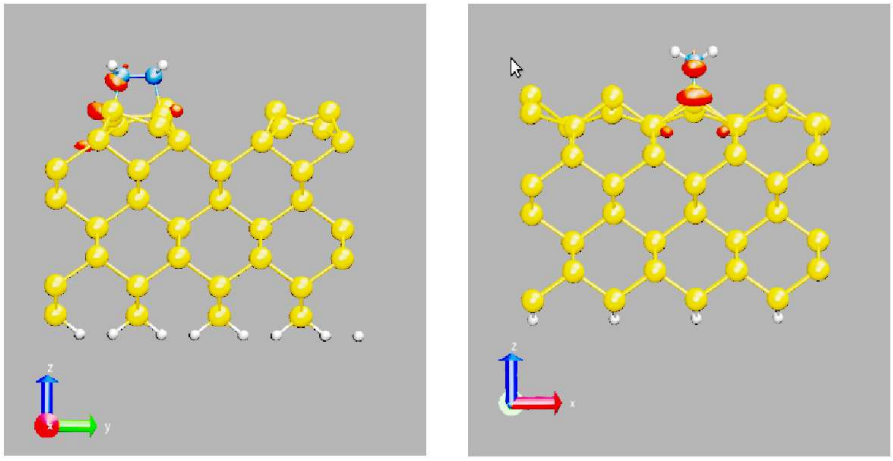

Figure 9.13: The figure presents a charge density of band 353 which was chosen as the main state participating in the process of electron stimulated migration [106]. Its energy is 3.08 eV above the HOMO level, and its shape is asymmetrical around the molecule, where the majority of the density is localized on one of the C–Si bond (calculated in GPAW).

chemisorbed ethylene following a Frank-Condon transition, i.e. without relaxation of the nuclei. The energy of the ionic state is calculated to be 3.08 eV above the ground state, in excellent agreement with the observed threshold for electron-induced reaction. The charge distribution in the excited state shows asymmetric charge localizations on the two C–Si bonds. The higher charge density on one C–Si bond is accompanied by a larger repulsive force (0.17 eV/Å) on the C atom, creating a net torque that could initiate motion along the direction of the C–C bond axis. The observed outcome depends, however, on the integral of this and subsequent forces in the negatively-charged state, and also following reversion to the ground potential-energy surface.

This was confirmed by means of a nudged elastic band calculation (NEB) for the reaction path-ways of difluoroethene in the process of asymmetric recoil during fluoridation of the Si dimer a) Figure 9.14a.

9.3.4 Conclusions

In conclusion, we demonstrate theoretical support for the long-range migration of ethylenic molecules on Si(100), induced by six surface reactions involving C–C π–bond formation. We show the generality of migration for (i) the thermal reaction of three related di–halo–alkanes and (ii) the electron-induced reaction of a series of three related chemisorbed alkenes at the same

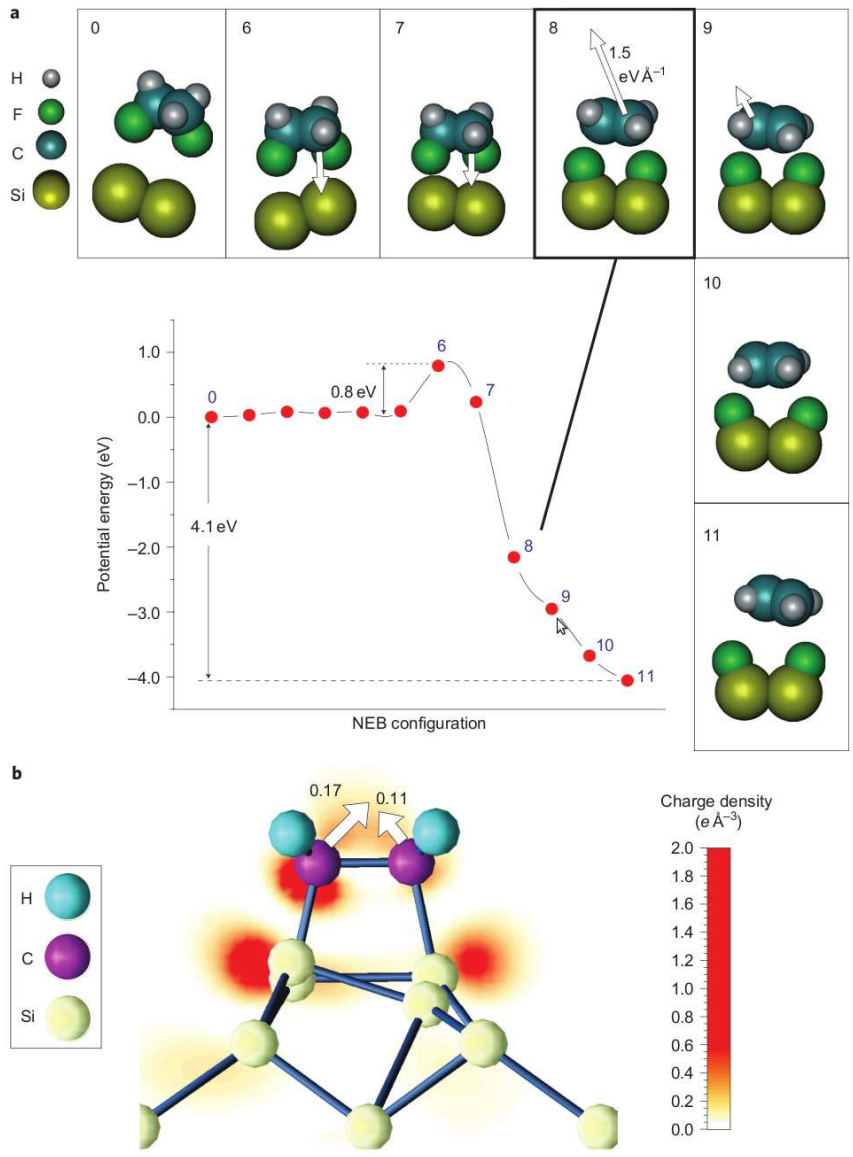

Figure 9.14: DFT calculation of thermal and electron induced recoil of ethylene [106]. a) Calculated minimum-energy path for the thermal dissociation of DFE on Si(100). Twelve NEB configurations from the initial state step 0 to the final state (step 11) were calculated. The presented slides present how the reaction proceeds. White arrows show differential forces on the carbon atoms. b) is a calculated charge distribution in the first excited state of chemisorbed ethylene on Si(100). White arrows represent forces on carbon atoms due to a Franck-Condon transition from the ground to the excited state.

surface. Each migratory event led at its terminus to a di–σ–bound ethylene (90 % intra–dimer, 10 % interdimer). Migration distances averaged 29 Å for the room-temperature surface, increasing to 87 Å for the 150° C surface and extending up to 200 Å. This long-range migration occurs despite the well known roughness of this surface that makes possible STM observation of adsorbates on Si(100) at room temperature. The observed migration is energized by the formation of a C–C π–bond. For electron-induced recoil of ethylene the migration is directed along the initial C–C bond axis in the chemisorbed state. The mechanism for the migration gives evidence of being rolling, rather than translation, of recoiling physisorbed molecules across the surface, because obstacles are surmounted and end-to-end inversion is exhibited. The rotation is induced by torque during the recoil of ethylene following surface di-halogenation (in three examples examined) or during the electron-induced recoil of the ethylenic molecules from their surface counterparts (in three further examples). Evidence of this torque comes from DFT calculations performed for both the thermal and electron-induced reactions. These findings open up possibilities for the use of chemical energy to direct long-range adsorbate migration across surfaces, and also offer a new means with which to study adsorbate–surface interactions during the course of surface migration. Directed molecular movement over many tens of Angstroms followed by chemical reaction offers a means to promote reaction at a distance. Additionally, the understanding of long-range migration should assist in applications that require substantial movement across a surface, such as molecular nanomachines [108, 109].

9.4 Acetylene on Si(100)

In this work we investigate a range of possible acetylene geometries on the Si(100) surface together STM simulations. So far, this system has received much attention because of its relevance to developing technologies. In this respect, various chemical processes and molecular configurations have been analysed due to their importance for applications in molecular electronics, or towards a comprehensive method of chemical and physical functionalisation [110]. The adsorption of simple hydrocarbons such as acetylene was found to be essential for analysis of the first stages in organic film growth.

9.4.1 Existing experimental and theoretical data

Due to its triple C–C bond, the acetylene molecule on Si is very reactive. It has been concluded that during acetylene chemisorption the stability of the silicon dimer bond is not affected [111]. It bonds to the Si–dimer by changing the hybridization of the carbon electrons from sp^3 to sp^2. According to early experimental accounts of acetylene adsorption, a di-σ-bonded molecule was believed to be the only stable configuration. However subsequent STM images and a careful examination have shown that this assumption may not be correct. In two articles by Terborg et al.[112] and by Xu et al. [113] it was claimed that two adsorption configurations exist, namely a di-σ-bonded (Figure 9.15, c and d) bonded to two Si atoms and a tetra-σ-bonded (Figure 9.15, f and g) configuration bonded to four Si atoms. This led to the proposition of stable tetra-coordinated configurations, which we shall call the ”pedestal” and "rotated pedestal" (Figure 9.15, f and g). Due to the unclear interpretation of experimental results, a series of theoretical studies have been conducted [114, 115, 116, 117, 118, 119, 120, 121]. The results of these simulations are summarized in Table 9.4. Adsorption energies of different configurations considered in theoretical studies using different theoretical methods are consistently higher for the di-σ than for the tetra-σ configuration. However, despite the agreement of theoretical studies upon the energetics, the interpretation of available STM images is still somewhat unclear [117, 120].

Notwithstanding the large number of published results, there are still controversial issues to address such as the appearance of the molecule in scanning tunneling microscopy (STM) images [118, 122, 123], or the influence of van der Waals (vdW) interactions on the energetics. VdW interactions have only recently been implemented in density functional theory (DFT) calculations, and it has been demonstrated that they may change the surface

and adsorbate distance and therefore have a non–negligible effect on the final result [124]. For these reasons we have decided to revisit the problem of acetylene adsorption on Si(100) with the improved theoretical methods to our disposition today.

The Si(100)-(2×1) surface is reconstructed due to the formation of dimers from top layer atoms, so that the number of dangling bonds is reduced by 50% (for more details see section 7.3. The surface is composed of Si–Si dimer rows, which in their energetic groundstate form a buckled c(4×2) structure. At room temperature however, the surface involves asymmetric buckling vibrations of the dimers, in effect causing a flip-flop motion between opposite buckling configurations. Due to the low time resolution of an STM, the surface is then imaged as a (2×1) reconstruction [44].

	(a)	(b)	(c)	(d)	(e)	(f)	(g)
(a) Double bridge						3.19	
(b) Double rotated bridge	3.72	2.79			2.93	3.35	
(c) Bridge	2.89	2.63	2.97	3.1		3.2	2.75
(d) Rotated bridge		2.53	2.87	2.5	2.63	3	2.45
(e) Ring		2.53					
(f) Pedestal	2.13	1.04	1.2	0.5		1.8	1.3
(g) Rotated pedestal	2.04	1.71	2.0	1.4	2.14	2.5	2.15
([125]) R-bridge Si -ring	3.08						

Table 9.4: Overview of theoretical adsorption energies (eV) of single acetylene molecules on Si(100)-(2×1). (a) Lu [125], (b) Morikawa [114],(c) Hofer [115], (d) Mezhenny [120], (e) Cho [116], (f) Kim [118], (g) Sorescu [119]. The bracketed letters next to the names refer to the configuration in the Figure 9.15. The R-bridge Si-ring configuration is the one proposed by Lu, where in addition to a standard rotated bridge the configuration contains a pair of uncoordinated Si-bonds.

In order to clarify the controversial issues we have performed a series of theoretical calculations. The first part of our analysis is focused on the investigation of different possible configurations and their energetic stabilities. We employed standard DFT, with the addition of post-process vdW simulations based on the Langreth–Lundqvist functional and also compared this set of simulations with DFT enhanced by semi-empirical simulations of vdW interactions. Subsequently, the most stable configurations were chosen for STM simulations.

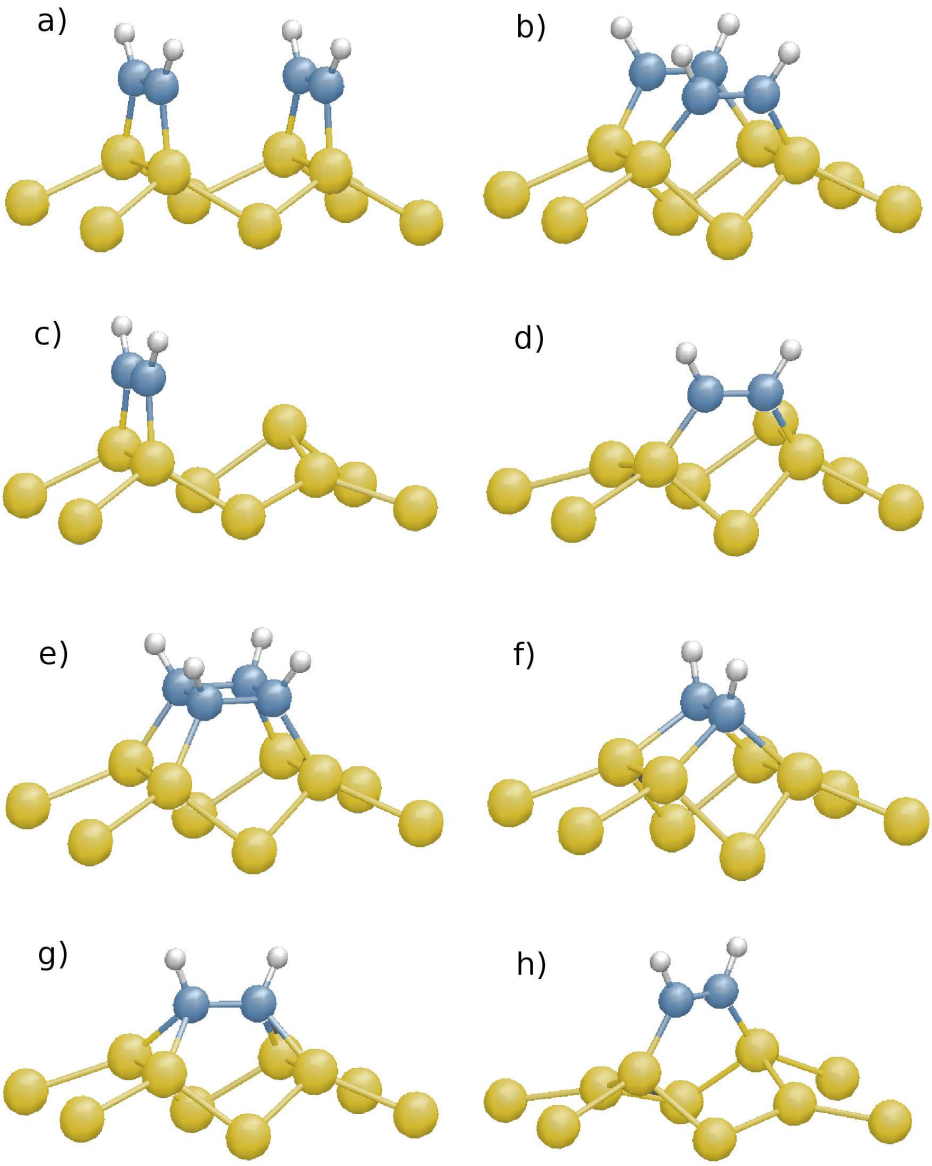

Figure 9.15: Adsorption configurations of acetylene C_2H_2 on Si(100)–(2×1): (a)double bridge – two adjacent bridge adsorption, (b) double rotated bridge – two adjacent rotated bridge, (c) bridge – directly above single dimer, (d) rotated bridge – between two ends of dimers adjacent in the dimer row, (e) ring – two acetylene molecules bonded in the four C ring between two dimers, (f) pedestal – four bonded parallel to the Si dimers, (g) rotated pedestal – four bonded perpendicular to Si dimers, (h) twisted bridge – diagonally between two dimers.

9.4.2 Theoretical methods

Because of the simplicity of the system in our investigations we mainly used non-self-consistent post-GGA methods to account for vdW interactions, which were, however, benchmarked against self-consistent iterations with semi-empirical vdW methods.

In post-GGA, the vdW functional is an approximation for the correlation energy alone [17], while the exchange energy is taken from standard GGA calculations. However, the right flavor of the GGA needs to be applied in order to avoid an overestimation of the exchange part of the binding energy [126, 127]. The DFT method used for the relaxation and for the calculation of electronic structure in our studies is the Vienna Ab-Initio simulation package (VASP) [31, 32]. In all simulations we employed PBE and RPBE functionals for exchange-correlation potentials and the projector-augmented-wave (PAW) method. The ionic relaxation was performed until the Hellman-Feynman forces reached values smaller than 0.02 eV/Å. The Si(100) surface, with its buckled dimer reconstruction, was mimicked by a c(4×2) supercell. The lattice constant was 5.46 Å [128]. The surface slab consisted of eight layers with a 19 Å, vacuum, the last two layers were kept fixed during relaxation. The bottom layer was passivated with two hydrogen atoms per silicon atom. The Brillouin zone sampling was limited to the gamma point.

Due to the requirement of accurate charge density representations also for the core regions, it was necessary to use a high resolution Fourier grid in the simulations. To this end the energy cutoff was set to 600 eV, in this case the neighbouring grid points of the real space grid have a separation of less than 0.1 Å. Based on the obtained charge densities the final step in our calculations was the calculation of vdW interactions. This approach allows adjustment of the resolution depending on the radial and angular coordinates of the atoms which minimizes the computational expense with negligible changes in accuracy [18]. Energy values obtained from standard DFT calculations in this step are updated by the vdW corrected correlation energies calculated according to 4.2.

The above two-step simulations were repeated for eight different configurations – bridge, rotated bridge, pedestal, rotated pedestal, twisted bridge, double bridge, double rotated bridge and ring – shown in Figure (9.15). In addition to simulations with non-self-consistent vdW corrections, we also performed self-consistent relaxations using semi-empirical Grimme corrections [20], where dispersion corrections take the form of $C_6 R^{-6}$ as described

in section 4.2.

9.4.3 Results and Discussion

Adsorption energies for single molecules were obtained with respect to a reference system composed of a clean surface and a single molecule placed in the middle of the vacuum. For multiple adsorptions the reference system similarly contained one molecule in the vacuum range while the other one was already adsorbed on the surface. All calculations were performed on a c(4×2) buckled ground state of Si(100). The coverage for single and double adsorption then corresponds to a coverage of 0.125 ML and 0.25 ML, respectively. The first set of adsorption energies is based on non-self-consistent calculations and presented in Table 9.5. We find that the most favourable adsorption configuration for acetylene is the double rotated bridge configuration (Figure 9.15). It is worth pointing out that there is an energy difference of 0.36 eV between the bridge and the double bridge far apart (Figure 9.16), which reflects the limited size of our unit cell: even the largest distance between two molecules in our unit cell does not completely decouple the molecules. Given the limitations of computational resources, this cannot be prevented. There is also a small difference in energy between adjacent and far apart double bridge configurations, slightly favouring the more distant setup, indicating a small repulsive potential, which is due to lattice strain. The pedestal and rotated pedestal configurations are much less stable. The same applies to the twisted bridge. These three configurations have therefore been excluded in the subsequent analysis.

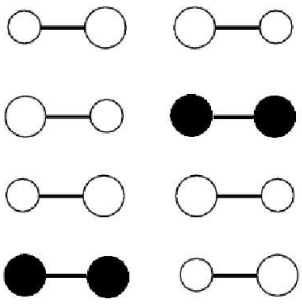

Figure 9.16: Ilustration of the unit cell of Si(100)–(2×1) with two acetylene C_2H_2 molecules adsorbed in bridge configurations above Si dimers located far apart from each other.

To gauge the validity of the non-self-consistent vdW simulations, we also performed calculations using semi-empirical but self-consistent methods for all configurations with adsorption energies above 2.0 eV. The results of our

	E (eV/molecule)
(a) Double bridge	2.65
(b) Double rotated bridge	3.17
(c) Bridge	3.08
(d) Rotated bridge	2.55
(e) Ring from rotated bridge	2.12
(f) Pedestal	0.65
(g) Rotated pedestal	1.39
(h) Twisted bridge	1.16
Double bridge far apart	2.72

Table 9.5: Results of calculation for adsorption energies of acetylene on Si(100) using non-self-consistent vdw-DF. The bracketed letters next to the names refer to the configuration in the Figure 9.15.

calculations are presented in Table 9.6. Simulations have been performed using both, RPBE and PBE functionals. As seen in Table 9.6 the difference in energies for most configurations is between 0.2 and 0.3 eV. For the ring configurations we find slightly higher differences of 0.4 eV, presumably because in this case the molecule is closer to the surface. Comparing self-consistent and non-self-consistent methods for the vdW interactions, we note very good agreement to within 0.1 eV for most configurations. However, the bridge turns out to be less stable by 0.26 eV and the ring more stable by 0.48 eV (see Table 9.7).

We have also analysed the bond length and its dependence on the method used. The bonds of interests are shown in Figure 9.17. The values for standard PBE (geometry used for non-self-consistent vdw), PBE+vdw and RPBE+vdw are included in Table 9.8. The general conclusion here is that the use of RPBE in the relaxation process produces sparser systems by slightly increasing the bond lengths with respect to PBE. Comparing PBE and PBE+vdW (non-self-consistent and self-consistent geometries) we find that all bonds are shortened except the C–H bonds. Self-consistent simulations based on Grimme corrections depend to some extent on the cutoff radius: they tend to overestimate vdW corrections for short bondlengths, and to underestimate them for long bondlengths. In our view this is the case for the bridge and the ring from the rotated bridge, which both show the largest energy difference between self-consistent and non-selfconsistent total energy values. In principle, all parameters in the simulations could

be analysed by a method developed by Hanke *et al.* [129]. However, since the ring from the rotated bridge, which shows the largest difference, is actually not backed by experimental data, we have omitted this analysis in the present work.

	E^{RPBE} (eV/mol)	E^{PBE} (eV/mol)	difference (eV/mol)
(a) Double bridge	2.47	2.72	-0.25
(b) Double rotated bridge	2.99	3.21	-0.22
(c) Bridge	2.56	2.82	-0.26
(d) Rotated bridge	2.25	2.57	-0.32
(e) Ring	2.20	2.60	-0.40
Double bridge far apart	2.46	2.74	-0.28

Table 9.6: Comparison of adsorption energies from self-consistent dispersion correction calculation for PBE and RPBE functional DFT-D for different configurations of acetylene on Si(100)–(2×1). The bracketed letters next to the names refer to the configuration in the Figure 9.15.

	E^{non-sc} (eV/mol)	E^{sc} (eV/mol)	difference (eV/mol)
(a) Double bridge	2.65	2.72	0.07
(b) Double rotated bridge	3.17	3.21	0.04
(c) Bridge	3.08	2.82	-0.26
(d) Rotated bridge	2.55	2.57	0.02
(e) Ring	2.12	2.6	0.48
Double bridge far apart	2.72	2.74	0.03

Table 9.7: Comparison of adsorption energies between self-consistent and non-self-consistent method for different configurations of acetylene on Si(100)–(2×1) . The bracketed letters next to the names refer to the configuration in the Figure 9.15.

9.4.4 STM simulations

In our theoretical work we aimed at analysing the experimental findings of Mezhenny (Figure 9.18), who presents three visually distinct configurations together with their line profiles [120]. Experimentally, the acetylene molecules appear as depressions compared to the non-reacted dimers, one configuration occupying an area corresponding to a single dimer (Figure 9.18,

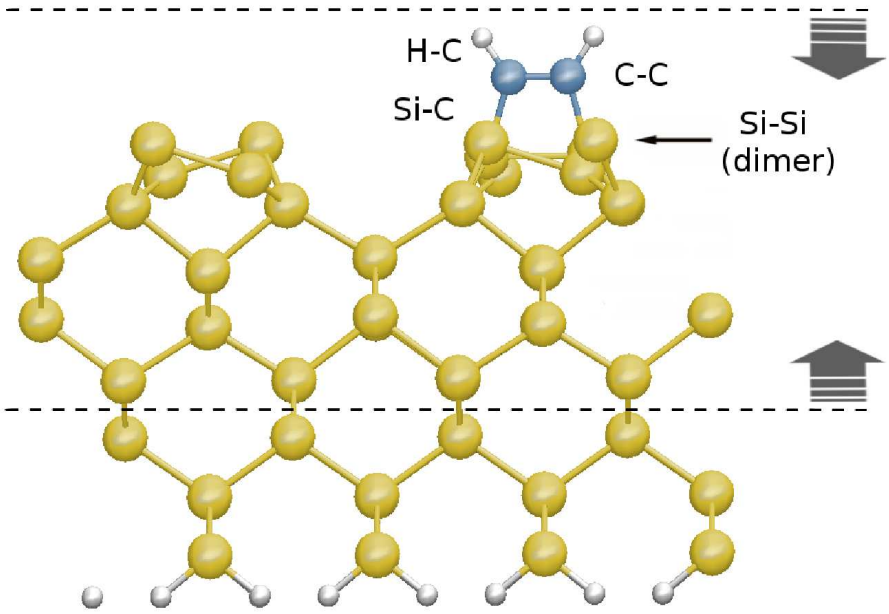

Figure 9.17: An example of super-cell used in calculations. The atoms included in between dashed lines undergo relaxation, during the self-consistent van der Waals calculations. The labelled bonds the ones considered in the discussion and included in Table 9.8.

I) and the other two occupying an area of two adjacent dimers of the same dimer row (Figure 9.18, II and III). The first approach to STM simulations discussed here is based on the Tersoff–Hamann approximation [130, 131], which is restricted to representations of the local density of states (LDOS). Images of our configurations using the TH method, together with line scans are presented in Fig. 9.19 for a bias voltage of -1.5 V and in Fig. 9.20 for a bias of -1.0 V. All images generated are for an LDOS value of 1×10^{-8}/ eV. The differences between configurations are unambiguous, and the obtained images were used to interpret all experimentally observed configurations.

In order to overcome the limitations of a finite unit cell size, which generally makes it impossible to find accurate contour values from a single simulation [115], we used a numerical interpolation scheme to mimic the transition from a non-reacted surface (at the edges of the unit cell) to a reacted surface (at the position of the molecule). While adjacent dimers are slightly higher in the reacted contour, they appear unchanged in the interpolated contour. We find that a double rotated bridge configuration has a similar shape and line–scan (Figure 9.19, b) as feature III, observed experimentally (Figure 9.18). However, for a bias voltage of -1.5 V the depth of the experimental depression is 0.6 Å, while it is 0.25 Å, theoretically. But this difference is partly

	H-C	C-C	C-Si	Si-Si
PBE				
Double R-bridge	1.096	1.364	1.924	2.436
Bridge	1.094	1.36	1.919	2.365
R-bridge	1.096	1.365	1.937	2.465
Ring	1.097	1.580(∥)	2.006	2.362
		1.575(⊥)		
PBE + vdW				
Double R-bridge	1.099	1.362	1.919	2.414
Bridge	1.097	1.359	1.911	2.362
R-bridge	1.098	1.362	1.925	2.427
Ring	1.100	1.579(∥)	1.997	2.353
		1.574(⊥)		
RPBE + vdW				
Double R-bridge	1.100	1.368	1.928	2.425
Bridge	1.099	1.364	1.921	2.367
R-bridge	1.100	1.369	1.943	2.449
Ring	1.101	1.587(∥)	2.010	2.361
		1.583(⊥)		

Table 9.8: Bonds length measurement for different configurations using standard PBE functional for relaxation with and without vdW correction.

due to an elevation of about 0.2 Å, of adjacent dimers in the experiments, which are used as reference heights (graph E-E' on Figure 9.18). It is known that bonding of molecules to silicon can lead to charging of adjacent dimers which then increase in apparent height [99]. In our simulations, the effort to reproduce also this feature in the experiments would become prohibitively expensive, as it requires the use of hybrid functionals and a doping of the silicon surface. Moreover, it has already been established in the cited paper what the origin of this effect actually is.

The other adsorption configuration with a double dimer footprint (Figure 9.18, feature II) which shows an asymmetric profile, can be attributed to a rotated bridge (Figure 9.19, d). In this case, there is no increased height for neighbouring dimers and our linescan in the direction across the dimers with a depth of 0.3 Å is in good agreement with experimental values. For the perpendicular direction the depth of the depression is 0.4 Å , again in good agreement with experiments.

The last configuration in the experiments (Figure 9.18, feature I), where

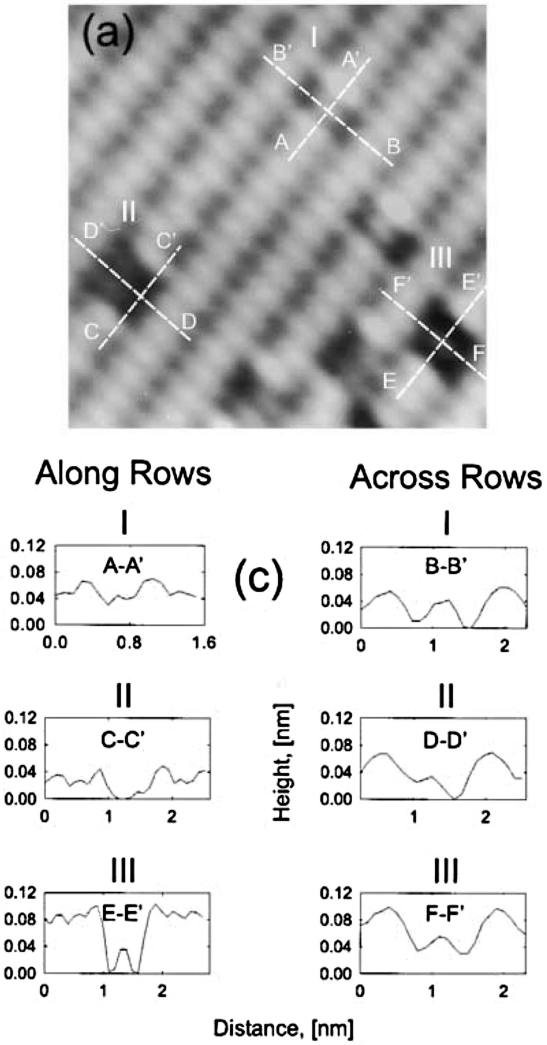

Figure 9.18: The experimental STM images [120] of acetylene C_2H_2 adsorption on Si(100)-(2×1) at -1.0 V sample bias.

the reacted site is 0.2 Å lower than adjacent dimers, is the bridge configuration (Figure 9.19, c), where we find a feature which has no apparent height compared to adjacent dimers. This can be understood considering the intrinsic limitation of DFT in simulating the width of the band gap of semiconductors. It is well known that DFT has the tendency to underestimate the band gap, which in our calculations would mean to sample the densities of states further away from Fermi level than in the experimental scans. For that reason, considering the experimental band gap of 1.1 V and the DFT band gap of about 0.6 V we decided to perform simulations also at -1.0 V bias and obtained following results (Figure 9.20).

All depressions in this case become deeper. The double rotated bridge 0.4 Å , the rotated bridge 0.4 Å and the bridge 0.1 Å , which with additionally

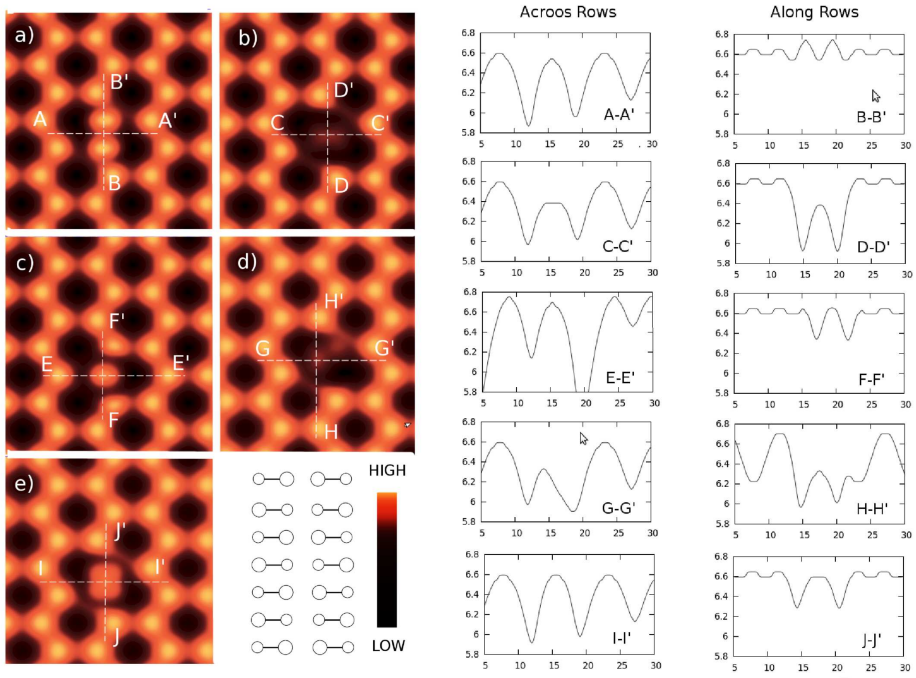

Figure 9.19: Simulated STM images for a density of states of 1×10^{-8}/ eV and a bias voltage of -1.5 V. The dotted lines on the right represent linescans across the images on the left. (a)double bridge – adsorption at two adjacent bridges, (b) double rotated bridge - adsorption at two adjacent rotated bridges, (c) single bridge – directly above a single dimer, (d) single rotated bridge – between two ends of adjacent dimers in a dimer row, (e) ring – two acetylene form a ring of four C atoms between two dimers.

included perturbation of adjacent dimers provides close to perfect agreement with the experiment. The other two configurations not considered in experimental studies have the following profiles; the double bridge configuration is seen as a protrusion of 0.1 Å for -1.5 V and a depression of 0.1 Å without considering the perturbation of adjacent dimers, and the ring configuration is of 0.0 Å height for -1.5 V and a 0.1 Å depression for -1 V bias, again without considering any additional effects.

9.4.5 Conclusions

We have calculated adsorption energies employing two methods, a self and a non-self-consistent one, accounting for vdW interactions for a set of possible configurations of acetylene on Si(100) surface. The obtained results agreed with the previously published trends without any strong effects on the hierarchy of the possible adsorption caused by vdW interactions. Simulations showed a good correlation between self and non-self-consistent methods ex-

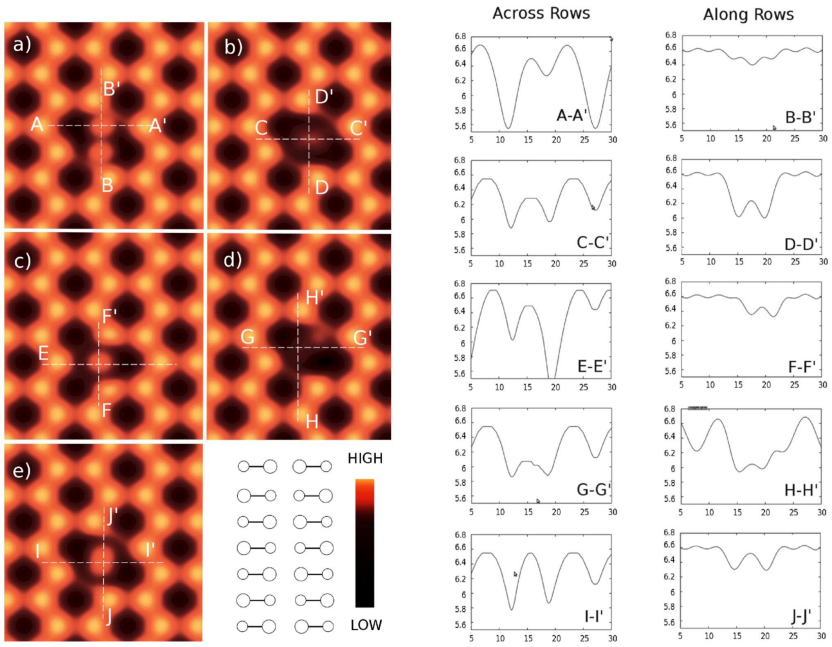

Figure 9.20: Simulated STM images using Tersoff–Hamman approximation for density of states 10^{-8}/ eV and bias voltage -1.0 V: The dotted lines represent linescans along which the profile of the image is presented on the graphs on the right hand side. (a) double bridge – two adjacent bridge adsorptions, (b) double rotated bridge – two adjacent rotated bridge, (c) bridge – directly above single dimer, (d) rotated bridge – between two ends of dimers adjacent in the dimer row, (e) ring – to acetylenes bonded in the four C ring between two dimers.

cept for the ring adsorption which deviated by 0.48 or 0.78 eV, depending on the starting configuration. The most stable configurations have been used to generate STM images and three of the configurations (double rotated bridge, rotated bridge and bridge) were very well matched with the experimental findings. The long prevailing problem, whether the double dimer depression is a single-molecule adsorption in a tetra–σ configuration or a two-molecule adsorption with a similar double dimer footprint can now be solved in favour of double adsorptions. Based on the energy calculations alone the ring configuration is proposed as another candidate for a stable geometry. However, there is no experimental match at present in the literature. Concerning STM simulations we highlighted the importance of the voltage bias adjustment and the charge agglomeration on the adjacent dimers.

Chapter 10

Towards high coverage: benzene on Si(100)

In this chapter we investigate some of the fundamental processes that may accompany high coverage molecular adsorption on semiconductor surfaces, while revisiting the long debated subject of benzene adsorption on Si(100). In our work, through calculations of total energies, transition barriers and simulations of scanning tunnelling microscopy (STM) images, we provide some new insights on both methodology and physics.

The interaction of a benzene molecule with a Si(100) surface has received great attention due to the importance of benzene as a model system for studying molecular adsorption of aromatic hydrocarbon molecules. In spite of the apparent ¨simplicity¨ of both benzene and the Si(100) surface, the ground state adsorption geometry of this system has been under debate for nearly two decades.

The adsorption takes place at the buckled Si(100) surface (see section 7.3) one would expect orientation–dependant reactivity. As shown in sections 7.3.1 on some occasions, molecular adsorbates significantly influence or even fix the surface buckling. This Si dimer pinning may, at some range, affect the surface character and its reactivity [99, 132]. The early experimental observations using near–edge X–ray adsorption fine structure (NEXAFS) measurements, combined with high resolution electron energy loss spectroscopy (HREELS) and thermal desorption spectroscopy (TDS) revealed that benzene molecules are chemisorbed on a Si(100)–(2×1) surface without molecular decomposition and two configurations can be distinguished [133, 134]. Since the early experimental accounts could not unambiguously determine the adsorption geometries, various theoretical models have been proposed and investigated [115, 156, 135, 136, 137, 138, 139, 140, 141, 142].

It has been agreed for all observed configurations that the bonding between the C and Si atoms is expected to be of σ nature. The geometrically possible adsorptions could be divided into two groups for the benzene molecule: di–σ bonded and tetra–σ bonded. In either case, all of the configurations have been considered and investigated in previous theoretical works.

For the di–σ bonded molecule on top of the single dimer, a C_1, C_2 or C_1, C_4 pair of C atoms could be engaged, while a C_1, C_4 pair alone could also bond in between two dimers along or across dimer rows, or even diagonally within the row (for visualization aid see Fig. 10.1).

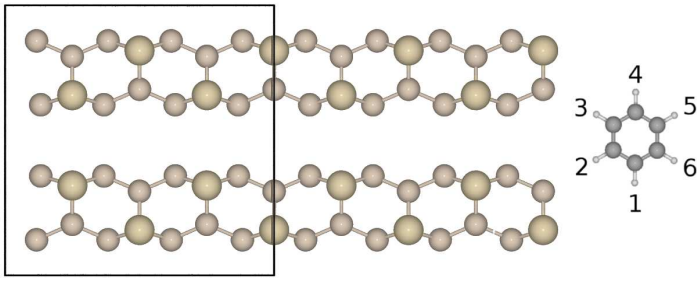

Figure 10.1: Si–c(4×2) surface reconstruction and a benzene molecule. The black frame represent the supercell and cream larger balls represent buckled up Si atoms.

For the tetra–σ bonded case, C_1, C_2, C_4 and C_5 atoms could engage in bonding, bridging two neighbouring dimers in the dimer row or alternatively a bonding of C_1, C_2, C_3 and C_4 atoms could form a tight bridge configuration, either symmetrical along the row called tight bridge (TB) or a 90° rotated version with respect to it.

On a basis of multiple theoretical investigations, two most stable configurations were determined for which the results are presented in Table 10.1. In each class, the most stable adsorption configurations obtained from first–principle calculations are the standard butterfly (SB) and tight–bridge (TB), respectively. As shown in Fig. 10.2, in the SB structure each benzene molecule reacts with the surface via a [4+2] cycloaddition, that is, the C_1 and C_4 atoms of benzene form two σ–bonds with two Si atoms of a dimer. The remaining C atoms are tilted up and the molecule has a C_{2v} symmetry. As a result, the C_1 and C_4 atoms are sp^3–hybridized and two π–bonds of the adsorbate are retained in the tilted C atoms. The TB structure, however, is a [2+2] cycloaddition product. Each benzene molecule interacts with two Si dimers with its C_{1-4} atoms, which are on a plane parallel to the Si surface. The C_5 and C_6 are sp^2–hybridized and tilted away from the surface. The adsorbate also shows a C_{2v} symmetry, in which the mirror plane is per-

pendicular to the [-110] direction. Regardless of the pseudo–potentials and exchange correlation functional used, the TB configuration is energetically more favoured than the SB configuration in all standard DFT calculations (Table 10.1). Supported by first-principle STM simulations, the SB structure has been assigned to the metastable adsorption state, while the TB structure is regarded as the ground state [115, 137]. This conclusion offers a logical explanation for the creation of TB in which SB is an intermediate state, less strained and thus more kinetically favourable, while TB is a final state which is energetically more stable. The evidence supporting this model can be found in examples of tip–induced conversion and desorption, demonstrating the possibility of back and forth switching between those states [143, 144, 145].

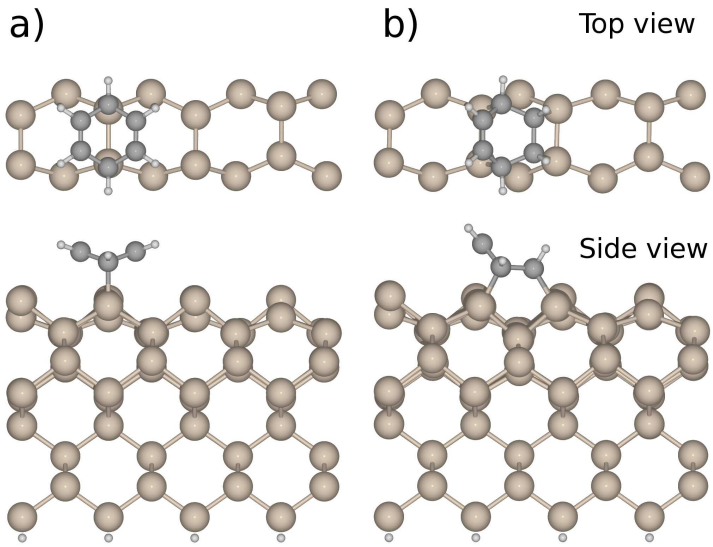

Figure 10.2: Adsorption geometry of an isolated benzene molecule on a Si(100)–c(4×2) surface: (a) the SB configuration and (b) the TB structure.

Although through this model an agreement with some experiments was reached, a fair group of experiments still remain where the TB state is either not observed or is a secondary state. This inconsistency between experiments posed new questions and raised doubts about the accuracy of both experimental and theoretical methods. A broad experimental analysis was recently presented by Nisbet *et al.* to which we refer the reader for more in depth review of experimental data [146]. Here, we will mostly focus on the theoretical side and on issues that have been omitted in earlier work. One of the latter

can be that, since the gradient–corrected density functionals are unable to describe dispersive interactions, van der Waals interactions between benzene molecules and the silicon surface are usually not included [147, 148, 149]. In order to correct for this methodological deficiency, Johnston *et al.* revisited this system with the van der Waals density functional (vdW–DF) [140, 141]. In their calculations, the structural optimization was performed using the PBE form of GGA and ultra–soft (US) pseudo–potentials. The total energy, however, was calculated to include the dispersion interactions [126]. In contrast to other results, this work has reported that the SB structure is a global minimum which is about 0.08 eV more stable than the TB structure regardless of coverage. It is important to note that the post–GGA total energy vdW–DF method employed in Ref. [140, 141] does not allow atomic relaxations when the van de Waals forces are calculated. Taking into account the small difference in the binding energies of two adsorption states, further structural optimization may play a decisive role in determining the ground state adsorption geometry. In order to investigate this further in our work we decided to use self–consistent DFT–D as suggested by Grimme in Ref. [20]. Here, the van der Waals interactions are included through the use of C_6R^{-6} semi–empirical dispersion corrections where C_6 is a coefficient for fixed atom pairs (see Section 4.2 for more details). Since this method allows ionic relaxations that also take van der Waals forces into account, the obtained geometry of adsorbed structures, *e.g.* concerning bond lengths, is more accurate than that from standard DFT calculations. This methodology has been employed throughout the work presented here. In Section 10.2, we also tested the reduced Grimme approach, in which vdW interactions between substrate atoms are not considered and vdW correction is limited to the molecule–substrate interaction.

As to this time, it has been pointed out in few publications that the discrepancy between different experiments may be related to coverage, defects or temperature. On one hand, the results are strongly temperature dependent via the effect on the rate of conversion between two states. Therefore, at low enough temperatures only single state occupancy would be expected. On the other hand, there is a difference in sample preparation between the STM studies and spectroscopic experiments. The first usually takes place at low defect density surfaces and lower coverages, while for the second the defect density is not considered and the measurements take place at high coverages. In many publications the unexplained reverse relative SB/TB population was observed and it was related to the increase of coverage. As a result, significant molecule–molecule interactions were suggested, which

Pseudopotential	GGA	SB (eV)	TB (eV)	Diff (eV)	Ref
PAW	PW91	1.00	1.25	–0.25	[155]
NC	BLYP	2.04	2.10	–0.06	[156]
US	PW92	1.12	1.42	–0.30	[115]
US	PBE	0.82	1.05	–0.23	[157]
US	PBE	0.92	1.19	–0.27	[140]
US	RPBE	0.47	0.66	–0.19	[140]
US	PW91	0.99	1.24	–0.25	[140]

Table 10.1: Computed adsorption energies (in eV) of the SB and TB configurations using different pseudo–potentials and generalized–gradient approximations (GGA).

could affect the energetics of the adsorption or the height of the barrier in the SB to TB transition. This subject has been for the first time theoretically approached by Lee *et al.* [139].

Here, we expand this discussion and also provide comparisons of DFT vs D–DFT. In Sections 10.5 and 10.6 we investigate the energetics for in–line interactions and the directionality as well as the inter–row interaction. We also provide comparison of the isolated vs full coverage SB to TB transition barriers.

In response to recently published high coverage studies, in which mixed SB/TB coverages were investigated [145], we also have performed a series of STM simulations for which the results are presented and discussed in the Section 10.7.

Finally, we present the calculations of the newly proposed geometry for stable benzene adsorption of inter-dimer butterfly (IdB) on the C–type defect [144]. We further expanded on this results and perform structural analysis of a high coverage version of the IdB configuration for which we also present simulated STM images in section 10.8.

10.1 Computational details

In this work, all calculations are carried out using the Vienna Ab–initio Simulation Package (VASP) [32, 80]. The electron–electron exchange–correlation interactions are described with the PBE form of GGA [13]. In order to accurately account for the ion–electron interactions, the projector augmented wave (PAW) method has been employed [22, 23]. The optimized lattice

constant obtained from Si bulk calculations is 5.47 Å, which is in agreement with a previous theoretical study [128]. The molecule and the five uppermost layers of Si atoms are allowed to relax in three dimensions.

The energy cut–off used in all calculations for the plane waves is 400 eV; the structural relaxation, carried out with the conjugate gradient method [150, 151], stops when the forces on each relaxed atom are smaller than 0.01 eV/Å. At the bottom surface of the supercell, all Si atoms are passivated by two H atoms per Si atom. In all calculations the vacuum range is about 23 Å.

The values of E_{ads} are determined by the following equation:

$$E_{ads} = E_{ref} - E \ , \tag{10.1}$$

where E is the total energy of chemisorbed benzene on a Si(100)–c(4×2) surface, and E_{ref} is the total energy of a reference system, in which the benzene molecule is kept about 10 Å above the surface.

10.2 Single adsorption

In these calculations, the silicon surface is modelled by a supercell which contains a 12–layer Si(100)–c(4×2) slab. Each Si layer contains 16 Si atoms and the surface consists of eight dimers, four per dimer-row. This set up results in 0.125 and 0.25 dangling bond saturation for SB and TB respectively. For the technical parameters, we note that, due to the large size of the supercell, the first Brillouin zone can be sufficiently sampled with the Γ point only. In order to understand the role that van der Waals interactions play in the adsorption process, three series of DFT calculations have been performed: (i) standard DFT, (ii) Grimme DFT–D and (iii) reduced Grimme DFT–D, in which the van der Waals interactions between Si atoms are excluded. The calculated binding energies per molecule are summarized in Table 10.2.

Methods	SB (eV)	TB (eV)	Difference (eV)
DFT	0.93	1.14	–0.21
DFT–D	1.55	1.84	–0.29
Reduced DFT–D	1.52	1.77	–0.25

Table 10.2: Binding energies (in eV) of the SB and TB configurations calculated with different methods.

As expected, both adsorption states are stabilized by taking van der

Waals interactions into account. A comparison of the binding energies obtained from the DFT–D and the reduced DFT–D calculations shows that the Si–Si van der Waals interactions do not have a significant effect on E_{ads} of benzene on Si(100)–c(4×2) surface. The increase of adsorption energies can be ascribed to surface–molecule dispersion interactions. Importantly, the DFT–D calculations indicate that the TB state is energetically more favoured than the SB state by around 0.29/0.25 eV for DFD–D/reduced–DFT-D, which is consistent with standard DFT calculations. This reveals that the van der Waals interactions do not change the relative stability of the SB and TB states. In this work, the parameters which need to be tested are the free atom radius R_{0i} and dispersion coefficient C_{6ii} for Si, C and H, respectively. Based on our calculation, the uncertainty $\triangle E_{ads}$ is 0.11 eV. This means that the TB state is more stable than SB state even if the R_{0i} and C_{6ii} vary by 5% for all elements [129].

A careful analysis of structural relaxations shows that the van der Waals forces do not affect the molecular structures of TB and SB states dramatically. The C–Si bond lengths are almost unchanged although the van der Waals interactions among the Si atoms introduce a contraction of the lattice constant by 1%. A Bader charge analysis also indicates that the local charge of all molecular atoms does not vary much [152].

10.3 Transition from SB to TB

Once it is established that benzene adsorbs on Si(100)–c(4×2) in a SB configuration which then turns into the more stable TB, it is then possible to calculate the transition barrier between the two states and hence the rate of conversion. In order to do that, we have employed the Nudged Elastic Band (NEB) method (calculations performed by Chiara Panosetti), as implemented in VASP 5.2.1, proposed by Henkelman and Jónsson [25] to search for saddle points, that is, transition states, and minimum energy paths (MEP) between known reactants and products. The NEB, as a chain–of–states method, is more computationally costly than a single relaxation, we thus employed a slightly looser convergence threshold of 0.02 eV/Å. The reaction coordinate was sampled using 3 intermediate replicas, for a total of 5 images (including the initial and final states), connected through a spring force of constant $k = 5$ eV/Å^2.

The optimized Minimum Energy Path for the conversion of chemisorbed benzene from the SB configuration to the TB configuration is shown in Fig. 10.3. The computed energy barrier is 0.75 eV. Experimentally, the

conversion barrier was estimated to be around 1.0 or 0.9 eV in two previous studies [153, 154] respectively, both calculated from the measured rate of conversion R using the Arrhenius equation,

$$R = A \cdot \exp^{-E_a/kT} \tag{10.2}$$

assuming the pre–exponential factor A to be 10^{13}.

However, several non vdW–corrected theoretical studies place the barrier in a range spanning 0.5 eV (Car–Parrinello method [156]) to 0.87 eV (Gradient Projector Method [139]) to 1.61 eV (Cluster method [138]). Hence, within our model, the conversion barrier lies in the range defined by theoretical literature but is underestimated with respect to the experimental values. However, the geometric features of the transition states are in perfect agreement with the results of Ref. [139]. The high value of cluster calculations indicates that the stiffness of the system, which can be influenced not only by its chemical composition and bonding structure, but also by its electronic structure and dopants, may play an important role in the absolute value obtained. Structural details of the transition state, compared to that from Ref. [139], are illustrated in Fig. 10.4 and Table 10.3.

We evaluated the ZPE correction in the harmonic approximation displacing the adsorbate degrees of freedom together with four underlying Si atoms by 0.005 Å. The Si atoms included in the displacement are those forming the dimer to which the butterfly benzene is attached, and the adjacent dimer toward which the adsorbate bends along the reaction path, which will become bonded in the tight bridge final state. The ZPE–corrected classical activation barrier is 0.67 eV. Using the quantum harmonic partition function with Wigner's formula [158] including the correction for tunnelling [159], we obtain an activation barrier of 0.70 eV.

Furthermore, roughly estimating the van der Waals binding energies of the initial state and the transition state, by means of single point calculations at the van der Waals optimized geometries, we find that, subtracting the van der Waals correction, the barrier increases to 0.79 eV. This is easily explained considering that in the transition state the molecule is closer to the surface, more atoms are thus involved in the interaction; the van der Waals binding energy is then larger for the transition states than for the initial state. This explains the lowering of the conversion barrier when the dispersion correction is included in the calculation.

A summary of all the computed conversion barriers is shown in Table 10.4.

Method	d_1	d_2
Gradient projector, no vdW [139]	2.45 Å	2.86 Å
CI–NEB, vdW	2.50 Å	2.91 Å

Table 10.3: Relevant structural details of the transition state in the conversion of benzene from BS to TB, that is, the lengths of the forming C–Si bonds (cfr. Fig. 10.4). There is substantial agreement between the Gradient Projector method, which does not include van der Waals, used in [139] and the Climbing Image NEB used in our calculation.

Method	E_a	Reference
Experimental I	1.00 eV	[153]
Experimental II	0.95 eV	[154]
Car–Parrinello	0.50 eV	[156]
Gradient Projector Method	0.87 eV	[139]
Cluster method	1.61 eV	[138]
CI–NEB, vdW	0.75 eV	–
CI–NEB + ZPE, classical, vdW	0.67 eV	–
CI–NEB + Wigner, vdW	0.70 eV	–
CI–NEB, no vdW (estimated)	0.79 eV	–

Table 10.4: Comparison of conversion barriers from literature with the present calculations. Our results lie in the range defined by previous theoretical calculations, but it underestimates the experimental value.

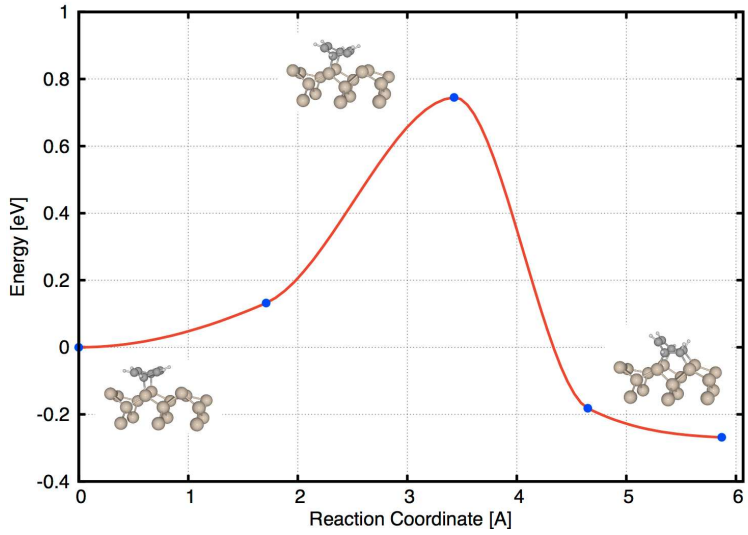

Figure 10.3: Computed minimum energy path for the conversion between BS and TB states of chemisorbed benzene on Si(100)–c(4×2) obtained using Climbing Image Nudged Elastic Band. The conversion barrier (classical) is 0.75 eV.

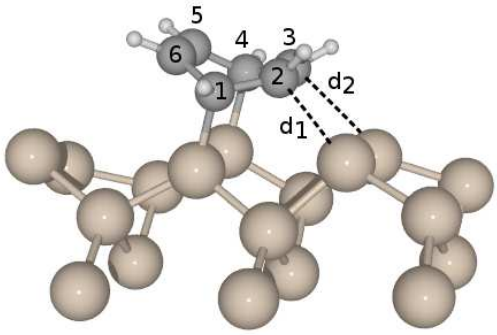

Figure 10.4: Relevant structural details of the transition state in the conversion of benzene from BS to TB, that is, the lengths of the forming C–Si bonds. Numerical details are given in Table 10.3.

It is also important to point out that at room temperature the Si dimers flip quickly up and down. In a theoretical model this feature is not trivial to consider; our simulation was carried out on a c(4×2) reconstructed surface. While the adsorption energies are not dramatically affected by the choice of either reconstruction, especially concerning chemisorption, it is clear that in a dynamical process involving a reaction path, the dimer flipping may also have a significant effect. This effect is particularly evident when an adsorbed molecule locally pins the surface in either configuration (see, for example, [132]), which, in this case, is unknown.

Finally, the underestimation of the conversion barrier with respect to

the experimental value can also be explained considering the limitations of the chosen theoretical setup. It is known that, in general, the employment of GGA–based functionals tends to underestimate activation barriers (see, for example, Ref. [160]). For the purpose of the present work, where we are mainly interested in investigating coverage effects, the underestimation of the barrier is not significantly changed at different coverages, which again points to a general, rather than a specific shortcoming in our theoretical model. We can thus still compare activation barriers in order to point out the effect of surface concentration on the transition from the butterfly configuration to the tight bridge (see Section 10.6).

10.4 Adsorption on C–defect

The clean Si(100) surface has several types of common imperfections, such as step and point defects, all of which could have an influence on surface properties or reactivity.

The Si(100) point defects have been categorized into three types: type A and B represent single and double dimer vacancy, respectively [51, 52]. The origin of the C–type defect was not clear from the beginning; different models were initially proposed, such as vacancies [53, 54], surface or subsurface defect atoms [55, 56] and water adsorption [57]. Recently, a conclusion has been reached and the C defect has been identified as a reaction site of a water molecule commonly also referred to as inter–dimer dissociation of water (ID). According to recent observations, the C–defect is an active site in benzene adsorptions [144].

In our study, we have performed DFT and DFT–D calculations of the adsorption geometry shown in Fig. 10.5. The adsorbates saturate 0.25 of the dangling bonds, two by a C-defect and two by an inter-dimer butterfly(IdB) adsorption geometry. The obtained bond length was 1.50 Å for Si–H and 1.68, 0.98 Å for Si–O and O–H, respectively. Both the OH and H are slightly spread apart in comparison to the Si atoms directly below, repelled from the axial position by 0.04 Å and 0.05 Å, respectively. The OH group is pointing in the direction of the neighbouring dangling bond, which is consistent with the studies of the C-defect alone (see section 8.2. The obtained adsorption energies of IdB on C-defect are 1.20 eV and 1.90 eV for DFT and DFT–D, respectively, which is also 0.06 eV higher than the TB configuration for both methods.

These values are slightly smaller than results obtained by cluster studies [144], however still supporting the inter–dimer butterfly as the most sta-

ble benzene adsorption configuration. Similarly to acetylene molecules on Si(100)–c(4×2), a secondary inter–dimer adsorbent on the same dimer pair has increased bonding energy [161]. In this case the reactivity of the inter–dimer butterfly (IdB) is increased greatly by ~ 0.43 eV in comparison to single IdB adsorption due the dissociated water occupying the other two atoms in bonded dimers (Fig. 10.5). From this observation, it is suggestive to assume that some of the increase in the binding energy results from reduced strain, due to stabilization of two dimers and decreased surface buckling. This will be further investigated in Sections 10.6, and 10.8.

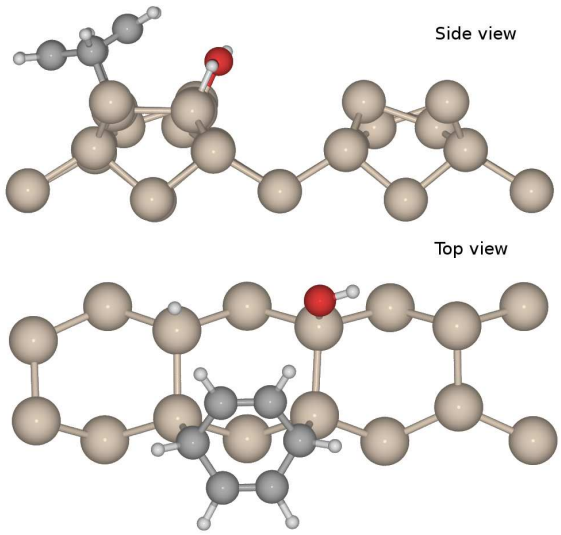

Figure 10.5: Adsorption geometry of an isolated benzene molecule on C–defect on Si(100)–c(4×2) surface. A C–defect comprises an adsorbed OH group and H atom on the nearby dangling bonds of neighbouring dimers, benzene molecules adsorbed in inter–dimer butterfly configuration.

10.5 Line coverage

In this section, we focus on the interaction of a benzene molecule with its neighbours. In these calculations, we increased the length of the supercell to double the size used in previous sections, i.e. to eight dimers in a single row. The Si(100)–c(4×2) cell used consisted of 7 layers of Si atoms with 8 dimers per row, thus a total of 16 dimers per unit cell. Each Si layer contains 32 Si atoms. Due to the large size of the supercell, the first Brillouin zone can be sufficiently sampled with the Γ point only. The energy cutoff used was 350 eV. All the configurations discussed in this section involve adsorptions on the single dimer-row keeping the other dimer-row unoccupied. In order to

understand the role that van der Waals interaction plays in the adsorption process, two DFT calculations have been performed: (i) standard DFT and (ii) DFT–D. The calculated binding energies per molecule are summarized in Table 10.5, while adsorbed geometries are presented in Fig. 10.6. Our aim in performing this calculation was to provide a more complete picture on higher coverage molecular adsorption and to investigate the possibilities of interaction between molecules with respect to energetics of adsorption. The first analysis presented here concerns the possibility of directional ordering. Two configurations, labelled with a) and b) in Fig. 10.6, are considered. In both a) and b) there are four molecules occupying eight out of sixteen dimers, saturating one dimer row accounting for a coverage of 0.5. In a) all TB molecules face the same direction along the line, while in b) one of the molecules is in reversed order. From the adsorption stability it is apparent that the direction does not influence the energetics enough to favour either of these adsorptions (see one way and one odd in a Table 10.5).

By comparing configuration a) and b) one can see that the TB molecule is reversed, thus its precursor SB molecule must have occupied a different dimer in each case. Earlier studies have shown that the difference between these two SB configurations is only ~ 0.05 eV which also does not support any directionality [139]. In all following configurations investigated in this section there are three benzene molecules reacting with eight dimers in one row as presented in Fig. 10.6 which due to mixed SB, TB character result in a different dangling bond coverage: 0.313, 0.375, 0.375, 0.188, 0.25 for c), d), e), f) and g), respectively.

Further, we considered whether there is any energetic directional preference for SB to TB conversion while surrounded by TB benzenes pointing in a single direction c) in Fig 10.6. In d) and e) this SB transforms to TB by collapsing to the left– and right–hand side respectively. The directional preference has been found to be only 0.026/0.030 eV for DFT and DFT–D showing only a slight side–specific preference, which is unlikely to have any statistical significance. Finally, we have performed SB to TB conversion in SB environments, here the obtained conversion energies have been found to be 0.30/0.39 eV, which is $\sim 0.05/0.06$ eV more exothermic than the conversion in a TB environment. This suggests that the SB to TB conversion energy decreases with an increase in TB population.

In structural analysis of single phase adsorptions of TB or SB no effects on angles or bond length were observed that could be attributed to the inter–molecular interactions. For the TB geometry (bonded with C_1, C_2, C_3 and C_4) C_2–Si and C_3–Si is 2.01 Å and for C_1–Si and C_4–Si is 1.99

Å with the angle C_3–C_4–$C_5 \sim 110°$ and the unbounded wing including C_5, C_6 at 52.5° from the surface plane (47° experimental [146]). For the SB geometry C_1–Si and C_4–Si are 1.97-1.98 Å depending on the buckling of the neighbouring dimers (1.93 Å experimental [146]) while the angle of the wing from the surface plane is 19.4° (15° experimental [146]). All the above DFT–D results were consistent with single molecule adsorption. From comparison of DFT to DFT–D the C–H and C–C and C–Si for TB bonds stayed unchanged while Si–Si and Si–C for SB shortened on average by 0.01 Å. A structural analysis of mixed high coverages will be given in Section 10.7 when we discuss the relevant STM images.

When studying phenomena on a clean Si(100) surface it is important to remember that adsorbates may affect the buckling in the neighbouring dimers. Comparing the height of the buckled dimer atoms of the clean surface with the atoms of unoccupied dimers on the left and right hand side of an SB adsorbate in c) in Fig. 10.6, it is observed that the up atoms are 0.1 Å lower while the down atoms are 0.05 Å higher, thus flattening the buckling. The same trend is present on unoccupied dimers in d), e), f) and g) in Fig. 10.6 where the lowering or raising of atoms are on average around 0.1 Å. The phenomenon of dimer flattening or pinning, although it does not seem to play as important a role in this particular system, will be discussed in depth in future publications.

Methods	DFT (eV)	DFT-D (eV)	
one way	0.000	0.000	(a) at Fig. 10.6
one odd	0.008	0.001	(b) at Fig. 10.6
TB environment			
SB→ left–TB	0.268	0.345	(c)→(d) at Fig. 10.6
SB→ right–TB	0.242	0.315	(c) →(e) at Fig.10.6
SB environment			
SB →TB	0.300	0.389	(f)→(g) at Fig. 10.6

Table 10.5: Full line relative adsorption energy of TB oriented in the same direction vs one odd TB oriented opposite direction. SB to TB conversion energy in one directional TB environment. SB to TB conversion energy in SB environment.

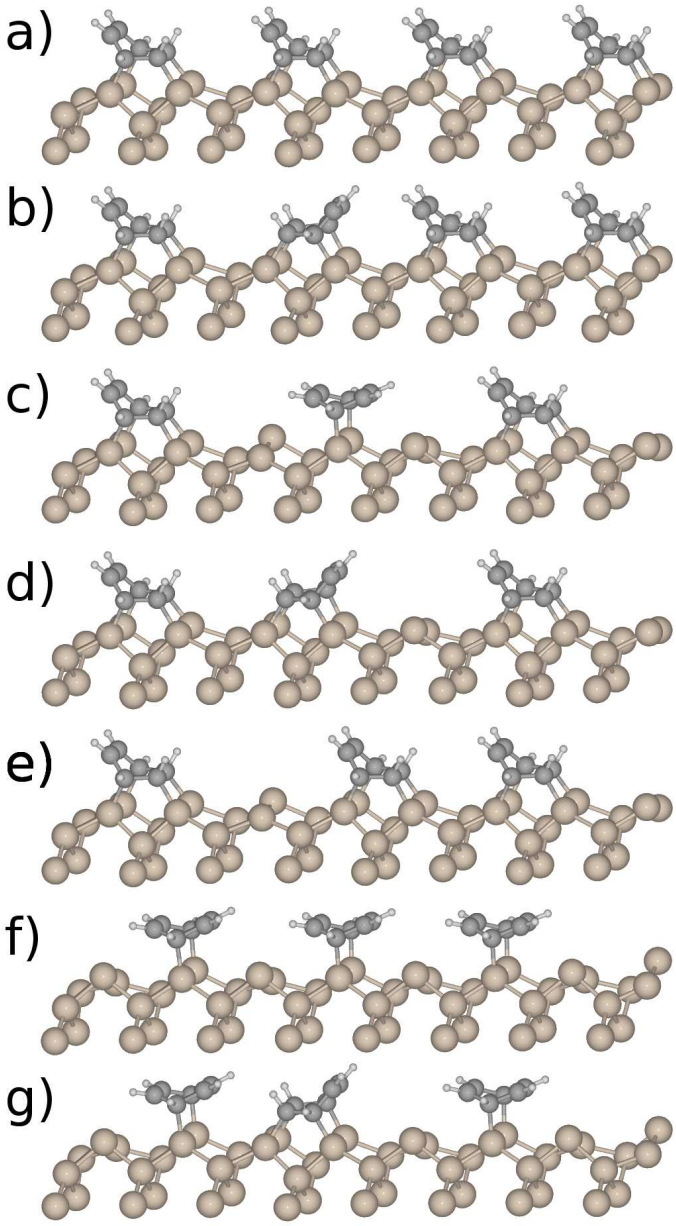

Figure 10.6: Adsorption geometries of benzene lines. a) Full line of TB adsorbates with the same directional orientation, b) Full line of TB adsorbates with a second TB oriented in opposite direction to the rest, c), d) and e) three metastable configurations in directional TB environment for SB, left-TB and right-TB respectively, f), g) two metastable configurations in SB environment, SB and TB respectively.

10.6 Full coverage

Full coverage calculations have been performed in order to investigate inter–row interactions as suggested by the work of Self *et al.* [162]. We have

obtained the adsorption energy differences related to correlations between dimer rows and investigated a few possible phases. The calculations were performed using a Si(100)–c(4×2) unit cell consisting of eight dimers. The adsorption configurations are shown in Fig. 10.7. Different full TB and full SB coverages were investigated. The energy differences obtained are presented with respect to the most stable configuration TB and divided by four, to give difference per benzene molecule. The results do not show any meaningful interaction between benzene adsorbates, suggesting no phase preference in any SB or TB full surface coverage. The average adsorption energy for TB is 0.25/0.3 eV higher than for the SB configuration which is close to the single adsorbate energy difference of 0.21/0.29 eV for DFT/DFT–D. This shows that with higher coverage line adsorption case in section 10.5 the average stability of TB over SB increases by $\sim$ 0.04/0.02 eV. From the structural analysis similarly to the high coverage case no geometrical changes could be attributed to molecule–molecule interactions. In each case there are 4 molecules per unit cell, di–σ bonded configurations a), c) and g) account for the 0.5 dangling bond coverage (which is a saturation coverage for the SB geometry) and tetra–σ bonded configuration b), d), e), f) and h) account for 1.0 dangling bond coverage (which is a saturation coverage for the TB or RTB geometry)

After performing the calculations presented in Section 10.4, we have decided to consider the IdB geometry in full coverage in which double dimer occupancy could in principle act similarly to the C-defect and stabilize buckling and increase adsorption energy as shown for double acetylene molecular adsorption by Czekala *at el.* [161]. In order to do that, the molecules were arranged in a zig–zag pattern as shown in panel g) of Fig. 10.7. The results (Table 10.6) show that, in fact, the prediction was correct and in comparison to single adsorption multiple adsorption increases stability. The average adsorption energy per IdB vs SB rises from –0.17 to –0.04 eV and from –0.08 to 0.09 eV for standard DFT and DFT–D calculations respectively.

Although from an energetic perspective, the IdB presence is much more expected than another di–σ configuration, it is still important to point out that this possibility is somehow limited due to the first single adsorption being less likely to occur. So far this high coverage geometry has not been considered, neither experimentally, nor theoretically. But it is possible that this phase has been interpreted as SB in spectroscopic studies, as it has a similar ratio of π and σ bonds. In this case, STM experiments will allow an unambiguous identification.

We have also performed the calculation of another four-sigma bonded TB

configuration, where the molecule is rotated by 90 °. The intention, with this simulation, was to show that high coverage does not change the adsorption energetics, unless it saturates both dangling bonds of a dimer without causing too much strain, as is the case for the zigzag-IdD. Rotated TB (RTB) gave energies of 0.22 and 0.23 eV for DFT and DFT–D respectively, which are similar to single adsorption. RTB adsorption has not been identified. The likely cause is that it only arises after conversion from IdB, which, as noted, is rather unlikely to occur.

Methods	DFT (eV)	DFT–D (eV)	
TB	0.00	0.00	(b) at Fig. 10.7
TB–shifted	0.00	–	(d) at Fig. 10.7
TB–reversed	0.00	–	(e) at Fig. 10.7
TB– rev. and shif.	0.00	–	(f) at Fig. 10.7
SB	0.25	0.31	(a) at Fig. 10.7
SB–shifted	0.25	0.31	(c) at Fig. 10.7
IdB–zigzag	0.22	0.29	(g) at Fig. 10.7
RTB	0.22	0.23	(h) at Fig. 10.7

Table 10.6: Relative adsorption energies for different phases of full coverage adsorption of TB and SB configuration and one full coverage adsorption of RTB and zig-zag IDB adsorption. The energies were obtained in reference to the lowest energy configuration TB therefore the most stable ones are those with the lowest value. The discussed configurations are presented on Fig. 10.7.

To complete the picture, we investigated the effect of intermolecular interactions on the conversion barrier between SB and TB, performing a NEB calculation at full coverage. With respect to the isolated adsorption case, the difference is that the neighbouring benzene may cause steric hindrance to the conversion, as well as influence the buckling of the unoccupied dimer which could in effect change the activation energy. These calculations were performed with a c(4×2) super–cell including eight dimers in two dimer rows. The use of two dimer rows is necessary to avoid an artefact due to the boundary conditions. Had we employed a supercell containing only one row, this would have corresponded to the simultaneous transition of an infinite line of benzene molecules from SB to TB. The initial state consists of four benzene molecules in the SB configuration, while in the final state one of the benzene molecules is converted to the TB configuration.

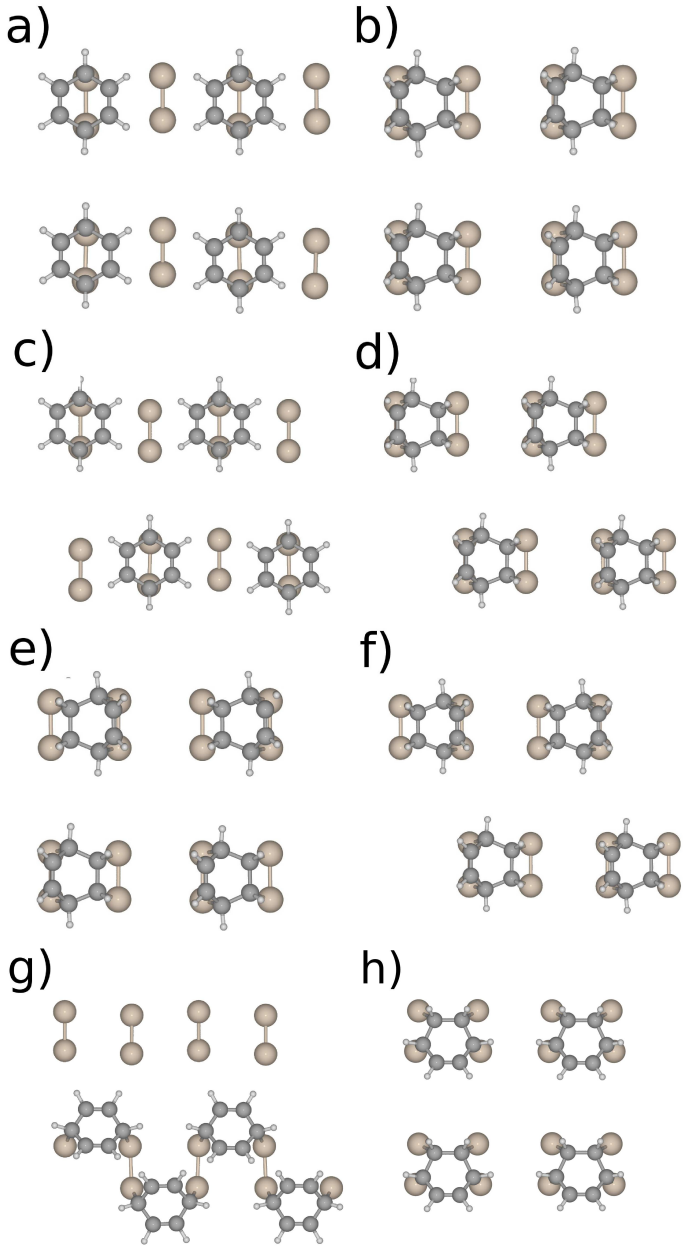

Figure 10.7: Adsorption geometries for full coverage of benzene on Si(100)–c(4×2) surface. Panels a) and d) represent standard and shifted SB phases while b), c), e) and f) represent standard, reversed, standard–shifted, reverse–shifted phases of TB–type adsorption, g) IdB–zigzag, h) RTB-type adsorption

The computed conversion barrier at full coverage is 0.74 eV which is only 0.01 eV lower than single adsorption. Hence, the hypothesis of the population reversal can not be attributed to high coverage molecular interaction as the effect on the conversion barrier due to the neighbouring benzene molecules is negligible.

10.7 STM simulations

In this section we present STM simulations using the Tersoff–Hamann approach [130] as implemented in BSKAN [137] for a bias voltage -1.0 V and local density of states (LDOS) value of $1 \times 10^{-8} states/eV$ In order to provide some additional insight into the STM image interpretations of high coverage cases in our analysis, we considered groups of mixed SB/TB adsorptions. The adsorbed configurations together with their STM images are presented in Fig. 10.8. We chose the geometries in such a way as to provide a full picture for all the predicted possibilities. In Fig. 10.8 panel a) the mix consists of right–handed TB's (r–TB) and SB's. From the profile of the first three molecules (r–TB, SB, r–TB) one can see how the overlap in the local density of states (LDOS) could make it difficult to distinguish the exact structure. It is important to notice that, due to the asymmetry of the structure, the depression in between the first two molecules is more prominent than in between the second two. Additionally, due to a slight repulsion from the right–hand side the SB is tilted to the left (C–Si bond angle in respect to the dimer row is 89.3° , and the difference in height between opposing C and H atoms is 0.27 and 0.32 Å, respectively). This can also be observed in the profile of the image. The image of the 3rd and 4th (r–TB, r–TB) molecules in a) shows another asymmetric feature which can be used to determine the direction of the adsorption. Here, the overlap is much weaker than previously and a stronger depression is visible. The gradient of the left molecule's profile is lower than the right one. The asymmetry of the feature in between two r–TB or two l–TB can therefore be used in interpreting the direction when lower or higher gradient can determine whether they represent the TB side which is bonded to the surface or tilted away from it. The image of 4th and 5th (r–TB, unoccupied dimer (UD), r–TB) can be analysed similarly with respect to the different gradients; here, however, the depression is much deeper and UD states are visible. In Fig. 10.8 panel b) we analyse the symmetrical arrangements with 1st, 2nd, 3rd (l–TB, SB , r–TB) and 4th, 5th, 6th (r–TB, SB, l–TB) molecules creating two characteristic images of narrow and wide profile.

In both cases there is a large overlap of LDOS creating a high profile. However, in the second case the profile is wider due to two maxima from tilted-up sides of TB adsorptions. The prominent depression in between TB and SB is another distinguishable feature, which is stronger and further apart for a second case. In Fig. 10.8 panel c) we investigate symmetric TB adsorptions with an unoccupied dimer in between them (1st, 2nd and 3rd,

4th molecules). Here the situation is similar to b), creating narrow and wide versions in the middle; however, UD states exposed in the middle of the profile are slightly more prominent for this case with a more open profile. In Fig. 10.8 panel d) we have simulated only a TB population. Here, another two profiles can be distinguished for pairs of 1st, 2nd and 3rd, 4th molecules (l–TB, r–TB and r–TB, l–TB). One can recognize the strong overlap created between tilted up from the surface parts of the TB's in the first case and a wider profile with more prominent middle depression for the second pair. Finally, in 10.8 panel e) we have examined an SB only population. Here also two cases can be distinguished with a single and double unoccupied dimer in between the molecules 1st, 2nd and 2nd, 3rd respectively. All the profiles are in-plane with strong overlap of first pair and a prominent depression for a second pair.

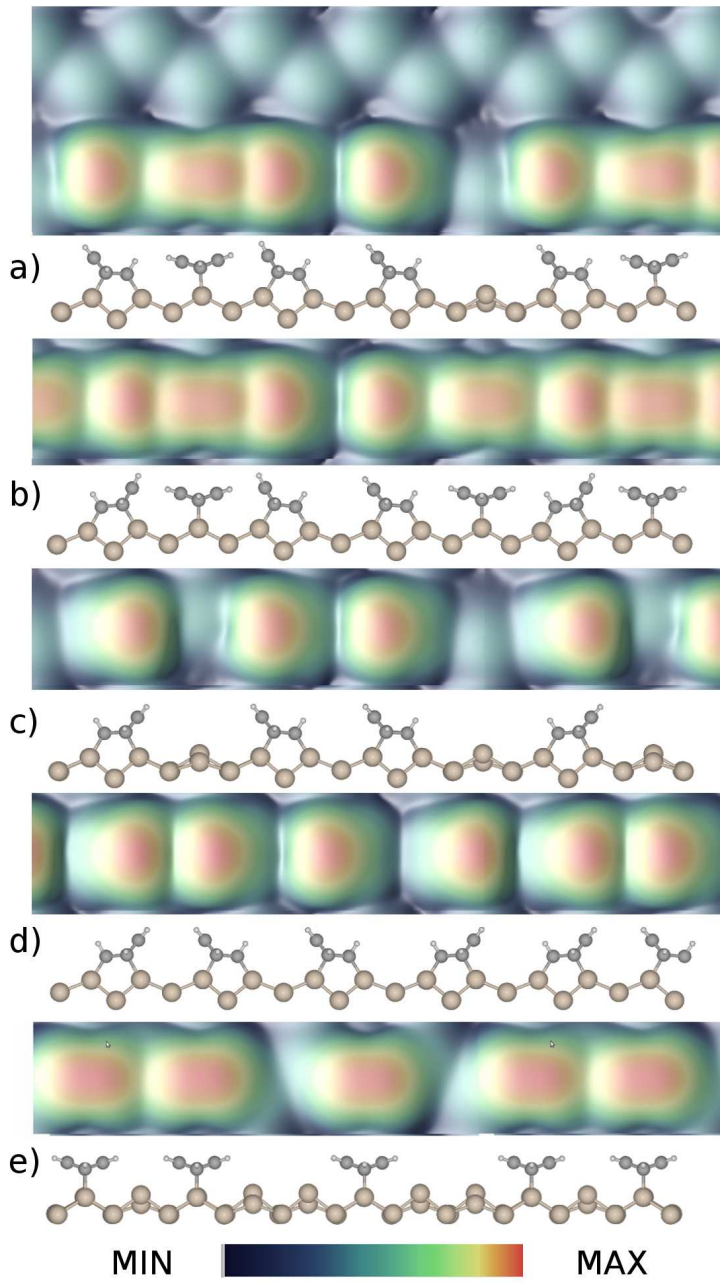

Figure 10.8: Simulated STM images of high coverage mixed SB and TB adsorptions of benzene molecule on Si(100)–c(4×2) surface for -1V bias and isosurface of LDOS $10^{-8} states/eV$ together with the related structural representations.

10.8 Structural analysis

In this section we focus on a further analysis of IdB stability in the higher coverage geometries. We investigated the structural changes that may accompany high coverage adsorption. It is known that due to dimer buckling the coordinates of the atoms in the layer below have to change, which creates

a more/less packed environment (down/up buckling) causing the opposite buckling in the next dimer [49]. It has been demonstrated that adsorbed molecules can have a strong effect on their surroundings. This in turn could lead to a more or less stable adsorption site for the next adsorbate. In Table 10.7 we compare a set of parameters for different IdB adsorptions in order to characterize the structural changes and their possible relation with adsorption configurations. At the top of the table we present s–IdB (single IdB) adsorption and the reference to the higher coverage cases. The chosen parameters are two angles of C–Si bond α with respect to dimer row and β with respect to the dimer, and two distances a(Si,Si) between IdB bonded Si atoms and b(Si,Si) between the two Si atoms in the layer below(see Fig. 10.9). The analysed adsorption are n–TB–IdB (IdB in narrow TB environment) Fig. 10.9(a), w–TB–IdB (IdB in wide TB environment) Fig. 10.9(b), SB–IdB (IdB in SB environment) Fig. 10.9(c) , C–IdB (C-defect adsorption) in Fig. 10.5 and z–IdB (zig–zag IdB adsorption) in Fig. 10.7(g). The comparison of the α shows very little variation, which would be expected due to the structural rigidity in this direction. The molecule is expected to be bent more in the direction described by β, where bonds are more flexible. The maximum bend of $\sim 6\ ^\circ$ is observed in the z–IdB case due to the repulsion of adjacent benzene molecules. For a and b distances the change is more prominent for the n–TB– and w–TB– cases, in which the a distances are increased by 0.04 Å due to the strain induced by the adjacent tetra-σ-bonded TB molecules. When these results are compared to the simulated energies, it can be seen that for the n-TB, w-TB and SB cases the neighbouring molecules add additional strain to IdB, which lower the adsorption energy making this configuration even less likely than s–IdB by ~ 0.11 and ~ 0.17 eV respectively. We conclude that higher coverage does not reduce the strain, and the increase in energetics of C– and z– cases should be attributed to electronic effects mainly, due to the changes in the electronic structure of the dimer.

In addition to the structural analysis we have also performed STM simulations of the w–TB- , n–TB- and SB–IdB configurations. In Fig. 10.9 we considered two structures of IdB with neighbouring symmetrical TB adsorptions (l–TB, IdB, r–TB and r–TB, IdB, l–TB) and one with neighbouring SB (SB, TB, SB). Similar to what was discussed earlier in Fig. 10.8 panel b) there is a clear distinction between the narrow a) and wide b) profile in Fig. 10.9. In a) and b) LDOS of TwB is strongly asymmetric with respect to the dimer row with a narrower profile comparing to SB adsorption, thus not creating any strong overlap in the LDOS between neighbouring molecules. In

	α (°)	β (°)	a(Si, Si)	b(Si, Si)
s–IdB	77.2/78.7	105.8/114.8	3.77	7.71
n–TB–IdB	77.2	109.8	3.81	7.87
w–TB–IdB	77.2	110.4	3.81	7.87
SB–IdB	77.4/77.7	113.2/113.9	3.78	7.77
C–IdB	77.9	110.7	3.77	7.73
C-IdB, vdW	77.9	110.4	3.77	7.73
z–IdB	78.6	116.1	3.76	7.74
z–IdB, vdW	78.6	116.3	3.77	7.73

Table 10.7: Structural information for group of different geometries: single adsorption of IdB (s–IdB), IdB adsorption in narrow TB environment (n–TB–IdB) (panel a) in Fig. 10.9), IdB adsorption in wide TB environment (w–TB–IdB) (panel b) in Fig. 10.9), IdB adsorption with SB environment (SB–IdB) (panel c) in Fig. 10.9), IdB adsorption on a C-defect C-IdB in Fig. 10.5, zig–zag IdB adsorption (panel a) in Fig. 10.7). Here, α is angle of C–Si bond with respect to dimer row direction, β is an angle of C–Si bond with respect to the involved dimer (two numbers are present if buckling still persist in underlying structure), A is the distance between both Si atoms involved in bonding IdB molecule, B is a distance between two pairs of Si atoms in the layer beneath the Si dimer (see Fig. 10.9).

c) the overlap is much more prominent with a similar height of the profile for both SB and IdB thus concealing the IdB's features slightly; the asymmetry is still visible which is a characteristic signature of the IdB geometry.

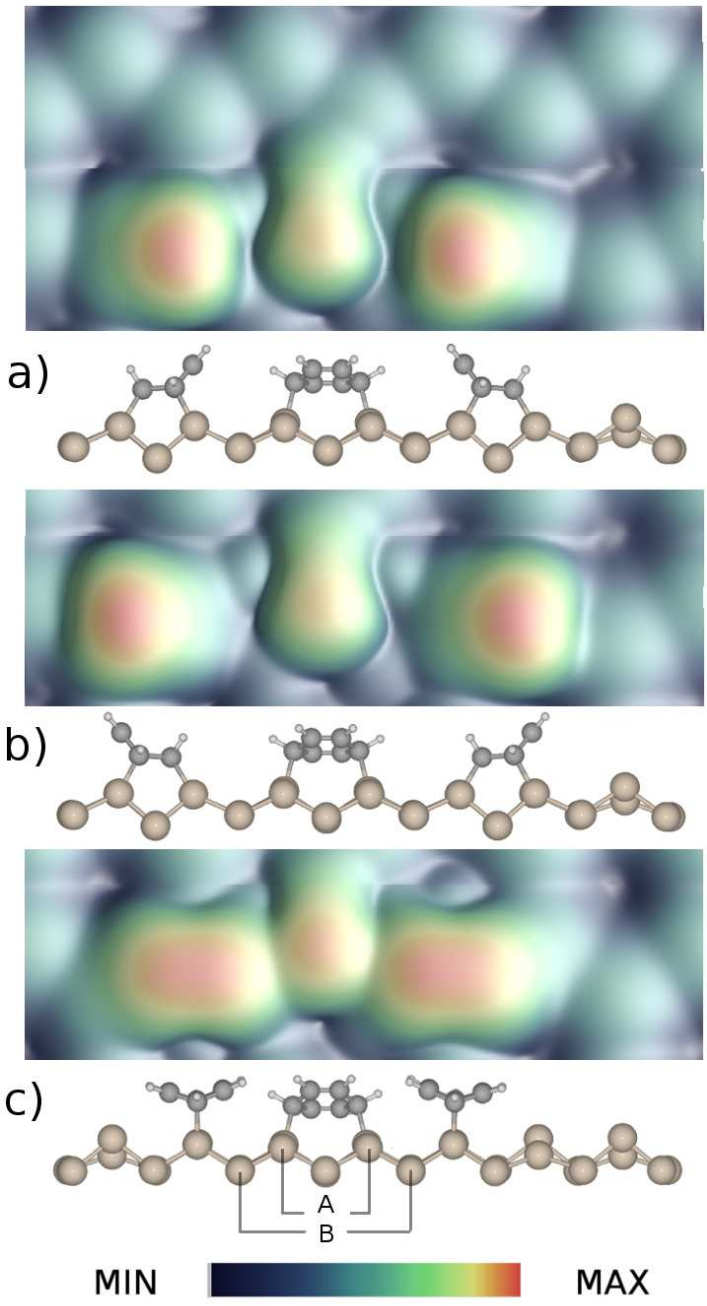

Figure 10.9: Simulated STM images of high coverage mixed SB/TB with TwB adsorptions of benzene molecule on Si(100)–c(4×2) surface for −1.0 V bias and isosurface of LDOS $10^{-8} states/eV$ together with the related structural representations.

10.9 Conclusions

In summary, our calculations of the single adsorption geometries agree with the other results previously obtained using different DFT functionals. The most stable adsorption observed is the tight bridge (TB) in Fig 10.2b), which is 0.21/0.29/0.25 eV more stable than Standard Butterfly (SB) (panel a) in Fig. 10.2) for DFT, DFT–D and reduced DFT–D. The transition barrier obtained is 0.75 or 0.79 eV with and without dispersion correction. Overall, Grimme's dispersion correction slightly decreases the bond length and contributes to stronger bonding and transition barrier lowering. Additionally we also corrected the barrier by ZPE contributions and obtained a barrier height of 0.67 eV and 0.70 eV including the correction for tunnelling. Furthermore, for the C–defected surface the calculations of inter–dimer benzene IdB adsorption has confirmed the proposal of another energetically stable benzene configuration on the C–type defects, with adsorption energies of 1.2/1.9eV which is 0.27/0.35 eV higher than that of SB and 0.44/0.43 eV higher than IdB alone, for DFT and DFT–D respectively. In the light of these results and cluster calculations presented at Ref. [144], we confirm the strong evidence for this configuration on C–defected surfaces. We also highlighted the effect of increased adsorption energy due to double dimer adsorption, which in this case has been achieved by OH and H but is also possible by means of other molecules, as shown in a double sided intra–dimer adsorption of acetylene molecule in Ref. [161]. We successfully tested this idea with high coverage zig–zag IdB in Fig. 10.7g) and observed the increase of adsorption energies to $-0.04/0.09$ eV in comparison to SB adsorption making it more likely to appear in this phase than as a single adsorption which is $-0.17/-0.08$ eV, for DFT and DFT–D respectively.

These phenomena can be important not just in hydrocarbon mono-layer growth but also in other self-assembly applications such as for nanoscale device manufacturing.An example of this was recently shown by Belcher *at el.*, where the benzonitrile molecules were used as nucleation and termination sites for metallic chain-growth [163].

In our high coverage analysis of SB and TB states, we have found no significant environmental effect on the activation barrier, energetics or any directional selectivity in SB to TB conversion. Based on full coverage calculations, we conclude that TB is still the most stable configurations. For a single–state full coverage no phase preference has been found, indicating the observed phases in Ref. [162] are statitically equally probable and the interactions in between dimer rows are negligible.

We have also performed a high coverage STM analysis providing all the possible profiles expected in the mixed and singular SB and TB adsorption and highlighted a range of characteristics that may ease the interpretation of the geometries. We also presented the mixed SB/TB with IdB adsorption to provide full description for another analysed adsorption configuration. In addition we provided structural analysis of the high coverage IdB configurations and concluded, that the neighbouring adsorbates do not stabilize the IdB but instead creates additional strain further decreasing the adsorption energy. The gain in IdB stability can be attributed to change in electronic structure of doubly occupied dimer.

No answer to the problem of high SB populations can be given from the perspective of any surface mediated interaction. According to the above analysis, we conclude that benzene adsorption on Si(100) is expected to appear in a SB configuration at first as it is kinetically preferable, then, depending on environmental conditions, it transforms to a TB configuration. It is expected that for low coverages all adsorbates can undergo transformations. For high coverage one would expect the final populations to be a mix. These results should not be attributed to molecule–molecule interaction, as the total energy and NEB calculation proves, but should be expected as purely geometrical restrictions, due to the fact that the SB molecule only needs one empty dimer to adsorb, while TB needs two. The adsorption of SB may therefore be possible while the conversion to TB is restricted. This, in effect, causes mixed populations in high coverage cases. An additional possible factor could be IdB adsorption which is energetically comparable to SB in a high coverage zig–zag phase which could impact the population ratios in the spectroscopic studies as presenting the same σ vs π signature as SB. The above studies were also performed to test the idea of environmental control for metastable adsorptions. On the basis of our results, we can conclude that the surface mediated environmental interactions are not sufficient for effective control of the SB/TB conversion.

Chapter 11

Thin–film photovoltaic absorbers

11.1 Introduction

Despite offering an alternative energy source, PV cells are still far from being affordable without government subsidies. This is because they are still above the threshold of 1US $ per Watt offered by the standard fossil fuel-derived electricity. Nevertheless, this is expected to change in the near future, early this year the price for German PV cells was estimated around 2$ per Watt which is half of the price from 2010 [175]. The rapid rise of Chinese PV manufacturing further increased competition in global PV market, with prices of Chinese cells already reaching 1$ per Watt and lower. According to an observed trend, commonly called Swanson's law, it is suggested that the cost of a photovoltaic cell falls by 20 % every time the total global manufacturing capacity doubles. The constant modernization, automation of large scale production and recent innovations in material science are soon expected to make PV cells both environmentally and economically viable. The conversion of sunlight into energy has been a subject of interest for a few decades now, with Si single crystalline PV cells dominating the market, although there are a range of different technologies now offering alternative and promising routes to solar energy production. This will open a great range of applications in the future (see Fig. 11.1 for a historical overview).

In fact, silicon is not an ideal PV material, because it has an indirect band gap which reduces its adsorption coefficient to 10^3. The implication of this is that a direct band-gap material such $GaAs$, which has an absorption coefficient of 10^5, can be 100 times thinner than an equivalent Si absorber. [176]. As shown in Fig. 11.1 solar–cell technologies can be divided into single-

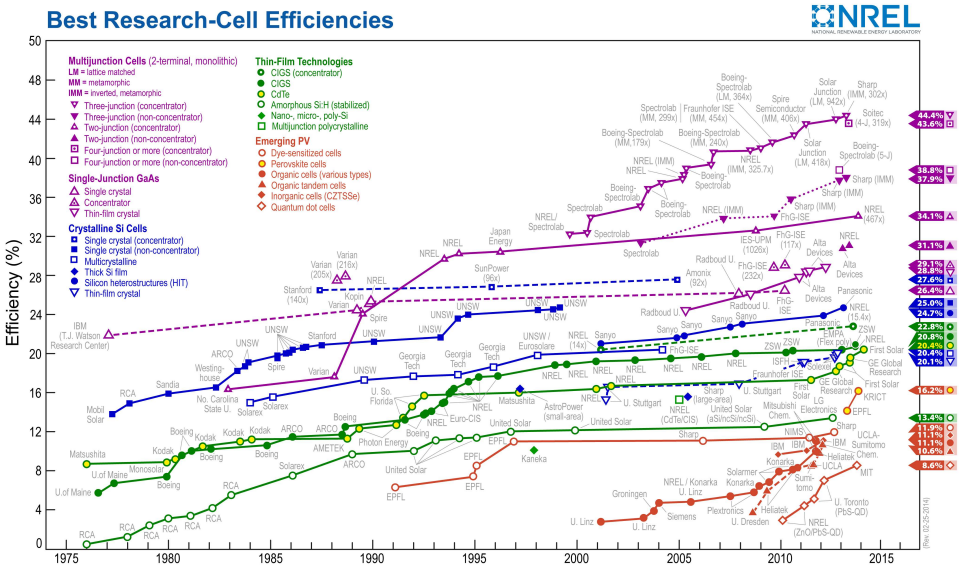

Figure 11.1: Historical accounts of PV solar–cell technologies. [177]

or multijunction cells. Furthermore, depending on the material used, they can be classified into single crystal or thin-film polycrystalline solar cells; in addition to these there is a new group of emerging PV technologies, such as dye-sensitized cells or organic quantum dots cells, which trade very cheap production cost for still relatively low efficiency [178].

This chapter will focus on one of the available technologies, called thin-film photovoltaics; which in contrast to the standard Si PV cells are made of polycrystalline absorbers. These greatly simplify the production process, that can be done by a range of Ultra–High–Vacuum (UHV) and non-UHV methods.

According to Powalla *et al.*, thin-film technologies have a high cost-reduction potential at high production [179]. The outstanding issue is the cost and availability of indium and gallium which are the main components of the best $Cu(In,Ga)(Se,S)_2$ thin–film solar cells [180]. To solve this problem, a new quaternary material has been proposed. $Cu_2ZnSn(S,Se)_4$, in which every element from the III group (In, Ga) is replaced by a pair of atoms from groups II and IV (specifically, Zn and Sn). In that way the material is entirely made of abundant elements with the row element price for Zn 2$ /kg, Cu 7$ /kg, Sn 20 $ /kg, instead of Ga 300$ /kg, In 550 $ /kg, which offers a significant cost reduction [181]. These materials have not been long used as photovoltaic absorbers and the highest efficiency reached so far is 9.7 % [182].

The work presented here is concerned with both groups of PV absorbers cited above. One of the chosen materials is $CuInSe_2$; an alloy of this has

been used as a commercial PV absorber and is commonly known as $CIGS$ which represents the family of $Cu(In, Ga)(Se, S)_2$ materials. The alloying process has been found to allow the control over the polycrystalline structure characteristics and phase uniformity, which ultimately resulted in higher performance of the PV device. Other investigated materials are pure structures of the $CZTS$ group of alloys which in the longer notations represent $Cu_2ZnSn(Se, S)_4$ compounds.

The basic structure of a $CIGS$ or $CZTS$ thin-film solar cell is depicted in Figure 11.2.

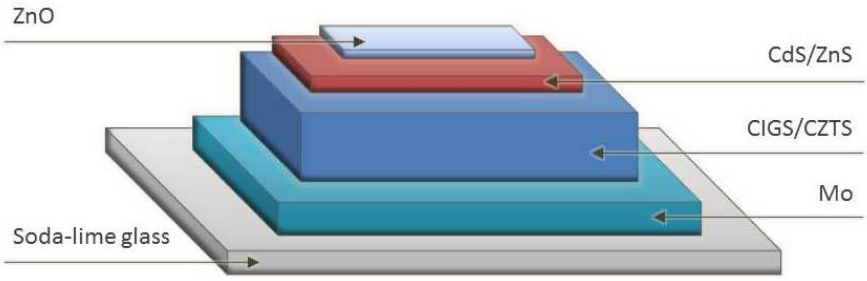

Figure 11.2: The general structure of a thin-film solar-cell.

The most common substrate for supporting PVC is soda-lime glass, 13 mm thick and coated on one side with molybdenum (Mo); this serves as a metal back contact. The hetero–junction is formed between the semiconductors $CIGS$ or $CZTS$ and ZnO, buffered by a thin layer of CdS or ZnS and a layer of intrinsic ZnO. The $CIGS/CZTS$ is doped p-type from intrinsic defects, while the ZnO is doped n-type to a much larger extent through the incorporation of aluminium (Al). In $CIGS$ this asymmetric doping causes the space-charge region to extend much further into the ZnO. Matched to this are the layer thickness's and the band-gaps of the materials. The wide $CIGS$ layer serves as absorber with a band-gap between 1.02 eV ($CuInSe_2$) and 1.65 eV ($CuGaSe_2$). For $CZTS$ band tuning is still an unresolved issue. The light absorption is minimized in the upper layers, by the choice of larger band-gaps: e.g. $ZnO = 3.2eV$ and $CdS = 2.4eV$, $ZnS = 3.5eV$. The doped ZnO also serves as front contact for current collection. Laboratory scale devices, typically 0.5 cm^2 large, are provided with a Ni/Al-grid deposited onto the front side to contact the ZnO.

Most of thin-film photovoltaics have so far been developed empirically. The improvement has often been made by trial and error, only some of the results were later backed up by theoretical models. This approach may

change in the near future, with rapidly increasing computational power and new scientific methods. Theoretical materials science offers a glimpse into the material world through the quantum lens, allowing quantum design of the quantum system.

11.2 CIGS

The $CIGS$ compounds crystallize in the tetragonal chalopyrite structure represented by the $I\bar{4}2d$ (D_{2d}^{12}) space group (see Fig. 11.3). This group is an isoelectric analogue of III-V binary compound semiconductors. The $CuInSe_2$ structure could be discussed from the perspective of the zincblend structure, where each anion is coordinated by two different pairs of analogous cations, Cu and In. This coordination leads to the formation of two different cation-anion chemical bonds with two different lengths. Since the $Cu-Se$ bond is stiffer than $In-Se$ the Se atoms are slightly displaced from the ideal zincblend positions. The unit cell used is a double of the zincblend in **c** direction containing eight Se anions, four Cu and four In cations which is giving rise to slight anisotropy in the c direction, thus $\eta \equiv c/2a \neq 1$.

11.2.1 Phases

In addition to the chalcopyrate structure, another polymorph has also been observed for $CIGS$ films, $CuAu$. It has been found that the chalcopyrate phase is 0.2 meV/atom more stable then the $CuAu$ type structure and that this value rises to 0.9 meV/atom in case of $CuGaSe_2$. Polymorphism has been associated with the reduced performance of the solar cell due to increased interface related recombination. In the case of CIGS it has also been found that the $CuAu$ phase could cause an overall reduction in the band gap, therefore even further decreasing the solar cell performances. One way to counteract the creation of unwanted phases and to increase the cell efficiency is through alloying of $Cu(In, Ga)Se_2$ [183].

11.2.2 Computational details

For the optimization of the bulk unit–cell, the calculation have been performed using PBE-PAW potentials and GGA functional with a cut off energy of 300 eV and $5 \times 5 \times 3$ Monkhorst–Pack [21] k–mesh sampling as implemented in VASP. The ionic relaxation has been performed until the force per atom has been smaller then 0.01 eV/ Å.

$CuInSe_2$	Theoretical	Experimental [184]
Unit cell size		
a=b	5.89Å	5.782Å
c	11.80Å	11.620Å
c/2a	1.005	1.001
Bond lengths		
Se-In	2.67Å	
Se-Cu	2.45Å	

Table 11.1: The structural results for chacopyrite structure of $CuInSe_2$ comparison of experimental data with optimized structure.

11.2.3 Results

The relaxations have been performed until the lattice constants (see Fig. 11.3) The structural parameters obtained are presented in Table (11.2.3). The lattice constants obtained by simulations are in good agreement with experimental values.

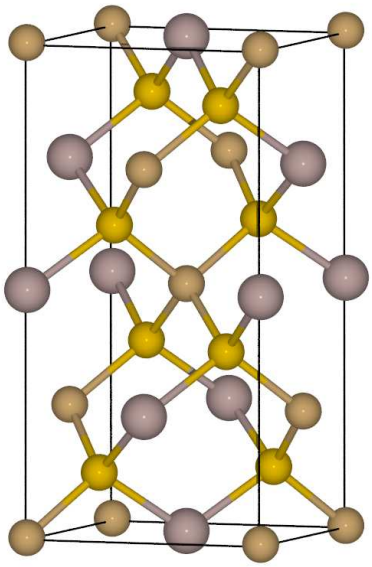

Figure 11.3: Unit cell for $CuInSe_2$ – chalcopyrite crystallographic structure. The different atoms are represented by the following colours: brown – Cu, grey – In, orange – Se.

11.3 CZTS

In comparison to the chalcopyrates, the array of the anion atoms is unchanged in $CZTS$ structures, occupying one half of the tetragonal sites. There is however a change in the coordination of the cations. This is due to the substitution of the In atom with a pair of Zn and Sn atoms, introducing an additional complexity. For every Se atom there are two Cu and one Zn and Sn cation thus a wider range of alternative phases is possible. This has been investigated in recent theoretical studies [185, 186, 187, 188]. The proposed phases can be characterized by the symmetry of $I\bar{4}$, $I\bar{4}2m$, $P\bar{4}2c$, $P\bar{4}2_1$ and $P2$ space group. From the above, the kesterite ($I\bar{4}$) structure has been identified both in the experimental and in the theoretical studies as the most stable. Additionally, another $I\bar{4}2m$ phase has been found called stannite [189, 190, 191, 192]. Nevertheless, the exact $CZTS$ crystal structure identification has not been a straight forward one because Cu^{+} and Zn^{2+} are isoelectronic thus the X-ray diffraction is unable to distinguish between the two phases and alternative experimental techniques are required. One such technique is neutron diffraction which has been successfully used to identify that both sulphite and selenite based materials crystallize in a kesterite structure. In recent such studies although the phase have been identified, a disorder between Zn and Cu sites has also been observed indicating a possibility for short range cationic displacement and deviation from a major phase [193]. This possibility is supported by the earlier mentioned theoretical studies which predict the second most stable phase to be $P\bar{4}2c$ in which there is a slight intermixing of Cu and Zn atoms within the $Cu - Zn$ plane.

Here, we decided to investigate the kesterite and stannite phase due to the significant structural differences and yet still competitive energetics, for details see A and B in Fig. 11.4.

11.3.1 Computational details

For the optimization of the bulk unitcell, the calculations have been performed using PBE–PAW potentials and GGA functional with the cut of energy 300 eV and $5 \times 5 \times 3$ Monkhorst–Pack [21] k mesh sampling as implemented in VASP. The unit cell size similarly to $CIGS$ is a double of the zincblend in the **c** direction containing eight anions Se or S, four Cu , two Zn and two Sn cations. The ionic relaxation has been performed until the force per atom has been smaller then 0.01 eV/ Å.

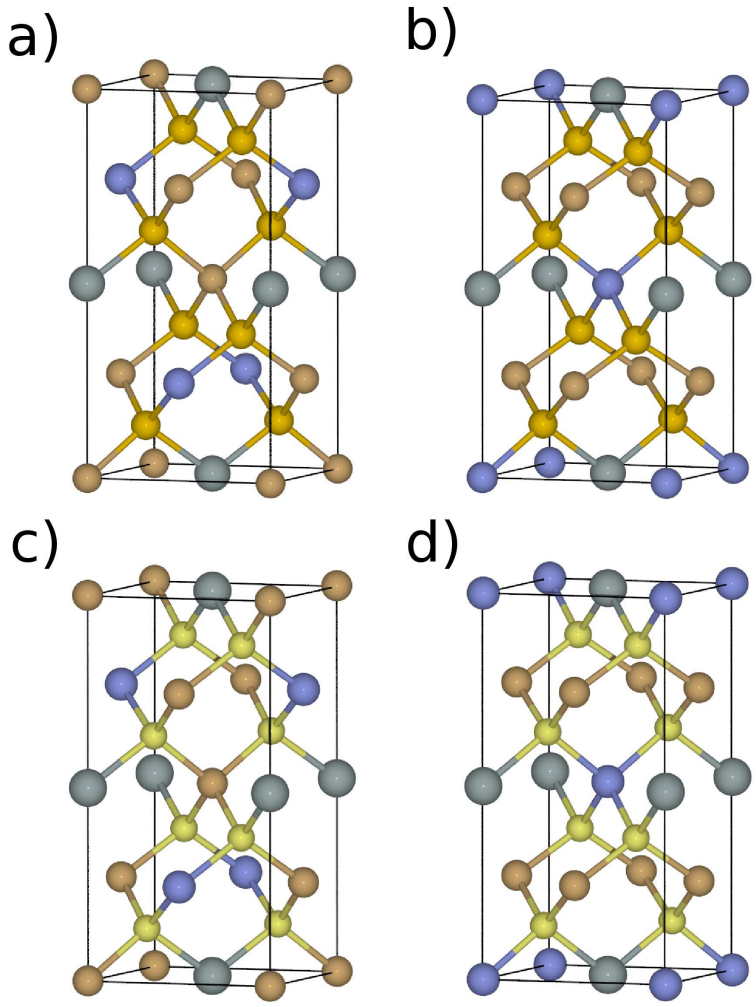

Figure 11.4: Unitcell for Cu_2ZnSnS_4 or $Cu_2ZnSnSe_4$ a) and c) kesterite ($I\bar{4}$) and b) and d) stannite ($I\bar{4}2m$) crystallographic structure. The differnt atoms are represented by the following colours: brown – Cu, grey – Zn, blue – Sn, orange – Se and yellow – S

11.3.2 Results

From the calculated structural optimization calculations the lowest total energy structure were obtained for both kesterite and stannite structures. The results are shown in the table 11.3.2. The difference between kesterite and stannite phase is 0.03eV for Cu_2ZnSnS_4 and 0.15 eV for $Cu_2ZnSnSe_4$ thus showing that the Se based compound is much less likely to have phase mixing than the S based one.

Cu_2ZnSnS_4			
	Kesterite	Stannite	
	Theory	Theory	Experimental [194]
Unit cell size			
a=b	5.48Å	5.47Å	5.427Å
c	10.91Å	10.95Å	10.87Å
c/2a	0.995	1.00	1.001
Bond lengths			
Se–Cu	2.35Å	2.34Å	
Se–Zn	2.36Å	2.43Å	
Se–Sn	2.42Å	2.38Å	
Energy	0.00eV	0.03eV	
$Cu_2ZnSnSe_4$			
	Kesterite	Stannite	
	Theory	Theory	Experimental [195]
Unit cell size			
a=b	5.78Å	5.85Å	5.688Å
c	11.56Å	11.34Å	11.338Å
c/2a	1.000Å	0.97Å	0.996Å
Bond lengths			
Se–Cu	2.44Å	2.464Å	
Se–Zn	2.50Å	2.52Å	
Se–Sn	2.63Å	2.58Å	
Energy	0.00eV	0.16eV	

Table 11.2: The structural characterization of kesterite and stannite structure for Cu_2ZnSnS_4 and $Cu_2ZnSnSe_4$ materials.

11.4 Grain boundaries

In comparison to the single crystalline structures with a long range periodicity in polycrystalline materials the periodicity is conserved only within the grains which in turn can give rise to quantum confinement of some states while conduction for other. The space between individual grains called the grain boundary (GB) is a transition between grains of a different orientation, different phase or even different composition. One of the significant challenges of thin-film technology is the full understanding of polycrystalline structures and a wide range of effects and mechanisms arising from it. One can easily see why the proper understanding of these interfaces is a necessary step for the understanding of the polycrystalline materials. The grain boundaries are known to be sinks for both defects and impurities, due to misalignments and a decreased coordination. One has to consider that some of the bonds of the interface atoms are not satisfied creating states often localized within the band gap. Considering the above one can see why production of single crystals which are free from any impurities, gaps, dislocation, and grain boundaries has been a goal in the production of high efficiency semiconductor devices. In the case of polycrystalline materials these studies become even more central with imperfections being a significant part of the the structure. In this case a skilful control over a GB is a way of defining the material property. This approach is known as of grain boundary engineering and has been proven so far to give improved mechanical and chemical properties of the materials [196]. According to the standard perspective the GBs in semiconductors are viewed as detrimental to the performance of electronic devices. In recent work on chalcopyrites, it has been shown that this may not always be the case and GBs in polycrystalline materials could actually play a beneficial role in the performance of photovoltaic devices [197, 198].

The interest in grain boundaries has undergone significant expansion in the last 30 years, with origins traceable back to the development of the first polycrystalline photovoltaics. At first the studies, due the experimental limitation, were mostly investigating such properties as resistivity, recombination efficiency, and I/V characteristics. With the development of more advanced experimental techniques, detailed studies of GB became possible. The major interest in the GB are physical processes like charge trapping and transport. Modelling of the realistic picture is however not straight forward with significant interface diversity and interplay of phenomena caused by a mixture of defects and impurities.

The thin films are produced in a variety of different methods. This

has a direct impact on the structures created and the characteristics of the grain boundaries present. The potential for many different morphologies and types of grain boundaries coexisting within the single sample makes both the experimental and theoretical work challenging.

One type of a grain boundry is a twin boundary. It is the incidence of highly symmetrical grain boundaries, it is prevalent in diamond-like semiconductors. Twin boundaries are of special interest in the structures analysed here. They represent the low energy boundaries with a minimal number of disrupted bonds. All others are more disrupted and chemically active, thus supporting chemical diffusion and electrical recombination and inhibiting or disrupting the transport over the boundary. Although the twinning relationship is fixed the interface plane between the grains is not, offering a few different boundary types. Since the twin boundaries are highly symmetrical they can be described by means of tilt, rotation shear or reflection. While in the case of small angle tilt boundaries the number of dislocations increases with increase of the angle, there are certain angles at which a lattice point of both sides of the boundary will be superimposed. Which in accordance to Coincidence Site Lattice (CSL) theory can be described by a ratio of points in the lattice to the number of points in CSL and is known as the Friedel index denoted by Σ. In the 1950's the CSL theory was applied extensively in the study by Kohn for the twin boundaries of diamond and then in late 1980's by Durose in the study of sphalerite [200, 201, 202]. The sphalerite orientation proposed by the model has been confirmed experimentally for CdTe [201, 203, 204]. As showed by Hold the mirror plane in sphalerite would lead to an energetically unfavourable boundary of an anti-phase orientation, this has been further extended in the recent work on the sphalerite and chalcopyrite where the CSL was used to identify the allowed twin boundaries [205]. One coherent and five incoherent boundaries were proposed while the coherent one was simulated in further work for a proposed chalcopyrite as well as structurally similar kesterite and stannite structures.

11.4.1 Experimental overview

The *CIGS* materials are a good example for thin–films to reach an efficiency competitive with the single crystalline material [206]. The process responsible for the unusually high efficiency has been debated for over a decade (for reviews of the subject see [198, 197]). The most accepted explanation has been proposed by Zunger and Persson. In their model the valence band bending would have been present due the neutral $2V_{Cu} + In_{Cu}$ defect states.

There the valence band offset is caused by the removal of Cu atoms from the boundary interface, leading to the formation of a neutral barrier for holes that prohibits the transport of electrons. This reduces the probability of recombination in the defected area. The proposed model was based on the formation of the grain boundary interface from two Cu deficient (112) polar surfaces. In such a way that the defects are localized along the two layers of a (112) interface between two crystal grains, where one grain is shifted with respect to the other by translation $\mathbf{t}$=0.5$\mathbf{b}$. The formation of this type of defect would also agree with the fact that the highest efficiency cells were always produced from Cu deficient materials [85, 207]. The existence of the proposed $2V_{Cu} + In_{Cu}$ defect complex has recently been been confirmed by experimental studies which have shown that the GB composition is in fact Cu deficient and In rich while the grain interior stays unchanged [208]. From high-resolution scanning transmission electron microscopy (HR-STEM) experiments three types of the (112) twin boundary have been distinguished and are presented in Fig. 11.5.

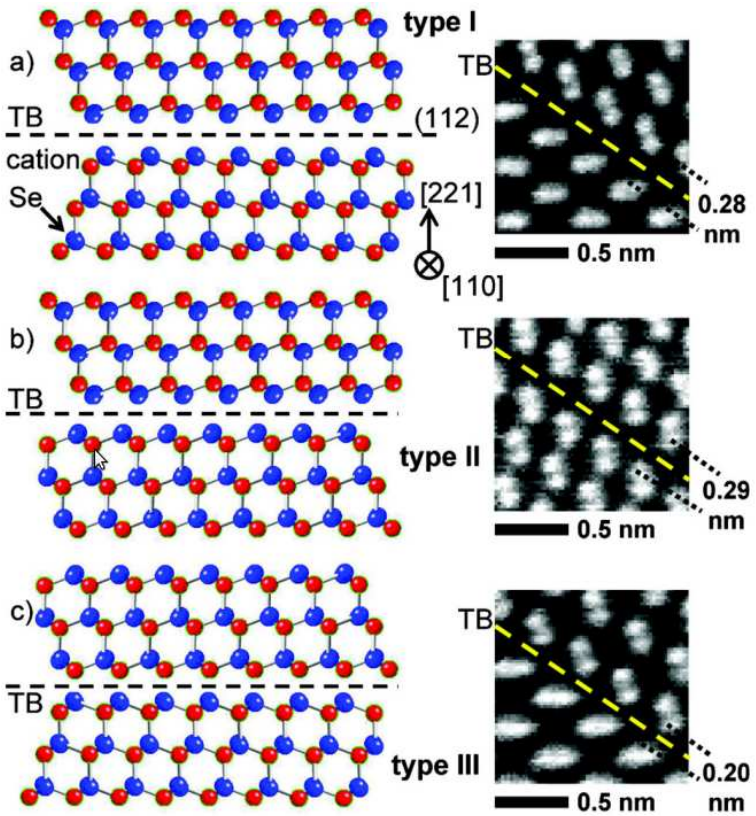

Figure 11.5: Structural representation of twin–boundaries and their corresponding high resolution high resolution transition microscope and electron energy–loss spectrometry of three types of GB identified in the studies performed by Abou–Ras *et al.* [208].

Type I and **Type II** GB have been identified as $Se - Se$ terminated lattice planes with the approximate distance between the planes of 2.8 Å and 2.9 Å respectively. For both of them a Cu depletion and In enrichment has been observed in comparison to the GB interior. **Type III** have been identified as Se–cation terminated lattice planes with the approximate distance between the planes of 2.0 Å. In this case no significant In enrichment but a slight Cu depletion was also observed.

It has has been found that the region of the compositional changes is very close to the twin boundary plain, ranging in width around 7.0–8.0 Å and 8.0–9.0 Å for I and II which correlates well with the thickness of two atomic planes.

It has been published on few occasions that the variation of a $Cu/(In + Ga)$ ratio is responsible for the variation in grain size [209, 210, 211], similarly to when the ratio of $Cu/(Zn, Sn)$ is varied for $CZTS$ absorbers [212, 213, 214]. On the basis of a series of measurements of random boundaries, Cu and In signals are always anti-correlated which is also strong evidence that site exchange In_{Cu}^{2+} and Cu_{In}^{2-} could be the origin for such hole barrier and increased efficiency [208]. Although there is a strong correlation between the proposed theoretical and the experimental composition of the boundary this can not be said about the structures proposed. Comparing Figures 11.5 (experimental GBs) and 11.6b (the theoretical GB proposed by Zunger) it can be seen that no satisfactory match can be made. Firstly the type I and II GB are characterized by $Se - Se$ bonding in experiments and Se–cation in theory, which is also reflected in the difference in the GB width. Secondly the characteristic atomic alignment (blue line in Fig. 11.6b) also differs, for experimental GB type I the atomic lines form a shifted mirrored structure while type II forms shifted in line structure. In contrast to the theoretical model the atoms in the bottom and top halfes of the interface are in line (blue line Fig. 11.6b). These differences prove that GB studies do not yet amount to a fully comprehensive model for $CIGS$ polycrystalline materials.

Investigations of the $CZTS$ grain boundary so far have shown two types of scenario: one with a Cu rich grain boundary and a width of about 50Å, while the other remains unchanged from the bulk composition [215, 216]. The studies of GB in $CZTS$ have just begun and have not been widely discussed in the literature yet. In recent theoretical studies, based on the grain boundary models derived from studies of $CdTe$, Li *et al.* compared $CIGS$ and $CZTS$ grain boundaries for a (114) plane GB. They have found that in this particular type of GB, dangling bonds are present, which in

the $Cu_2ZnSnSe_4$ create more defect levels within the band gap than in $CuInSe_2$. These would be expected to promote more electron–hole recombination and decrease the overall performance of the solar-cell.

11.4.2 Computational setting

The calculations have been performed using unit cells relaxed earlier from which the larger grain boundaries unit cells were created. The GB unit cells have been relaxed in the **z** direction to account for the different stacking present in the two GB (one at the middle of the cell and one at the cell boundary). In order to create a cell in which the interaction between the parallel boundaries are limited the cell grain interior consist of nine bilayers (see Fig. 11.6 and Fig. 11.7). The unit cell contains 144 atoms conserving the bulk stoichiometry. The unit cell dimensions are 8.33/7.22/61.25 Å for $CuInSe_2$, 8.16/7.07/59.97 Å and 8.16/7.06/59.97 Å for $Cu_2ZnSnSe_4$ kesterite and stannite, 7.74/6.70/56.88 Å and 7.73/6.70/56.87 Å for Cu_2ZnSnS_4 kesterite and stannite respectively. The k-point sampling has been made with $5\times5\times3$ grid. The calculations have been made with the PBE-PAW potentials with an energy cut off 300 eV. The relaxations have been performed until the force exerted on the atom was smaller the 0.01 eV/Å.

11.4.3 Theory and results

In this section, a coherent twin boundary within the (112) plane has been considered for both $CuInSe_2$ and the $CZTS$ group of materials. This type of boundary is also present in sphalerite as a (111) twin boundary. This is not the case however for chalcoparates in which the anti-site occupancy of the lattice is present for one in two of the CSL metal columns. In this case the grain boundary created has a slightly different ordering than the grain (presented in the Fig. 11.6) where for each Se atom there are two Cu and two In atoms. It has for every four Se atoms two are coordinated by $3Cu + 1In$ and $3In + 1Cu$ atoms and the two by $2Cu + 2In$ as for the bulk material. This type of boundary has been chosen to model the type III boundary observed by Abou–Ras *et al.*(see Fig. 11.5).

Similarly as for the chalcopyrates the same structure of the boundary would be expected in the kesterite or stannite materials which have also been investigated in this section. For the kesterites, the variation in the coordination similarly to the CIGS, creates different coordinations of the anions at the grain boundary where for every four Se or S anions there are $3Cu + Zn$ and $Cu + 2Zn + Sn$ or for the opposite boundary orientation

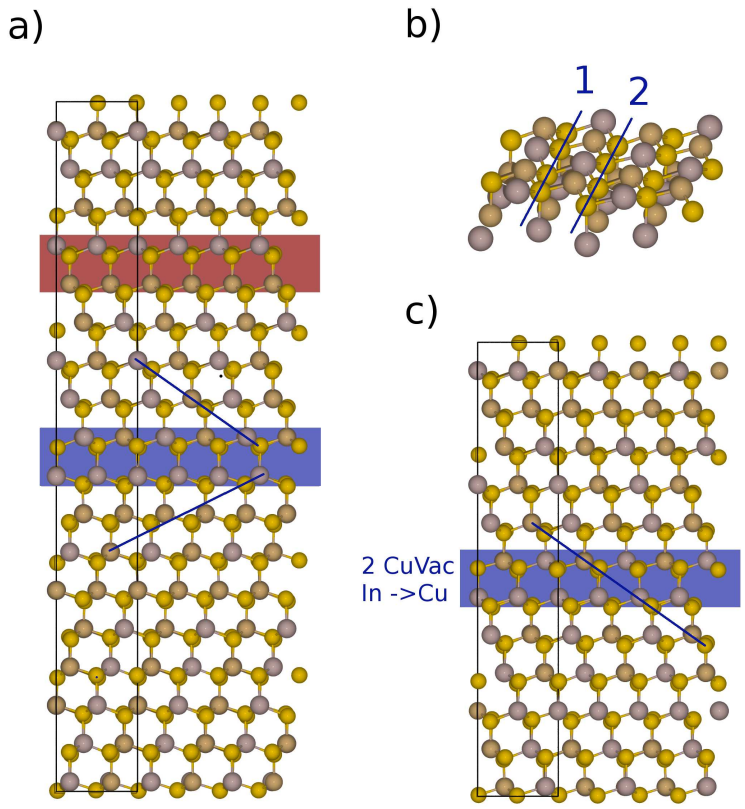

Figure 11.6: Unit cell for $CuInSe_2$ chalcopyrate grain boundaries. The a) panel presents the (112) twin boundary as proposed by the CSL model by Durose, the grain boundary is highlighted in blue while the grain interior used in text as reference atoms are highlighted in red. The blue lines represent the distinct atomic alignment. The panel b) the side tiled view of the boundary highlighted in blue color in a) is shown. The blue line no. 1 highlights the Se atoms with their usual coordination $2Cu+2In$ atoms per Se, while the blue line no. 2 highlights the atoms with grain boundary specific coordination $3Cu + In$ and $3In + Cu$ per Se atom. The plane c) present the modelled (112) boundary proposed as discused in text. The blue square highlights the boundary while the line represents the distinct atomic alignment.

$3Cu + Sn$ and $Cu + 2Sn + Zn$. In the case of stannites the GB ordering is slightly different: for every four Se atoms, two are coordinated by $2Cu + Zn + Sn$ and the other two by $2Cu + 2Zn$ and $2Cu + 2Sn$.

Because this type of boundary does not have any defect or dangling bonds, no trapped defect states are expected to be present within the band gap [217, 218]. In order to analyse the difference in the electronic structure at the grain boundary in comparison to the interior the LDOS for the grain boundary layer and a bulk layer have been obtained using the atoms as

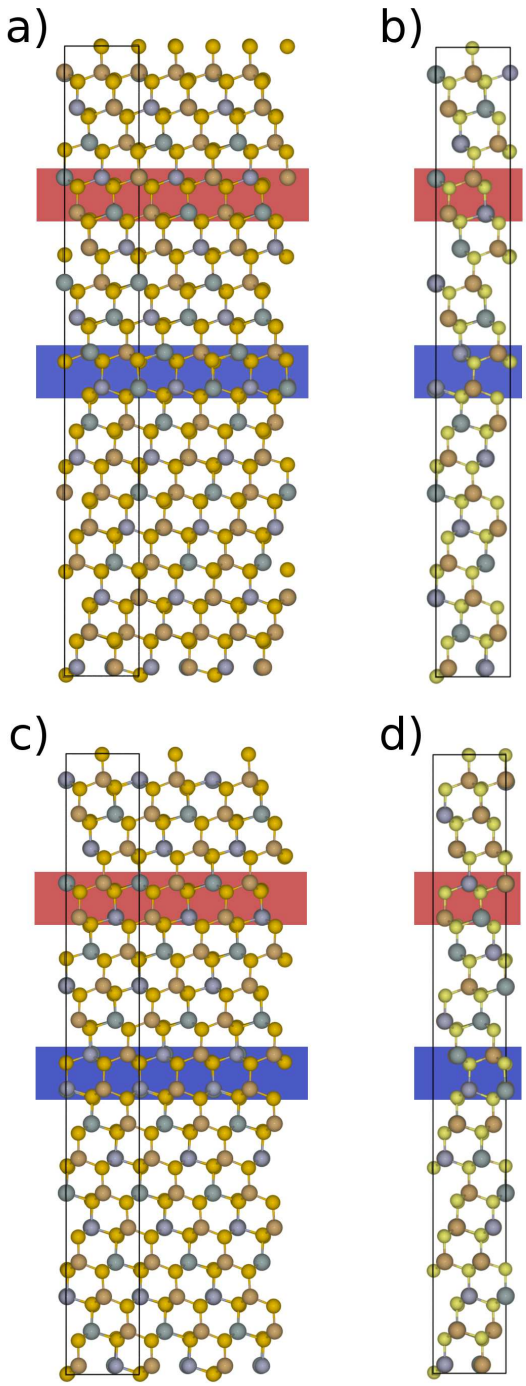

Figure 11.7: Unitcell of (112) plain grain boundary based on the CSL chalcopyrate grain boundary model. The panel a) and b) presents GB of kesterite, while c) and d) stannite type structures for $Cu_2ZnSnSe_4$ and Cu_2ZnSnS_4. The grain boundary is highlighted in blue while the grain interior used as reference atoms are highlighted in red.

highlighted in blue and red in Fig. 11.6a and Fig. 11.7.

The results of this study are shown at Fig. 11.7. Here, the band gap is

underestimated, therefore an additional $1.0 - 1.5$ eV (depending on the material) would have to be added to fit experimental band gaps. More accurate band gap calculations can be obtained with a higher level approximation such GGA+U or for hybrid functional HSE03, however this has been extensively studied in the literature [219, 185]. For the PV application the photon energy is in the range $1.2 - 3$ eV. As shown in the Fig. 11.8 there is an observable shift of the occupied LDOS closer to the Fermi level for both chalcopyrate and kesterite materials which is due to the switch in the Cu coordination of Se where the additional peak in the occupied states is caused by d–states of Cu atoms. The slight shift toward the Fermi level is larger in kesterites than in CuInSe2. For the stannite structure the LDOS is unchanged by the change in coordination from $2Cu+Zn+Sn$ to $2Cu+2Zn$, while $2Cu+2Sn$ had no significant impact on the electronic structure of the GB. The same characteristics are observed independent of the anion type, Se or S. In the Fig. 11.9, the total LDOS are shown for each atom. They reveal that the majority of the occupied states around the Fermi level are Cu states, while Se, In and Sn are largely unoccupied. The Zn states do not participate in the electronic structure close to the Fermi level.

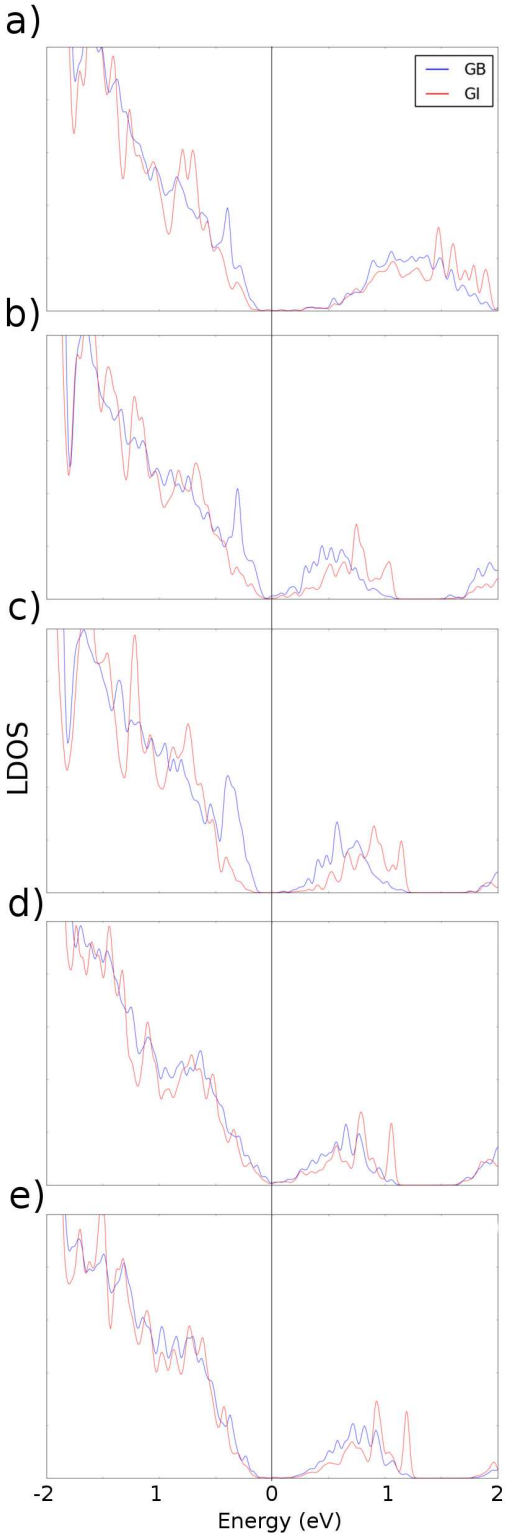

Figure 11.8: The comparison of LDOS projected on the grain boundary atoms and the grain interior atoms highlighted by blue and red squares in a) of fig. 11.6 and in fig. 11.7: a) $CuInSe_2$–chalcopyrate, b) $CuZnSnSe_4$–kesterite, c) $CuZnSnS_4$–kesterite, d) $CuZnSnSe_4$–stannite, e) $CuZnSnS_4$–stannite.

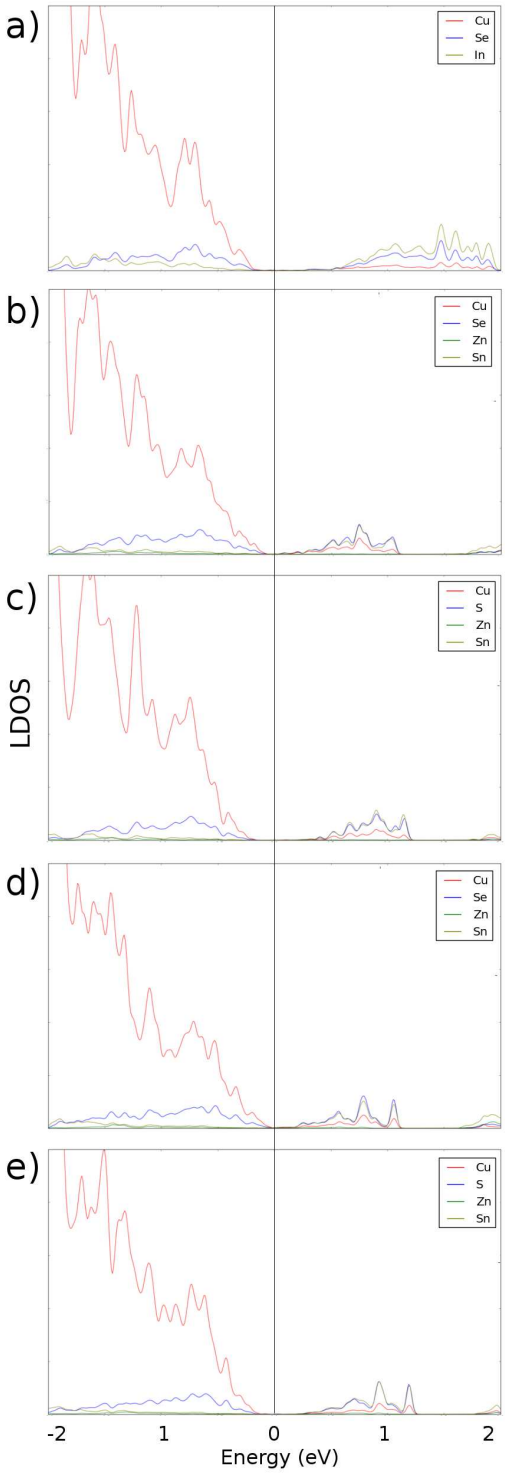

Figure 11.9: The comparison of LDOS projected on different atomic species: a) $CuInSe_2$–chalcopyrate, b) $CuZnSnSe_4$–kesterite, c) $CuZnSnS_4$–kesterite, d) $CuZnSnSe_4$–stannite, e) $CuZnSnS_4$–stannite.

11.5 Summary

The (112) twin grain boundary has been simulated for $CuInSe_2$ chalcopyrate and $CuZnSnSe_4$, $CuZnSnSe_4$ both kesterite and stannite materials. This boundary agrees well with one of the experimentally observed GB types for $CuInSe_2$ and is also expected to be present in the $CZTS$ materials. It has been found that this grain boundary in comparison to the grain interior has minor differences in the electronic structure. For the stannite materials no change has been observed, therefore the GB in this defect free state is expected to be inactive. For chalcopyrate and even more so for kesterite a shift of states towards the Fermi level was observed, it is expected that this could have just a small effect on the photovoltaic performance in specimens with high GB density.

It is predicted by Zhang *et al.* that the most important recombination defect due to its low formation energy and being located 0.34 eV below the conduction band minimum is In_{Cu}. It is, however, also predicted that this defect would be passivated relatively often due to the formation of the defect complexes $2V_{Cu} + In_Cu$ [14]. In future studies of this boundary the stability of the $2V_{Cu} + In_{Cu}$ complex relative to the grain interior should be considered as well as the V_{Cu} which is the lowest energy defect in CIS, while alternatively for $CZTS$ there is a larger group of low energy defects. In kesterites there are five low formation energy defects from which V_{Cu} is in second place after Cu_{Zn}, then there is additionally Zn_{Sn}, V_{Zn} and Cu_{Sn}. The GB localization of these defects should be studied which could lead to some interesting results and could more significantly affect the conductive characteristics of the boundary [14, 220].

Chapter 12

Final summary: Closing remarks

This thesis includes a broad range of simulations. The work started with the analysis of molecular adsorption on silicon, a wide variety of molecules adsorbed in varying levels of coverage, it touched the dynamics of diffusion of molecules along this surface in one instance, and it focussed on inter-molecular interactions and conformation changes due to polar interactions. This part of the work was driven to a large extent by existing experimental data and was the core task of my work in a collaboration with a group in Toronto.

The last part of the work, which analysed the electronic properties of semiconductors at grain boundaries, arose out of a particular situation during my PhD, the setup of a new institute for renewable energy with an emphasis on photovoltaics, and discussions with the group of Prof. Ken Durose on the importance of grain boundaries for photovoltaic efficiencies. As each individual chapter contained sections discussing the results and summarizing the main conclusions, I only wish to highlight the main achievements of this thesis in the closing remarks. These are, in my view:

- **Analysis of surface pinning:** Here we found that asymmetric pinning can be a valuable tool to identify the geometry of the adsorbate. In situations where STM profiles do not yield a clear identification of the molecule, calculations of relative adsorption energies and pinning can offer an alternative route.

- **Inter molecule interactions on Si(111):** Here we found that only simulations including dispersion interactions could correctly predict the preferred adsorption sites. The subsequent increase in precision

and size of the calculated system, which was performed after this work was concluded, established that surface mediated interactions via subsurface charge transfer is the decisive ingredient

- **Adsorption of small molecules of Si(100):** We find that the double-dimer bond configuration is the most favourable, and that the inclusion of vdW interactions improves the agreement between experimental and theoretical adsorption energies. Activation barriers for the conversion between single-dimer and double-dimer adsorption for benzene are within the range of established values, but 200meV too small compared to experiments.

- **High coverage benzene:** Here, the surface mediated interactions in this regime play only a limited role. Activation barriers are largely unaffected by coverage and no significant steric hindrance is observed.

- **Dynamics of diffusion:** In the study of ethylene on Si(100) we found that asymmetric desorption and residual torques on the molecules are probably the main cause of the very large diffusion lengths observed.

- **Grain boundaries in photovoltaic materials**: In the study of (112) twin boundaries the model proposed by experimenters has been validated by its total energy. It was also found that the anion coordination at the grain boundary of chalcopyrite and kesterite is the main driver for an increase of the LDOS near the bandgap. From a device point of view this indicates that such grain boundaries have only a minor effect on the efficiency of such solar cells.

It goes without saying that work, in particular in the last field, is still incomplete and one would wish that it could be continued with a prospect of a full understanding of functioning molecular electronics and photovoltaic devices.

Chapter 13

Additional material

13.1 Appendix I : Feynman-Hellmann theorem

Once the ground state of the system is reached through a self–consistent iteration cycle, KS orbitals can be used to determine the properties of the system. They can also be used to calculate the net force experienced by the ions in a not fully relaxed atomic arrangement. The calculation of the forces is the end step of the self–consistent DFT cycle at which the calculated force is used in the process of static minimization or molecular dynamic. As described earlier, this approach is possible due to BO approximation (see Secition 2.2.1). In VASP, the ionic forces are determined on the basis of Feynman-Hellmann theorem, i.e. the forces experienced by the ions are defined as the derivative of the generalized free energy. The functional F depends on the KS orbitals ϕ, the partial occupancies and the ionic positions $\mathbf{r}$. The set of the orbitals is denoted Φ and the set of partial occupancies as f. The electronic ground state is defined by the variational properties of the free energy

$$0 = \delta F[\Phi, f, R] \tag{13.1}$$

for an arbitrary variation of the equation it can be written as

$$\frac{\partial F}{\partial \Phi}\delta\phi + \frac{\partial F}{\partial f}\delta f = 0. \tag{13.2}$$

For arbitrary variation this is true only if both of the partial derivatives are equal to zero leading to the system of equations which determines Φ and f at the electronic ground state.

$$Force = \frac{dF[\Phi, f, R]}{dR} = \frac{\partial F}{\partial \Phi}\frac{\partial \Phi}{\partial R} + \frac{\partial F}{\partial f}\frac{\partial f}{\partial R} + \frac{\partial F}{\partial R} \tag{13.3}$$

where at the ground state the first two terms are equal to zero thus simplifying the equation to,

$$Force = \frac{dF[\Phi, f, R]}{dR} = \frac{\partial F}{\partial R} \tag{13.4}$$

The force is obtained by calculating the partial derivative of the free energy while keeping the wavefunction and the partial occupancies fixed at their respective ground state values.

13.2 Appendix II : Nudged elastic band

Common questions considering reactions, whether they are in the gas phase or on a surface, are the process of bonding, the transition between starting and final configuration, and the energy necessary to allow for the transition. The nudged elastic band method is one of the techniques dealing with these issues. In its application it is concerned with determining the minimum energy path (MEP) of the reaction. In the nudged elastic band (NEB) method a chain of intermediate positions is generated between two stable configurations (before and after reaction). The generated sets of coordinates are then updated in accordance to the first derivative of energy, the minimum energy path crosses the saddle points defining the transition barrier.

Henkelman and Jónsson in Ref. [25] proposed a method for the search of saddle points, that is, transition states, and minimum energy paths (MEP) between known reactants and products. The method requires no prior knowledge of the transition state as it works by optimizing a number of intermediate images, initially chosen as appropriate guesses (typically, by linear interpolation of the coordinates between the initial and the final state), along the reaction path. Each image converges to the lowest possible energy while maintaining equal spacing to neighbouring images. This constrained optimization is achieved by adding spring forces along the band between images and by projecting out the component of the force due to the potential perpendicular to the band. An elastic band with N+1 images can be denoted by $\{\mathbf{R_0}, \mathbf{R_1} ... \mathbf{R_N}\}$ where $\mathbf{R_0}$ and $\mathbf{R_N}$ are fixed (initial and final state). The total force acting on an image is:

$$\mathbf{F_i} = \mathbf{F_i^s} \mid_{\parallel} -\nabla \mathrm{E}(\mathbf{R_i}) \mid_{\perp} \tag{13.5}$$

where

$$\mathbf{F_i^s} \mid_{\parallel} = k(\mid \mathbf{R_{i+1}} - \mathbf{R_i} \mid - \mid \mathbf{R_i} - \mathbf{R_{i-1}} \mid) \tag{13.6}$$

and

$$\nabla E(\mathbf{R_i}) \mid_{\perp} = \nabla E(\mathbf{R_i}) - \nabla E(\mathbf{R_i}) \cdot \hat{\tau}_i \tag{13.7}$$

where k is the spring constant and $\hat{\tau}_i$ is the tangent unit vector at image i.

The Climbing Image NEB or CI–NEB [26] is an improvement of the NEB method, within which, after a few iterations, the image $\mathrm{i_{max}}$ with the highest energy is identified as the transition state and hence driven up to the saddle point by maximizing its energy along the band while minimizing it in all other directions. When this image converges, it will be at the exact saddle point. The force on this image is not given by Eqn. (13.5) but by

$$\mathbf{F_{i_{max}}} = -\nabla \mathrm{E}(\mathbf{R_{i_{max}}}) + 2\nabla \mathrm{E}(\mathbf{R_{i_{max}}}) \mid_{\parallel} , \tag{13.8}$$

that is, the image does not feel the spring forces along the band; instead, the true force acting upon this image along the tangent is inverted.

Bibliography

[1] P. Hohenberg and W. Kohn, Phys. Rev. **136**, B864 (1964).

[2] W. Kohn and L. J. Sham, Phys. Rev. **140**, A1133 (1965).

[3] M. Levy, Proc. Natl. Acad. Sci. USA **76**, 6062 (1979).

[4] E. Lieb, Intl. Jour. Quant. Chem. **24**, 243 (1983).

[5] Richard M. Martin *Electronic Structure*, Cambridge University Press, Cambridge UK (2004).

[6] A.D. Becke, J. Chem. Phys. **98**, 5648 (1993).

[7] C. Lee, W. Yang, R.G. Parr, Phys. Rev. B **37**, 785 (1988).

[8] J. P. Perdew and A. Zunger, Phys. Rev. B, **23**, 5048 (1981).

[9] J. Heyd, G. E. Scuseria, and M. Ernzerhof, J. Chem. Phys. **118**, 8207 (2003).

[10] V. Krukau, O. A. Vydrov, A. F. Izmaylov, and G. E. Scuseria, J. Chem. Phys. **125**, 224106 (2006).

[11] J. P. Perdew, J. A. Chevary, S. H. Vosko, K. A. Jackson, M. R. Pederson, D. J. Singh, and C. Fiolhais, Phys. Rev. B, **46**, 6671 (1992).

[12] G. J. Laming, V. Termath, and N. Handy, J. Chem. Phys. **99**, 8765 (1993).

[13] J. P. Perdew, K. Burke, and M. Ernzerhof, Phys. Rev. Lett. **77**, 3865 (1996).

[14] Y. Zhang and W. Yang Phys. Rev. Lett. **80**, 890 (1998).

[15] B. Hammer, L.B. Hansen and J.K. Norskov, Phys. Rev. B **59**, 7413 (1999).

[16] A. E. Mattsson, P. A. Schultz, M. P. Desjarlais, T. R. Mattsson, and K. Leung. Modell. Simul. Mater. Sci. Eng. **13**, R1 (2005).

[17] D. C. Langreth, M. Dion, H. Rydberg, E. Schrader, P. Hyldgaard, and B. I. Lundqvist, Intl. J. Quant. Chem. **101**, 599 (2005).

[18] A. Gulans, M. J. Puska, and R. M. Nieminen, Phys. Rev. B **79**, 201105(R) (2009).

[19] J. Klimes, D. R. Bowler, and A. Michaelides, Phys. Rev. B **83**, 195131 (2011).

[20] S. Grimme, J. Comp. Chem. **27**, 1787 (2006).

[21] H. J. Monkhorst and J. D. Pack, Phys Rev B **13**, 5188 (1976).

[22] P. E. Blöchl, Phys. Rev. B **50**, 17953 (1994).

[23] G. Kresse and D. Joubert, Phys. Rev. B **59**, 1758 (1999).

[24] J. Gavnholt, T. Olsen, M. Engelund and J. Schiotz, Phys. Rev. B **78**, 075441 (2008).

[25] H. Jónsson, G. Mills and K. W. Jacobsen, *Classical and Quantum Dynamics in Condensed Phase Simulations*, Singapore, World Scientific (1998).

[26] G. Henkelman, B. P. Uberuega and H. Jonsson, J. Chem. Phys. **113**, 9901 (2000).

[27] $http://www.fhi-berlin.mpg.de/pc/IMAGE/resmethodpict\_STM.jpg$

[28] J. Tersoff and D.R. Hamann Phys. Rev. B. **50**, 25 (1983).

[29] J. Tersoff and D.R. Hamann Phys. Rev. B. **31**, 2 (1984).

[30] $https://www.vasp.at/$

[31] G. Kresse and J. Hafner, Phys. Rev. B **47**, 558 (1993).

[32] G. Kresse and J. Furthmüller, Phys. Rev. B **54**, 11169 (1996).

[33] $https://wiki.fysik.dtu.dk/gpaw/features\_and\_algorithms.html\_features-andalgorithms$

[34] $http://www.liv.ac.uk/whofer/stm/bskan\_guide.pdf$

[35] J. Dabrowski and H. J. Mussig, *Silicon Surfaces and Formation of interfaces*, Singapore, World Scientific (2000).

[36] A. Kara, H. Enriquez, A. P. Seitsonen, L. C. Lew Yan Voon, S. Vizzini, B. Aufray and H, Oughaddou, Surf. Sci. Rep. **67**, 1 (2012).

[37] R. Del Sole, L. Reining and R. W. Godby, Phys. Rev . B. **49**, 8024 (1994).

[38] A. Fleszar and W. Hanke W, Phys. Rev. B **56**, 10228 (1997).

[39] D. H. Riegier, L. Steinbeck, I. D. White, H. N. Rojas, and R. W. Godby, Comput. Phys. Commun. **117**, 211 (1999).

[40] D. H. Rich, T. Miller, G. E. Franklin and T. C. Chiang, Phys. Rev. B **39**, 1438 (1989).

[41] O. Madelung, New Series, Springer, **22a**, 14(6) (1987).

[42] K. Takayanaki, Y. Tanishiro, M. Takahashi, and S. Takahashi, J. Vac. Sci. Technol. **A3**, 1502 (1985).

[43] www.preview.omicron.de

[44] J. Dabrowski and M. Scheffler, Appl. Surf. Sci. **56**, 15 (1992).

[45] R. A. Wolkow, Phys. Rev. Lett. **68**, 2636 (1992).

[46] C. C. Fu, M. Weissmann, and A. Saul, Surf. Sci. **494**, 119 (2001).

[47] M. Z. Hossain, K. Mukai , Y. Yamashita, H. Kawai and J. Yoshinobu Chem. Commun **47**, 10392 (2011).

[48] G. A. D Briggs, J. Knall, A. J. Mayne, T. S. Jones, W. H. Weinberg and A. R. Avery *Nanotechnology* **3** 113 (1992)

[49] H. F. Wilson, N. A. Marks, D. R. McKenzie, Surf. Sci. **587** 185, (2005).

[50] P. V. Smith, O. Warschkow, M. Radny, Steven R. Schofield and D. R. Belcher, J. Chem. Phys. **134** 064709 (2011).

[51] J. Wang, T. A. Arias, and J. D. Joannopoulos, Phys. Rev. B. **47**, 10497 (1993).

[52] S. R. Schoefield, N. J. Curson, J. L. O'Brien, M. Y. Simons, R. G. Clarck, N. A. Marks, H. F. Wilson, G. W. Brown, and M. E. Hawley, Phys. Rev. B **69**, 085312 (2004).

[53] Z. Zhang, M. A. Kulakov and B. Bullemer, Surf. Sci. **369**, L131 (1996).

[54] T. Uda, and K. Terakura, Phys. Rev. B. **53**, 6999 (1996).

[55] K. Hata, S. Ozawa and H, Shigekawa, Surf. Sci. **441**, 140 (1999).

[56] T. Miyazaki, T. Uda, and K. Terakura, Phys. Rev. Lett. **84**, 4128 (2000).

[57] M. Chander, Y. Z. Li, J. C. Patrin, and J. H. Weaver, Phys. Rev. B. **48**, 2493 (1993).

[58] O. Warschow, S. R. Schofield *et. al.* Phys. Rev. B **77**, 201305(R) (2008).

[59] P. Sobotik and I. Ostadal Surf. Sci. **604**, 237 (2010).

[60] J. Zikovsky, S. A. Dogel, M. Basser Haider, G. A. DiLabio, and R. A. Wolkow, J. Phys. Chem. A **111**, 12257 (2007).

[61] E. Pehlke and P. Kratzer Phys. Rev. B, **59**, 2790 (1999).

[62] M. Chandler, Y. Z. Li, J. C. Patrin and J.H. Weaver, Phys. Rev. B **48**, 2493 (1993).

[63] L. Andersohn and U. Kohler Surf. Sci. **284**, 77 (1993).

[64] S. Okano, and A. Oshiyama, Surf. Sci. **554**, 272 (2004).

[65] J. Y. Lee, and J. H. Cho, J. Phys. Chem. B **110**, 18455 (2006).

[66] R.Konecny and D. J. Doren J. Chem. Phys. **106**, 2426 (1997).

[67] R. Lelis-Sousa, and M. J. Caladas, AIP Conf. Proc. **1199**, 9 (2010).

[68] Z. K. Smedarchina and M. Z. Zgierski, Int. J. Mol. Sci. **4**, 445 (2003).

[69] S.-Y. Yu, Y-S Kim, H. Kim and J-Y. Koo *et. al.* J. Phys. Chem. C **115**, 24800 (2011).

[70] M. K. Weldon, B. B. Stefanov, K. Raghavachari and Y. J. Chabal Phys. Rev. Lett. **79**, 2851 (1997).

[71] I. Fernandez-Torrente, S. Mounturet, J. K. Franke, J. Fraxedas, N. Lorente, J. I. Pascal Phys. Rev. Lett. **99**, 176103(4) (2007).

[72] C. Stadler, S Hansen, I. Krøger, C. Kumpf, E Umbach Nat. Phys. **5**, 153 (2009).

[73] M. Sterrer, T. Risse, U. M. Pozzoni, L. Giordano, M. Heyde, H. P. Rust, G Pacchoni, H. J. Freund Phys. Rev Lett. **98**, 096107(4) (2007).

[74] T. Yokoyama, T. Takahashi, K. Shinozaki, M. Okamoto Phys Rev. Lett. **98**, 206102(4) (2007).

[75] Y. Nakamura, Y. Mera, K. Maeda. Phys. Rev. Lett. **89**, 266805(4) (2002).

[76] P. A. Sloan, S. Sakulsermsuk, R. E. Palmer Phys. Rev. Lett. **105**, 048301(4) (2010).

[77] A. Bellec, D. Riedel, G. Dujardin, O. Boudrioua, L. Chaput, L Stauffer, P. Sonnet Phys. Rev. Lett. **105**, 048302(4) (2010).

[78] Conversation and correspondence. (2010-2011).

[79] The presentation and discussion with Ian R. McNab (2011).

[80] G. Kresse and J. Furthmüller, Comput. Mater. Sci. **6**, 15 (1996).

[81] K. Tanabe, Spectrochem. Act **28A**, 407 (1972).

[82] M. Ebrahimi, K. Huang, X.K. Lu, I. R. McNab, J. C. Polanyi, Z. Wagar, J. S. Y. Yang, H. Lin and W. A. Hofer (2011) J. Am. Chem. Soc. **133**, 16560 (2011).

[83] G. A. Somorjai. Wiley 340–347, (1994).

[84] Briner, B. G., Doering, M., Rust, H. P. and Bradshaw, A. M. Science **278**, 257 (1997).

[85] C. Persson and A. Zunger, Phys. Rev. B **91**, 266401 (2003).

[86] T. Komeda, Y. Kim, M. Kawai, B. N. J. Persson and H. Ueba, Science **295**, 2055 (2002).

[87] J. I.Pascual, N. Lorente, Z. Song, H. Conrad and H.-P. Rust, Nature **423**, 525 (2003).

[88] L. Bartels, F. Wang, D. Moller, E. Knoesel and T. F. Heinz, Science **305**, 648 (2004).

[89] E. H. G. Backus, A. Eichler, A. W. Kleyn and M. Bonn, Science **310**, 1790 (2005).

[90] K. Stepan, J. Gudde and U. Hofer, Phys Rev. Lett. **94**, 236103 (2005).

[91] J. Gaudioso, H. J. Lee and W. Ho, J. Am. Chem. Soc. **121**, 8479 (1999).

[92] D.Riedel, J. Am. Chem. Soc. **131**, 5414 (2009).

[93] D. Riedel, J. Am. Chem. Soc. **131**, 7344 (2009).

[94] B. R. Trenhaile, V. N. Antonov, G. J. Xu, Abhishek Agrawal, A. W. Signor, R. E. Butera, Koji S. Nakayama, and J. H. Weaver Phys. Rev. B **73**, 125318 (2006).

[95] A. J. Mayne, G. Dujardin, G. Comtet and D. Riedel, Chem. Rev. **106**, 4355 (2006).

[96] J. V. Barth, Surf. Sci. Rep. **40**, 75 (2000).

[97] G. Ertl, Wiley 60–64 (2009).

[98] L. Clemen, Surf. Sci. **268**, 205 (1992).

[99] K. R. Harikumar, I. R. McNab, J. C. Polanyi, H. Lin and W. A. Hofer, Nature Chemistry **1**, 716 (2009).

[100] H. Liu, and R. J. Hamers, J. Am. Chem. Soc. **119**,7593 (1997).

[101] M. Shimomura, Surf. Sci. **504**, 19 (2002).

[102] M.J. Nagao, Am. Chem. Soc. **126**, 9922 (2004).

[103] C.-H. Chung, , W.-J. Jung, and I.-W. Lyo, Phys. Rev. Lett. **97**, 116102 (2006).

[104] Q. J. Zhang, X. L. Fan, W. M. Lau and Z.-F. Liu, Phys. Rev. B **79**, 195303 (2009).

[105] P. M. Ryan, L. C. Teague and J. J. Boland, J. Am. Chem. Soc. **131**, 6768 (2009).

[106] K. R. Harikumar, J. C. Polanyi, A. Zabet-Khosousi, P. Czekala , H. Lin and W. A. Hofer Nature Chem. **3**, 400 (2011).

[107] J. Paier, R. Hirschl, M. Marsman and G. Kresse, J. Chem. Phys. **122**, 234102 (2005).

[108] G. Comtet and G. Dujardin, J. Phys. Condens. Matte **18**, S1777 (2006).

[109] L. Grill, K.-H. Rieder, F. Moresco, G. Rapenne, S. Stojkovic, X. Bouju and C. Joachim Nature Nanotech **2**, 95 (2007).

[110] R. A. Wolkow. Annu. Rev. Chem. **50**, 413 (1999).

[111] A. J. Fisher, P. E. Blochl, and G. A. D. Briggs. Surf. Sci. **374**, 298 (1997).

[112] R. Terborg, P. Baumgärtel, R. Lindsay, O. Schaff, T. Gießel, J. T. Hoeft, M. Polcik, R. L. Toomes, S. Kulkarni, A. M. Bradshaw, and D. P. Woodruff. Phys. Rev. B, **61** 16697 (2000).

[113] S. H. Xu, M. Keeffe, Y. Yang, C. Chen, M. Yu, G. J. Lapeyre, E. Rotenberg, J. Denlinger, and J. T. Yates. Phys. Rev. Lett. **84**, 939 (2000).

[114] Y. Morikawa. Phys. Rev. B **63**, 033405 (2001).

[115] W. A. Hofer, A. J. Fisher, and R. A. Wolkow. Surf. Sci. **475**, 83, 3/10 (2001).

[116] J.-H. Cho and L. Kleinman. Phys. Rev. B, **69** 075303, (2004).

[117] L. Li, C. Tindall, O. Takaoka, Y. Hasegawa, and T. Sakurai. Phys. Rev. B, **56**, 4648 (1997).

[118] W. Kim, H. Kim, G. Lee, Y.-K. Hong, K. Lee, Chanyong, Hwang, D.-H. Kim, and J.-Y. Koo. Phys. Rev. B, **64**, 193313, (2001).

[119] D. C. Sorescu and K. D. Jordan. J. Phys. Chem. B, **104**, 8259, (2000).

[120] S. Mezhenny, I. Lyubinetsky, W. J. Choyke, R. A. Wolkow, and J. T. Yates. Chem. Phys. Lett., **344**, 7–12, 8/17 (2001).

[121] P. L. Silvestrelli, O. Pulci, M. Palummo, R. Del Sole, and F. Ancilotto. Phys. Rev. B, **68**, 2353061–2353065 (2003).

[122] W. A. Hofer, A. J. Fisher, G. P. Lopinski and R. A. Wolkow, Surf. Sci. **482-485**, 1181 (2001).

[123] F. Wang, D. C. Sorescu, and K. D. Jordan. J. Phys. Chem. B, **106**, 1316 (2002).

[124] W. Ji, L. A. Zotti, H.-J. Gao, and W. A. Hofer. Phys. Rev. Lett. **104**, 099703 (2010).

[125] X. Lu and M. C. Lin. Phys. Chem. Chem. Phys. **2**, 4213 (2000).

[126] M. Dion, H. Rydberg, E. Schrader, D. C. Langreth, and B. I. Lundqvist. Phys. Rev. Lett., **92**, 246401 (2004).

[127] M. Dion, H. Rydberg, E. Schrader, D. C. Langreth, and B. I. Lundqvist. Phys. Rev. Lett., **95**, 1 (2005).

[128] M. Hortamani, P. Kratzer, and M. Scheffler, Phys. Rev. B **76**, 235426 (2007).

[129] F. Hanke. J. Comput. Chem. **32**, 1424 (2011).

[130] J. Tersoff and D. R. Hamann. Phys. Rev. B, **31**, 805 (1985).

[131] J. Tersoff. Phys. Rev. B **37**, 6991 (1988).

[132] K. R. Harikumar, I. R. McNab, J. C. Polanyi, A. Zabet–Khosousi, C. Panosetti and W. A. Hofer, Chem. Commun. **47**, 12101 (2011).

[133] Y. Taguchi, M. Fujisawa, T. Takaoka, T. Okada and M. Nishijima, J. Chem. Phys. **95**, 6870 (1991).

[134] M. J. Kong, A. V. Teplyakov, J. G. Lyubovitsky and S. F. Bent, Surf. Sci. **411**, 286 (1998).

[135] H. D. Jeong, S. Ryu, Y. S. Lee and S. Kim, Surf. Sci. Lett. **344**, L1226 (1995).

[136] R. A. Wolkow, G. P. Lopinsi and D. J. Moffatt, Surf. Sci., **416**, L1107 (1998).

[137] W. A. Hofer, A. J. Fisher, G. P. Lopinski and R. A. Wolkow, Phys. Rev. B, **63**, 085314 (2001).

[138] Y. Jung and M. S. Gordon, J. Am. Chem. Soc., **127**, 3131 (2005).

[139] J. Lee and J. Cho, Phys. Rev. B **72**, 235317 (2005).

[140] K. Johnston, J. Kleis, B. I. Lundqvist and R. M. Nieminen, Phys. Rev. B, **77**, 121404 (2008).

[141] K. Johnston, J. Kleis, B. I. Lundqvist and R. M. Nieminen, Phys. Rev. B, **77**, 209904(E) (2008).

[142] B. I. Craig. Surf. Sci. Lett., **280**, L270 (1993).

[143] G. P. Lopinski, T. M. Fortier, D. J. Moffatt, and R. A. Wolkow, J. Vac. Sci. Technol. A, **16**, 1037 (1998).

[144] K. R. Harikumar, J. C. Polanyi, A. Zabet-Khousousi, Surf. Sci. **606**, 1431 (2012).

[145] S. C. Oh, K. W. Kim, A. H. Mamun, Ha-Jin Lee and J. R. Hahn, Bull. Korean Chem. Soc. **31**, 1 (2010).

[146] G. Nisbet, C. L. A. Lamont, M. Polcik, R. Terborg, D. I. Sayago, M. Kittel, J. T. Hoeft, R. L. Toomes and D. P. Woodruff, J. Phys: Condens. Matter **20**, 304206 (2008).

[147] S. Tsuzuki and H. P. Luethi, J. Chem. Phys. **114**, 3949 (2001).

[148] M. Allen and D. J. Tozer, J. Chem. Phys. **117**, 11113 (2002)

[149] U. Zimmerli, M. Parrinello and P. Koumoutsakos, J. Chem. Phys. **120**, 2693 (2004).

[150] K. H. Bevan, F. Zahid, D. Kienle and H. Guo, Phys. Rev. B **76**, 045325 (2007).

[151] J. M. Soler et al., Phys. Condens. Matter. **14**, 2745 (2002).

[152] W. Tang, E. Sanville, and G. Henkelman , J. Phys.: Condens. Matter **21**, 084204 (2009).

[153] B. Borovsky, M. Krueger and E. Ganz, Phys. Rev. B **57**, 4269 (1998).

[154] G. P. Lopinski, D. J. Moffatt and R. A. Wolkow, Chem. Phys. Lett. **282**, 305 (1998).

[155] K. Johnston and R. M. Nieminen, Phys. Rev. B **76**, 085402 (2007).

[156] P. L. Silvestrelli, F. Ancilotto and F. Tiogo, Phys. Rev. B **62**, 1596 (2000).

[157] H.–J. Kim, A. Tkatchenko, J. H. Cho and M. Scheffler, Phys. Rev. B **85**, 041403(R) (2012).

[158] E. Wigner, Trans. Faraday Soc. **34**, 29 (1938).

[159] E. Wigner, Z. Phys. Chem. Abt. B **19**, 203 (1932).

[160] H. Jónsson, *P Natl Acad Sci*, **108**, 944 (2011).

[161] P. T. Czekala, H. Lin, W. A. Hofer, A. Gulans, Surf. Sci. **605**, 1341 (2011).

[162] K. W. Self, R. I. Pelzel, J. H. G. Owen, and C. Yan, J. Vac. Sci. Technol. A, **16**, 1031 (1998).

[163] D. R. Belcher, M. W. Radny, S. R. Schoefield, P. W. Smith and O. Warschkow, J. Am. Chem. Soc. **134**, 15312 (2012).

[164] J. -J. Gallet, F. Bournel, F. Rochet, U. Kohler, S. Kubsky, M. G. Silly, F. Sirotti and D.Pierruci J. Phys. Chem. **115**, 7686 (2011).

[165] S.-Y. Yu, H. Kim and J.- Y. Koo Phys. Rev. Lett. **100**, 036107 (2008).

[166] Q. Goa, Z Donhnalek, C. C. Cheng, W. J. Choyke and J. T. Yates Surf. Sci. **312**, 261 (1994).

[167] Md. Z. Hossain, H. S. Kato, and M. Kawai, J. Am. Chem. Soc. **129**, 12304 (2007).

[168] G. P. Lopinski, D. D. M Wayner, R. A. Wolkow, Nature *406*, 6791, 48 (2000).

[169] R. Basu, N. P. Guisinger, M. C. Hersam, Appl. Phys. Lett. **85**, 2619 (2004).

[170] P. Kruse, E. R. Johnson, G. A. DiLabio, and R. A. Wolkow , Nano. Lett. **2**, 807(2002).

[171] J. L. Pitters, I. Dogel, G. A. DiLabio and R. A. Wolkow, J. Phys. Chem. B **110**, 2159 (2006).

[172] M. Z. Hossain, H. S. Kato, and M. Kawai, J. Phys.Chem. B **109**, 23129 (2005).

[173] M. Smeu, R. A. Wolkow, H. Guo, Theor Chem. Acc **131**, 1085 (2012).

[174] P. G. Piva, G. A. Dilabio, J. L. Pitters, J. Zilkovski, M. Rezeg, S. Dogel, Nature **435**, 658 (2005).

[175] Z. Shahan Clean Technica, (2013).

[176] K. Bucher, J. Burns, and H. G. Wagemann, J. Appl. Phys. **75**, 1125 (1994).

[177] $http://www.nrel.gov/ncpv/images/efficiency_chart.jpg$

[178] B. S. Richards, Prog. Photovolt. Res. Appl. **13**, 173 (2005).

[179] M. Powalla and B. Dimmler Sol. Mat. Energy Sol. Cells **67**, 337 (2001).

[180] M. A. Green Prog. Phot. Res. App . **17**, 347 (2009).

[181] www.fastmarkets.com , (2013).

[182] T. K. Todorov, K. B. Reuter, D. B. Mitzi, Adv. Mater. Sci. **22**, 1 (2010).

[183] S-.H. Wei, S. B. Zhang, and A. Zunger Phys. Rev. B **59**, R2478 (1999).

[184] J. Parkes, R. D. Tomlinson and M. J. Hampshire, J. Appl. Crystallogr. **6**, 514 (1973).

[185] J. Paier, R. Asahi, A.Nagoya, and G. Kresse, Phys. Rev. B **79**, 115126 (2009).

[186] C. Persson, J. Appl. Phys. **107**, 053710 (2010).

[187] S. Chen, X. G. Gong, A. Walsh, and Su-Huai Wei **94**, 041903 (2009).

[188] M. Ichimura, and. Y. Nakashima, Jpn. J. Appl. Phys. **48**, 090202 (2009).

[189] H. Katakgiri, K. Saitoh, T. Washio, H. Shinohara, T. Kurumandani and S. Miyajima, Sol. Energy Mater. Sol. Cells **65**, 141 (2001).

[190] N. Kamoun, H. Bouzouita and B. Rezig, Thin Solid Films **515**, 5949 (2007).

[191] N. Nakayama and K. Ito, Appl. Surf. Sci. **92**, 172 (2006).

[192] S. Ahn, S. Jung, J. Gwak, A. Cho, K. Shin, K. Yoon, D. Park, H. Cheong, and J. Ho Yun, Appl.Phys. Lett. **97**, 021905 (2010).

[193] S. Schorr, Sol. Energy Mater. Sol. Cells **95**, 1482 (2011).

[194] S. R. Hall, J. T. Szymanski and J. M. Stewart, Can. Mineral. **16**, 131 (1978).

[195] R. A. Wibowo, E. S. Lee, B. Munir and K. H. Kim Phys Status Solidi A**2004**, 3373 (2007).

[196] V. Randle, Mat. Sci. and Tech. **26**, 3 , 253 (2010).

[197] U. R. Rau, K Tarreto, S. Sibentritt Appl. Phys A **96**, 221 (2009).

[198] S. Siebentritt, M. Igalson, C. Persson, and S. Lany, Prog. Photovolt: Res. Appl. **18**, 390 (2010).

[199] D. Cahen, R. Noufi, Appl. Phys. Lett. **54**, 558 (1998).

[200] J. A. Kohn, Am. Minarologist **43**, 263 (1958).

[201] K. Durose and G. J. Russell, Inst. Phys. Conf. Ser.**No84**, (4)327 (1987).

[202] K. Durose and G. J. Russell, J. Crystal Growth. **101**, 246 (1989).

[203] K. Durose, G. J. Russell and J. Woods, Inst. Phys. Conf. Ser. **No76**, 233 (1985).

[204] K. Durose, Phd Thesis Structural defects in CdTe Durham University (1986).

[205] K. Durose, Mater. Res. Soc. Symp. Proc. **1012** Y09-02 (2007).

[206] P. Jackson, D. Hariskos, E. Lotter, S. Paetel, Wuerz, R. Renner, W. Wischmann and M. Powalla, Prog. Phot. Res. App. **19**, 894 (2011).

[207] M. J. Romero, K. Ramanathan, M. A. Contreras, M. M. Al-Jassim, R. Noufi and P. Sheldon App. Phys. Lett. **38**, 23 (2003).

[208] D. Abou-Ras, B. Schaffer, M. Schaffer, S.Schmidt, R.Caballero, and T. Unold, Phys. Rev. Lett. **108**, 075502 (2012).

[209] A. M. Gabor,F. R. Tuttle, D. S . Albin, M. A. Contreras and R. Noufi. Appl. Phys Lett. **65** (2), 198 (1994)

[210] R. A. Mickelsen, W. S. Chen, Y. R. Hsiao, V. E. Lowe, IEEE Transactions on Electron devices ED–31 (5), 543(1984).

[211] F. R. Tuttle, M. A Contreras, M. H. Bode, D. Niles, D. S. Albin, R. Matosn, A. M. Gabor, A. tennant, A. Duda, R Noufim, J. Appl. Phys **77** (1), 153 (1995).

[212] I. L. Repins, B. J. Stanbery, D. L. Young, S. S. Li, W. K. Metzger, C. L. Perkins, W. N. Shafarman, M. E. Beck, L. Chen, V. K. Kapur, D. Tarrant, M. D. Gonzalez, D. G. Jensen, T. J. Anderson, X. Wang, L. L. Kerr, B. Keyes, S. Asher, A. Delahoy and B. Von Roedern, Prog. Photovolt: Res. Appl. **14**, 4 (2006).

[213] B. A. Schubert, B. Marsen, S. Cinque, T. Unold, *et al.* Prog. Photovoltaics **19** (1), 93 (2011).

[214] T. Tanaka, A. Yoshida, D. Saiki, K. Saito, Q. Guo, M. Nishio, T. Yamaguchi Thin Solid Films **518**, S29 (2010).

[215] C. Lei, C. M. Li, A. Rockett, and I. M. Robertson, J. Appl. Phys. **101**, 024909 (2007).

[216] M. J. Hetzer, Y. M. Strzhemechny, M. Gao, M. A. Contreras, A. Zunger, and L. J. Brillson, Appl. Phys. Lett. **86**,162105 (2005)

[217] J. Li, D. B. Mitzi, and V. B. Shhhenoy, American Chemical Society **5**, 8613 (2011).

[218] Y. Yan, C. -S. Jiang, R. Noufi, Su-Huai Wei, H. R. Moutinho, and M. M. Al-Jassim, Phys. Rev. Lett. **99**, 235504 (2007).

[219] S. Chen, A. Walsh, J-.H. Yang, X. G. Gong, L. Sun, P-.X Yang, J-.H Chu and S-.H Wei Phys. Rev. B **83**, 135201 (2011).

[220] S. Chan, X. G. Gong, A. Walsh and S. H. Wei Appl. Phys. Lett. **96**, 021902 (2010)

Acknowledgement

I would like to express my gratitude and acknowledgement to all the people that made this postgraduate period of my life smooth and enjoyable, and supported me by their scientific knowledge or through their friendship and company so I could prevail and complete this thesis.

- First I would like to thank Prof. **Werner Hofer** for giving me the opportunity to do this PhD. I thank him for his supervision over the years and a lots of freedom and control that he gave me over my research project. It taught me a lot on how to manage myself and my scientific objectives in order to become an independent researcher.

- Special acknowledgements to my group members **Chiara Panosetti**, **Alejandro Sanchez Ronco**, Dr. **Haiping Lin** as well as to Dr. **Adolfo Fuentes**, who offered me their help and support and with whom I had many fruitful discussions.

- I would also like to thank Dr. **Felix Hanke**, Dr. **Matthew Dyer**, **Liz Cocklin**, **Joshua Elliott**, **John Sharp**, **Scott Devoy**, **Emiliano Poli**, Dr. **Ivan Scivetti**, Dr. **Jonas Bjork**, Dr **Geoffrey Thomas** and **Christoper Collins** for their kind advices or proof–reading some of my work.

- I gratefully acknowledge my collaborators for the discussions and very valuable insights to experimental side of my project. Thanks to the Prof. **John Polanyi** and Dr. **Ian McNab** from Toronto, Dr. **Amir Zabet** from Columbia University, Prof. **Ken Durose** from University of Liverpool and Dr. **Budhika Mendis** from Durham University.

- I also acknowledge Dr. **Andris Gulans** from Berlin and well as Dr. **Daniel Belcher** from University of Newcastle, Australia for their advice on the theoretical side.

- I give my special thanks to Dr. **Olalla Nam Lorenzo–Carballa** for her time and support in difficult moments and her precious words of encouragement.

- Many thanks to the efforts of **Cliff Addison** and **Dave Love** for their work in taking care of the computer cluster in Liverpool and for their helpful assistance.

- I would also like to thank my parents for their constant and unconditional love which keeps me strong in all circumstances and to my uncle Roman and my aunt Alinka for their support and belief in me.
- Finally, I would like to thank all my friends who are always with me no matter how far they are.

Publications and contributions at conferences

Published

- *Directed long-range molecular migration energized by surface reaction.*
  K. R. Harikumar, J. C. Polanyi, A. Zabet-Khosousi, P. Czekala*, H. Lin* and W. A. Hofer*
  Nature Chemistry **3**, 400–408 (2011).

- *Acetylene adsorption on silicon (100)–(4 x 2) revisited.*
  P. T. Czekala, H. Lin, W. A. Hofer and A. Gulans*,
  Surface Science **605** (15–16) , pp. 1341–1346 (2011).

- *Van der Waals corrected DFT study of high coverage benzene adsorptions on Si(100)–(4 x 2) surface and STM simulations.*
  P. T. Czekala, C. Panosetti, H. Lin and W. A. Hofer,
  Surface Science **621**, 15 (2013).

To be published

- *Structural and electronic characterization of (112) twin boundary in chalcopyrite, kesterite and stannite materials.*
  P. T Czekala, W. A Hofer and K. Durose

- *Wet oxidation and molecule mediated Si(100) – c(4x2) surface pinning*
  P. T. Czekala and W. A. Hofer

- *Dipolar group functionization for self–assembled molecular line switch on H–Si(100).*
  P. T. Czekala and W. A. Hofer

Conferences, Workshops and Meetings

- *High coverage adsorption of benzene on Si(100) – van der Waals extended studies.*
  Postgraduate talks 2012, University of Liverpool, (oral presentation)

- *Acetylene adsorption on silicon (100)-(4 x 2) revisited*
  Postgraduate online poster presentation, 2012 (poster presentation)

- *Acetylene adsorption on silicon (100)-(4 x 2) revisited*
  CIFAR Nanoelectronics Meeting, Banff, Canada
  November 16, 2010 – November 18, 2010, (poster presentation)

- *DFT study of acetylene adsorption on Si(100) surface with consideration of van der Waals interactions.*
  ECOSS27, (European Conference of Surface Science), Groningen, Netherlands, August 29 – September 3 2010 (oral presentation)

- Ab Initio Electrochemistry Workshop, CECAM-HQ-EPFL, Lausanne, Switzerland
  July 12, 2010 – July 14, 2010

- Materials Studio Workshop,
  University of Liverpool, UK
  12th May 2010,

- ECOSS26 (European Conference of Surface Science) Parma (2009)